Integrating Rupture and Tsunami Modeling to Study Large Subduction Zone Earthquakes

by

David Theodore Small

A dissertation accepted and approved in partial fulfillment of the
requirements for the degree of
Doctor of Philosophy
in Earth Sciences

Dissertation Committee:
Diego Melgar, Advisor and Chairperson
Emilie Hooft Toomey, Core Member
Valerie Sahakian, Core Member
Johnny Ryan, Institutional Representative

University of Oregon

Spring 2024

DISSERTATION ABSTRACT

David Theodore Small
Doctor of Philosophy in Earth Sciences
Title: Integrating Rupture and Tsunami Modeling to Study Large Subduction Zone Earthquakes

This dissertation focuses on studying past and future large subduction zone earthquakes through creating and utilizing a stochastic slip rupture modeling technique in combination with deformation and tsunami modeling. Here, I created a method for incorporating fault zone specific characteristics, like interseismic coupling, into the stochastic slip rupture modeling approach. With this method, output rupture models are informed as to where slip may be more likely to occur based on the specific pattern of coupling. I use the Cascadia subduction zone as a case study to then show how including coupling for rupture generation can impact the resultant tsunami hazards for an area when compared to the traditional approach for stochastic modeling. I find that imposing coupling into the workflow creates noticeable effects on the coastal tsunami hazards.

Next, I validate this approach for earthquake modeling in its ability to model **M**9+ earthquakes. Prior to this, stochastic slip rupture modeling had not been validated in its ability to create "realistic" slip distributions for such large magnitude events. Here, I compare the dissimilarity of a suite of slip distributions created to previously published finite fault models for 4 recent and historic **M**9+ earthquakes. These stochastic models are completely blind to the events we compare them to, however, the stochastic slip modeling approach is able to produce ruptures that have similar slip distributions, and therefore "realistic", to all 4 earthquakes. Additionally, when coupling models are available, the amount and similarity of "realistic" slip distributions can increase. However, the converse could also be true depending on the a priori assumption of coupling included, so a warning should be heeded.

Then, with the validated method for producing coupling informed stochastic slip models, I constrain potential slip distributions for the last great Cascadia earthquake. Unlike any previous attempt, here I incorporate 3 different paleoseismic proxies associated with the event and compare them to results from tsunami and coastal deformation modeling. I specifically compare previously estimated tsunami arrival heights in Japan, subsidence estimates across the coastal

Pacific Northwest, and locations of onshore tsunami sand deposits at 7 coastal marsh and lacustrine environments to those produced by the synthetic rupture models. By utilizing all 3 constraints, I find 7 unique but similar, wall-to-wall heterogeneous slip distributions. I also find that sequences of 3 or 4 closely time (years to a few decades) events can satisfy all 3 constraints equally well. While both modes of failure fit the constraints, I favor the full margin events because adequate sequences require specific extreme tidal conditions to inundate many coastal sites and their fits to the geologic observations are weaker.

This dissertation includes previously published and unpublished co- authored material.

ACKNOWLEDGMENTS

I would like to express my appreciation and gratitude for my advisor, Dr. Diego Melgar, in helping me achieve a graduate experience far greater than I could have imagined. I also would like to give special thanks to rest of my dissertation committee for their help and guidance along the way. Lastly, I would like to express my gratitude for the financial support provided by the National Science Foundation Graduate Research Fellowship Program.

DEDICATION

I dedicate this dissertation firstly to my mom, Sherry Lynn Small. I love you forever and always. Thank you for everything. Secondly, I dedicate this to my dad, Mark Small, who taught me the beauty of science, one Fig Newton at a time.

TABLE OF CONTENTS

LIST OF FIGURES

CHAPTER 1

Introduction

To adequately prepare for the seismic and tsunami hazards associated with large subduction zone earthquakes, we depend on both an understanding of how a fault has failed in the past as well as how it might fail in the future. Luckily, these two conditions are often linked to one another, as it is commonly considered that a fault fails in an earthquake cycle, with repeating characteristics of earthquakes that are controlled by properties specific to the fault zone. Simple enough in theory, however, global seismic instrumentation has only been available since the mid 20th century, limiting our full understanding of the earthquake cycle at any fault zone.

A clear remedy for such shortcomings and uncertainty is found by utilizing synthetic hypothetical earthquakes to supplement the lack of available data. Contained within this dissertation is a means for producing hypothetical earthquakes that are pre-conditioned based on a fault's specific pattern of coupling. Additionally, this dissertation attempts to validate this method and apply it for studying past earthquakes and future tsunami hazards. Chapters 2 and 3 have been previously published, and Chapter 4 is soon to be published. All chapters of this dissertation have been co-authored with my advisor, Diego Melgar, and Chapter 4 is additionally co-authored with SeanPaul La Selle and Andrew Meigs. Chapter 2 focuses on the methodological creation of a branch of stochastic slip rupture modeling that allows for fault zone specific characteristics – in this case, interseismic coupling – to inform output slip models of where slip is more likely to be experienced. To visualize the impact this method has on the output rupture models, I perform a probabilistic tsunami hazard assessment (PTHA) at the Cascadia subduction zone. Then, in Chapter 3, I validate this method's ability to produce realistic great earthquakes (**M**9+) by directly comparing synthetic slip patterns created by this method with previously published finite fault models for 4 **M**9+ earthquakes since 1960. In Chapter 4, I then attempt to constrain the likely slip distribution for the last great Cascadia earthquake that occurred on 26 January 1700 by comparing a catalog of synthetic slip distributions created in this aforementioned rupture modeling technique to known paleoseismic proxies associated to the event. Lastly, in Chapter 5 I provide a recap conclusion of this dissertation and mention some future work.

1.1 Subduction Zone Earthquakes

Subduction zone megathrusts host some of the largest earthquakes, with recent notable events like the 2004 **M**9.1 Sumatra-Andaman and the 2011 **M**9.1 Tohoku-Oki earthquakes. The vast energy and shaking from such events can produce widespread damage across several hundreds of kilometers away from the source (Wirth et al., 2022). To make matters worse, the offshore nature of the seismogenic zone of subduction zones creates the potential for such large earthquakes to produce tsunamis adding to the overall devastation. The combined damage of the Sumatra and Tohoku earthquakes and tsunamis resulted in over US$220 billion in economic damages and more than 250,000 fatalities (Telford and Cosgrave, 2006; Kajitana et al., 2013). Although **M**9+ ruptures have only occurred 4 times since 1960, their impacts are felt for a lifetime.

Not all subduction zones behave the same, with some like the Honshu subduction zone hosting 3 great (**M**8+) earthquakes since 1900, and others experiencing them far more sparingly, like the Cascadia subduction zone who has not experienced a great earthquake since 1700. With a steady rate of plate convergence, it is often considered that large earthquakes at subduction zones will fail in somewhat regular intervals, creating a seismic cycle. Here, a fault is initially loaded during the interseismic period, where plate convergence in some portions goes unaccommodated, and stress builds up. Once the frictional stability is overcome, an earthquake is produced, relieving some amount of the overburdened stress. Following the earthquake, there is a period of post-seismic adjustment of the fault as a response to the sudden change. This post-seismic adjustment results in additional slip, that through time decays back to the steady state interseismic period, returning the cycle to the start once more. While complex in nature, recognized patterns of failure, or overall earthquake recurrence, has been observed from historic data at subduction zones globally (Philibosian and Meltzner, 2020). Modern theories that consider recent and paleoseismic observations often can be fit by a recurrence model dominated by quasi-periodic and similar large magnitude ruptures (Zielke, 2018).

1.1.1 Interseismic to Coseismic

As one plate converges with another in a subduction zone, the overall plate convergence rate is accommodated through a combination of earthquake failure, episodic tremor and slow slip,

and aseismic stable sliding. Cumulative seismic slip, however, appears to account for less than half of the overall convergence rate experienced at plate boundaries (Bilek and Lay, 2018). With the increase in geophysical methods and global instrumentation for measuring earthquakes, our ability to model the heterogeneity in coseismic slip has dramatically improved. This property of earthquake slip is clearly seen in any finite fault model of recent earthquakes (Mai & Thingbaijam, 2014). Many factors contribute to this heterogeneity and slip variability of earthquakes, including the presence of fluids, sediment, and variable plate topography (Bilek and Lay, 2018). All these factors, however, generally influence the heterogeneity of earthquakes through their impact on the overall frictional strength of the fault zone.

The degree of frictional locking of a fault controls how the plate convergence is being accommodated, where frictionally locked segments will experience low or no interseismic creep and thus produce a slip deficit that may be alleviated by future earthquakes (Lindsey et al., 2021). Because frictional locking is not a geodetically measurable feature, I instead focus on geodetic coupling, which is influenced by frictional locking but can be measured directly from GNSS. For many recent great earthquakes, good correlation between regions of high coupling and coseismic slip has been observed. For example, these correlations were seen from the 2007 **M**8.0 Pisco, Peru (Perfettini et al., 2010), 2010 **M**8.8 Maule, Chile (Moreno et al., 2010), and the 2011 **M**9.1 Tohoku earthquake (Loveless and Meade, 2011). Throughout all chapters of this dissertation, I utilize this correlation between large slip patches and high coupling to help inform synthetic rupture models of where slip may be more likely. The work detailed in this dissertation relies on the correlation of fault slip and coupling as a way to inform hypothetical ruptures. More information on this is found in Chapter 2.

1.1.2 Coseismic to Tsunami

As previously mentioned, large subduction zone earthquakes produce hazards for coastal communities from both seismic shaking as well as tsunami generation. Of the biggest concern for tsunami hazards is the shallow offshore slip and potential activation of shallow splay faults that can further enhance tsunami amplitudes. Because megathrust rupture slip is often concentrated offshore in the seismogenic zone, surface uplift is predominantly experienced offshore and subsidence at the coast, intensifying the impact of the tsunami propagation onshore. While most tsunami generation signal comes from vertical advection of the seafloor, steeply

sloping seafloor topography can produce "pseudo-vertical" deformation, aiding in the size of the tsunami (Tanioka and Sataka, 1996). As a tsunami wave approaches the coast, the decrease in water depths shortens the wave packet and increases its amplitude. A catastrophic tsunami has the potential to reach several tens of meters in run-up height and can inundate several kilometers inland from the coast. This is clearly seen by the tsunami resulting from the 2011 Tohoku earthquake. This catastrophic tsunami reached almost 40 m in amplitude off the Sanriku Coast and in the Sendai Plain had a run-up distance of over 5 km inland (Mori et al., 2011).

Throughout this dissertation, I incorporate tsunami modeling as a tool for studying large subduction zone ruptures. In Chapter 2, I use tsunami modeling to produce a probabilistic hazard assessment along the Pacific Northwest (more information on this in section 1.3.1). This assessment implements tsunami arrival height as the intensity metric for understanding the tsunami hazards associated with a subduction zone earthquake. In Chapter 3, I use tsunami inundation modeling along the western coast of Japan to supplement the ability to validate synthetic ruptures against historic **M**9+ earthquakes. Finally, in Chapter 4, I incorporate tsunami inundation modeling as a tool to constrain possible slip distributions for the 1700 Cascadia event. Not only are tsunamis and their associated hazards important phenomena to study, but they can also be valuable tools to study other Earth processes.

1.1.3 Synthetic Rupture Modeling

Synthetic rupture modeling has become an increasingly popular tool for modeling future potential earthquakes. Due to the incompleteness of global earthquake catalogs and the long recurrence interval for large earthquakes, we can alleviate the lack of data by supplementing it with hypothetical ruptures that follow known characteristics of past earthquakes. Once such method for producing synthetic ruptures is with stochastic slip modeling. In the last two decades, the application this approach has grown into many fields as it is a computationally inexpensive and simple approach for calculating heterogeneous slip models. This method for rupture generation has been applied to test earthquake and tsunami early warning systems (Ruhl et al., 2017), train machine learning algorithms (Lin et al., 2021), produce seismic and tsunami hazards assessments (Graves et al., 2011; LeVeque et al., 2017), and constrain historic earthquake slip distributions (Melgar, 2021). While there are several approaches to stochastic modeling (e.g., Herroro and Bernard, 1994; Davies et al., 2015), here I specifically focus on the von Karman

autocorrelation function stochastic slip method (Mai and Beroza, 2002). All chapters of this dissertation incorporate synthetic rupture models and highlight multiple instances where producing hypothetical earthquakes is of great value. In Chapter 2, I lay down a method for including fault zone characteristics as a priori constraints for stochastic slip models. In Chapter 3, I then validate this method in its ability to produce realistic **M**9+ earthquakes. Finally, I use a large suite of stochastic models and compare them to various paleoseismic datasets to determine potential slip distributions for the 1700 Cascadia earthquake in Chapter 4.

1.2 Studying Historic Earthquakes

One of the difficulties adding to our uncertainty in what the next large earthquake may be is the lack of observations and data for the full suite of past earthquakes. Currently, there is an array of continuous GNSS and seismic networks across many major subduction zones, allowing us to observe the current state of the faults. Although clear connections between interseismic displacements and coseismic slip have been recognized, one is not a simple inverse of the other (Govers et al., 2018). Understanding how slip is partitioned throughout multiple iterations of the seismic cycle will lead to a better understanding of how the two connect.

1.2.1 Paleoseismic Proxies

Because geophysical observations of earthquakes are limited to the last century, we can supplement this lack of geophysical observations with paleoseismic records preserved geologically. Large subduction zone earthquakes will often then be recorded and preserved by secondary processes, providing indirect evidence for the occurrence of an event. Some paleoseismic proxies that point to a past earthquake include turbidites deposits from submarine or lacustrine slope failures (e.g., Hill et al., 2022), stratigraphic and micro-fossil assemblages correlating to rapid coseismic subsidence (e.g., Padgett et al., 2021), stratigraphic tsunami sand deposits (e.g., Spruell, 2018), and terrestrial paleo-landslide deposits (e.g., Grant et al., 2022). These proxies can then be associated with one another based on similar dates and their spatial extent can help guide our hypothesis of how large an event likely was. Unfortunately, error uncertainties can exceed decades to even centuries, making it difficult to fully understand if the proxies are connected to a single event or rather a sequence of closely timed events. Nonetheless, each one of these proxies has been fundamental for constraining paleoseismic events.

An example of where paleoseismic proxies has been fundamental to the study of the megathrust is at the Cascadia subduction zone. With no great earthquakes occurring in instrumental time, we rely entirely on the preserved geologic records to study past earthquakes. Luckily, much of the coastal Pacific Northwest is wetland marsh environments and pervasive mass wasting occurs along the Cascadia margin, creating ideal conditions for preservation of geologic seismic records (Hill et al., 2022). The coastal and submarine records of large earthquakes in Cascadia are some of the largest and best preserved in the world, with records of earthquakes occurring over the 10 ka years (Goldfinger et al., 2012, 2017).

In Chapter 4, I use 3 paleoseismic proxies associated with the 1700 Cascadia earthquake to constrain the possible slip distributions that might represent this event. Rupture models used here are created by the method described in Chapter 2. Surface deformation and tsunami inundation modeling are key components of this study as the outputs from these models are analyzed against the known paleoseismic constraints. If we can use the same techniques applied in Chapter 4 to study earthquakes prior to the 1700 event and can constrain slip distributions for those events, we can more confidently say how Cascadia likely ruptures and even what the slip budget might look like for the next earthquake. Unfortunately, incorporating these methods to study older past ruptures becomes increasingly difficult due to the growing uncertainty in past landscapes the further we look. This should not prevent us, however, from attempting to do so.

1.3 Preparing for the Future

Rather than attempting to predict what the next large earthquake will be, it is appealing to instead generate hypothetical future earthquakes and evaluate hazards and risk for community resilience. The most devastating natural hazards associated with coastal communities often comes from tsunamis and earthquakes. While methods for determining probabilistic seismic hazards have been around since the 1960s (e.g., Cornell, 1968), the rare nature of tsunamis has made calculating their hazards far less common. However, the devastation following the 2004 Sumatra and the 2011 Tohoku earthquakes and tsunamis really highlighted the limitations of our understanding of potential hazards and necessity for global hazard assessments.

1.3.1 Probabilistic Hazard Assessments

Both probabilistic seismic and tsunami hazard assessments (PSHA and PTHA) are focused

on assessing the likelihood of exceeding some kind of intensity metric at a specific location over a given period of time. Rather than a deterministic/scenario-based approach (e.g., Priest et al., 2010), these methods assess hazards based on a full suite of potential earthquakes and tsunamis. For PSHA, an example intensity metric used is peak ground acceleration, which can then be related to the expected level of damage to buildings and infrastructure. For PTHA, intensity measures include maximum tsunami arrival height or maximum inland inundation (e.g., Geist and Parson, 2006). In more recent PTHA studies, additional intensity measures of flow depth and speed have been implemented for more adequate analysis for evacuation planning and infrastructure damage estimation (De Risi et al., 2017).

In Chapter 2 of this dissertation, I employ a PTHA study for the CSZ based on a large suite of realistic, hypothetical ruptures and probability of exceeding the tsunami arrival height intensity metric. The application of the PTHA study used here is not intended to be implemented by communities. Still, it provides some insight into coastal regions with greater hazards associated with incoming tsunami arrival heights as well as highlights the impact of applying various assumptions for background models used to inform stochastic slip ruptures.

References Cited

Bilek, S. L., & Lay, T. (2018). Subduction zone megathrust earthquakes. *Geosphere*, *14*(4), 1468-1500.

Cornell, C. A. (1968). Engineering seismic risk analysis. *Bulletin of the seismological society of America*, *58*(5), 1583-1606.

Davies, G., Horspool, N., & Miller, V. (2015). Tsunami inundation from heterogeneous earthquake slip distributions: Evaluation of synthetic source models. *Journal of Geophysical Research: Solid Earth*, *120*(9), 6431-6451.

De Risi, R., Goda, K., Yasuda, T., & Mori, N. (2017). Is flow velocity important in tsunami empirical fragility modeling?. *Earth-science reviews*, *166*, 64-82.

Grant, A. R., Struble, W. T., & LaHusen, S. R. (2022). Limits to coseismic landslides triggered by Cascadia Subduction Zone earthquakes. *Geomorphology*, *418*, 108477.

Geist, E. L., & Parsons, T. (2006). Probabilistic analysis of tsunami hazards. *Natural Hazards*, *37*, 277-314.

Graves, R. W., Aagaard, B. T., & Hudnut, K. W. (2011). The ShakeOut earthquake source and ground motion simulations. *Earthquake Spectra*, *27*(2), 273-291.

Goldfinger, C., Galer, S., Beeson, J., Hamilton, T., Black, B., Romsos, C., ... & Morey, A. (2017). The importance of site selection, sediment supply, and hydrodynamics: A case study of submarine paleoseismology on the northern Cascadia margin, Washington USA. *Marine Geology*, *384*, 4-46.

Goldfinger, C., Nelson, C. H., Morey, A. E., Johnson, J. E., Patton, J. R., Karabanov, EI., ... & Vallier, T. (2012). *Turbidite event history—Methods and implications for Holocene paleoseismicity of the Cascadia subduction zone* (No. 1661-F). US Geological Survey.

Govers, R., Furlong, K. P., Van de Wiel, L., Herman, M. W., & Broerse, T. (2018). The geodetic signature of the earthquake cycle at subduction zones: Model constraints on the deep processes. *Reviews of Geophysics*, *56*(1), 6-49.

Herrero, A., & Bernard, P. (1994). A kinematic self-similar rupture process for earthquakes. *Bulletin of the Seismological Society of America*, *84*(4), 1216-1228.

Hill, J. C., Watt, J. T., & Brothers, D. S. (2022). Mass wasting along the Cascadia subduction zone: implications for abyssal turbidite sources and the earthquake record. *Earth and Planetary*

Science Letters, *597*, 117797.

Kajitani, Y., Chang, S. E., & Tatano, H. (2013). Economic impacts of the 2011 Tohoku-Oki earthquake and tsunami. Earthquake Spectra, 29(1_suppl), 457-478.

Lin, J. T., Melgar, D., Thomas, A. M., & Searcy, J. (2021). Early warning for great earthquakes from characterization of crustal deformation patterns with deep learning. *Journal of Geophysical Research: Solid Earth*, *126*(10), e2021JB022703.

Lindsey, E. O., Mallick, R., Hubbard, J. A., Bradley, K. E., Almeida, R. V., Moore, J. D., ... & Hill, E. M. (2021). Slip rate deficit and earthquake potential on shallow megathrusts. *Nature Geoscience*, *14*(5), 321-326.

Loveless, J. P., & Meade, B. J. (2011). Spatial correlation of interseismic coupling and coseismic rupture extent of the 2011 Mw= 9.0 Tohoku-oki earthquake. *Geophysical Research Letters*, *38*(17).

Mai, P. M., & Beroza, G. C. (2002). A spatial random field model to characterize complexity in earthquake slip. *Journal of Geophysical Research: Solid Earth*, *107*(B11), ESE-10.

Mai, P. M., & Thingbaijam, K. K. S. (2014). SRCMOD: An online database of finite-fault rupture models. *Seismological Research Letters*, *85*(6), 1348-1357.

Melgar, D. (2021). Was the January 26th, 1700 Cascadia earthquake part of a rupture sequence?. *Journal of Geophysical Research: Solid Earth*, *126*(10), e2021JB021822.

Moreno, M., Rosenau, M., & Oncken, O. (2010). 2010 Maule earthquake slip correlates with pre-seismic locking of Andean subduction zone. *Nature*, *467*(7312), 198-202.

Mori, N., Takahashi, T., Yasuda, T., & Yanagisawa, H. (2011). Survey of 2011 Tohoku earthquake tsunami inundation and run-up. *Geophysical research letters*, *38*(7).

Padgett, J. S., Engelhart, S. E., Kelsey, H. M., Witter, R. C., Cahill, N., & Hemphill-Haley, E. (2021). Timing and amount of southern Cascadia earthquake subsidence over the past 1700 years at northern Humboldt Bay, California, USA. *Bulletin*, *133*(9-10), 2137-2156.

Perfettini, H., Avouac, J. P., Tavera, H., Kositsky, A., Nocquet, J. M., Bondoux, F., ... & Soler, P. (2010). Seismic and aseismic slip on the Central Peru megathrust. *Nature*, *465*(7294), 78-81.

Philibosian, B., & Meltzner, A. J. (2020). Segmentation and supercycles: A catalog of earthquake rupture patterns from the Sumatran Sunda Megathrust and other well-studied faults worldwide. Quaternary Science Reviews, 241, 106390.

Priest, G. R., Goldfinger, C., Wang, K., Witter, R. C., Zhang, Y., & Baptista, A. M. (2010).

Confidence levels for tsunami-inundation limits in northern Oregon inferred from a 10,000-year history of great earthquakes at the Cascadia subduction zone. *Natural Hazards*, *54*, 27-73.

Ruhl, C. J., Melgar, D., Grapenthin, R., & Allen, R. M. (2017). The value of real-time GNSS to earthquake early warning. *Geophysical Research Letters*, *44*(16), 8311-8319.

Spruell, J. T. (2018). Up-estuary extent and lithologic characteristics of tsunami deposits attributed to the 1700 Cascadia earthquake within Alsea Bay, OR.

Tanioka, Y., & Sataka, K. (1996). Fault parameters of the 1896 Sanriku tsunami earthquake estimated from tsunami numerical modeling. *Geophysical research letters*, *23*(13), 1549-1552.

Telford, J., Cosgrave, J., & Houghton, R. (2006). Joint evaluation of the international response to the Indian Ocean tsunami. *Synthesis report*, *110*.

Wirth, E. A., Sahakian, V. J., Wallace, L. M., & Melnick, D. (2022). The occurrence and hazards of great subduction zone earthquakes. *Nature Reviews Earth & Environment*, *3*(2), 125-140.

Zielke, O. (2018). Earthquake recurrence and the resolution potential of tectono-geomorphic records. *Bulletin of the Seismological Society of America*, *108*(3A), 1399-1413.

CHAPTER 2

Geodetic Coupling Models as Constraints on Stochastic Earthquake Ruptures: An Example Application to PTHA in Cascadia

From Small, D. T., & Melgar, D. (2021). Geodetic coupling models as constraints on stochastic earthquake ruptures: An example application to PTHA in Cascadia. *Journal of Geophysical Research: Solid Earth*, *126*(7), e2020JB021149.

2.1 Introduction

Using stochastic slip ruptures has become an increasingly popular tool for modeling potential future large earthquakes. Fundamentally, stochastic modeling revolves around the assumption that the distribution of coseismic slip on a fault can be considered a spatially random field (Mai & Beroza, 2002). In particular, for regions where large earthquakes are likely and where observations are limited, a substantial number of source models can be formulated if one can reasonably assume the statistical parameters (the correlation function) of the random field. Then, for a given magnitude of interest, one can generate any number of slip distributions by making random draws from the appropriate distribution. This approach has been found quite useful in a number of hazards-related applications. For instance, the stochastic ruptures can be used to generate strong motion seismograms to study the potential ground motions in a specific region of interest (e.g., Frankel, Wirth, et al., 2018; Graves et al., 2011; Wirth et al., 2018). The time-histories from these stochastic sources can even be used for analyzing the response of structures2 and critical infrastructure to potential future earthquakes (Bijelić et al., 2018). Likewise, stochastic sources and their resulting seismic and geodetic waveforms can be used to test the response of earthquake early warning systems (Goldberg & Melgar, 2020; McGuire et al., 2021; Ruhl et al., 2017) and tsunami early warning systems that rely on onshore data (Williamson, Melgar, Crowell, et al., 2020). This same approach is now becoming common practice in probabilistic tsunami hazard analysis (PTHA) where stochastic source modeling, when

connected with advanced numerical models that simulate tsunami propagation, are also rapidly becoming a mainstay of that field (Grezio, Babeyko, et al., 2017).

Like the advances in stochastic source modeling, tectonic geodesy has progressed substantially in the last 30 years, spurred from the expansion of Global Navigation Satellite System (GNSS) capabilities. For example, it has become commonplace to use measurements of the long-term inter-seismic velocity field to identify which portions of faults are more or less coupled. A review of this can be found in Bock and Melgar (2016). Although our ability to predict future earthquakes is limited, we are able to relate these coupling models to long-term future earthquake potentials. Notably, in the California earthquake hazard model UCERF3 (Field et al., 2017) the inter-seismic surface velocity field is used to constrain long term "slip rates" of faults which are a primary constraint to determine the moment budget over broad areas along a fault zone. Overall, it is generally agreed that where coupling is higher and faults are accumulating a slip deficit at a faster rate, earthquakes are more likely to occur. Similarly, the areas with the greatest amount of slip during large ruptures often correlate with highly coupled patches of the fault zone. This relationship between coupling and slip is seen in previous large ruptures across a range of fault zones (e.g., Barnhart et al., 2016; Konca et al., 2008; S. Li & Freymueller, 2018; Moreno, Rosenau, & Oncken, 2010; Ozawa et al., 2011).

This correlation is not perfect, however, and the present-day pattern of heterogeneous coupling on a fault does not equate to the pattern of slip during the next earthquake. There is a myriad of other controlling variables which can be unique to each fault zone, such as the complex fault geometries, past and present stress regimes, and rupture dynamics to name a few. This creates large uncertainty in how a future earthquake will rupture. In spite of these, it remains true that highly coupled fault patches are accumulating a slip deficit at a faster rate and thus have a larger budget of available slip to use during the next event. Here we will show how to use that fault coupling to condition the likelihood of where slip should be expected in future earthquakes. Our proposed approach does not require, in a deterministic sense, that high slip occur in highly coupled patches, rather it increases the probability that it does. As a result, over many stochastic rupture simulations, on average, more slip will occur where inter-seismic coupling is higher and less where coupling is lower. However, for any one particular realization, slip can still be high in a low coupling region, and low in a highly coupled region.

To illustrate the impact of this we will show how assuming different coupling models impacts PTHA in the Cascadia subduction zone (CSZ) in particular. After the 2004 M9.2 Sumatra earthquake and tsunami which led to 240,000 casualties, probabilistic tsunami hazard assessment (PTHA, Geist & Parsons, 2006; Grezio, Babeyko, et al., 2017) has become a rapidly expanding methodology used for assessing the hazard potential of future earthquakes and tsunamis. Unlike site-specific tsunami studies, PTHA is rooted in determination of the probability of exceeding some threshold of tsunami intensity measure (e.g., tsunami arrival height) for one or many target sites for a given return period (e.g., 100 years). A fundamental difficulty addressed by application of PTHA is that awareness of previous historical tsunamis past hundreds to thousands of years is limited and sometimes based on historical recounts rather than surficial expressions or direct measurements of their impacts. In recent advances to PTHA, it has become more prevalent to rely on modeling complex earthquake source rupture processes, such as the heterogeneous slip distributions, and use the resulting deformation as the initial condition for propagation modeling. This is then combined with some probabilistic scaling relations as well as earthquake recurrence rates for quantification of likely exceedance of tsunami hazard intensities (e.g., De Risis & Goda, 2017; Grezio, Cinti, et al., 2020; L. Li et al., 2016).

In this approach to PTHA, arguably, the largest source of uncertainty is the earthquake or rather the tsunami source, since propagation modeling is already highly advanced and bathymetry, both in the deep ocean and in the nearshore, is relatively well-known. Earlier tsunami forecasting methods assumed a uniform slip on a geometrically simple fault buried in a homogeneous elastic half-space. It is now broadly recognized that assuming homogeneous slip drastically underrepresents the tsunamigenic potentials when compared to heterogeneous slip models for the same magnitude (Melgar, Williamson, & Salazar-Monroy, 2019; Ruiz et al., 2016). The situation is different, however, for inundation modeling of overland flow. Many advances in modeling the fluid dynamics of propagation over an erodible substrate and through the built environment are still necessary and introduce equally, if not larger, sources of uncertainty than knowledge of the earthquake source. However, for the simpler problem of quantifying the expected tsunami at the shoreline, without considering inundation, better constraints on what sources can realistically be expected to occur is one of the improvements that can most significantly reduce uncertainties in the hazard estimate. Lastly, presence and

contribution of splay faulting on tsunami hazards can also produce reasonable further uncertainties for PTHA studies (e.g., Gao et al., 2018). For the purpose of the paper, however, we do not focus on this aspect.

In this work we focus on the CSZ as it is extensively studied, has a suite of previously constrained coupling models, is well instrumented onshore, and is perceived as having high associated hazards. First, we present the mathematical formalism for introducing a geodetic coupling model as a prior constraint on the resulting stochastic rupture. We then model a total of 11,200 stochastic slip rupture scenarios for a magnitude range of M7.8–M9.1 on the CSZ in order sample a large enough range of tsunamigenic ruptures. We make four different assumptions on prior coupling which leads to for four distinct classes of ruptures. Two classes include different end member coupling models from Schmalzle et al. (2014) that vary in terms of their near-trench coupling estimates (noted as the "Gamma" and "Gaussian" coupling models). For the other two classes of ruptures, we produce stochastic slip in the traditional way, where, beyond assuming a down-dip limit of slip, there are no assumptions on where slip can occur, that is, with no coupling model. Following Frankel, Chen, et al. (2015), these last two classes have a deep ~30 km depth limit associated with the top of the tremor zone, and a ~15–25 km depth limit associated with the average 1 cm/yr slip deficit rate (25%) contour. For convenience, the class with a downdip limit associated with the top of the tremor zone will hereafter be called the "30 km depth" class. This last class follows what was proposed by Wirth and Frankel (2019) and although it is defined from regional coupling, no knowledge of the pattern of coupling is associated with the calculation of these ruptures.

For each of the rupture simulations we model tsunami propagation to the coast and analyze the resulting coastal tsunami amplitudes using hazard curves and hazard maps. Tsunami intensities vary considerably between classes, where these differences are best expressed off the coast of the Olympic Peninsula. Hazard curves for coastal points and hazard maps detail that with increasing distance north, the variations in hazards become much more distinct, where the coastal points experience greatest tsunami arrivals for the Gamma class. We stress that in this work we are not making an authoritative hazard assessment for the CSZ. Rather, we simply aim to demonstrate the impacts of conditioning the ruptures with a coupling model. Whether or not ruptures constrained by coupling are similar to past and future ruptures is a key question moving forward. It is our hope, however, that future authoritative hazards assessments more formally

consider geodetic coupling and that our work be used as motivation to better constrain offshore coupling in particular through expanded seafloor measurements. The variability between models that we will show highlights the need for these improvements.

2.2 Methods

2.2.1 Geodetic Coupling Models

Fault coupling models (e.g., Bürgmann et al., 2005; Konca et al., 2008; Loveless & Meade, 2010; Moreno, Melnick, et al., 2011) are obtained from inversion of surface velocities measured by geodetic techniques such as global navigation satellite systems (GNSS) and tide gauges. Accurately constraining coupling models can be done through integrating paleoseismic data (e.g., McCaffrey et al., 2007), however, good paleoseismic records are typically sparse for a given region. In theory, coupling models provide an estimate of a fault's present-day ability to move. Coupling is typically quantified by the ratio of the on-fault slip rate versus the long term far-field plate rate (e.g., the convergence rate at a subduction zone). A ratio of 1 is fully coupled and represents no current motion along the plate interface during the inter-seismic period, whereas a ratio of 0 indicates aseismic stable sliding (creep). Conversely, coupling models also include by definition an estimate of the "slip deficit rate." The coupling fraction is therefore the ratio between the slip deficit rate and the local plate convergence rate. Areas that are fully coupled, are accumulating a slip deficit fastest, specifically at the plate convergence rate.

The reliability of the calculated coupling models is dependent on the abundance, distribution, and timescale of geodetic stations (primarily GNSS). The resolving power of a specific GNSS site falls rapidly with distance. Currently, GNSS coverage of subduction zones worldwide is quite good for the on-shore portion (e.g., Barrientos & Pérez-Campos, 2018) but is very limited offshore. Seafloor geodetic instrumentation, which was pioneered at the CSZ (Spiess et al., 1998) is currently only widely implemented in Japan (Yokota et al., 2016), however its use is slowly expanding. This lapse in GNSS coverage means that the uncertainty in the recovered interseismic coupling, which is largely in the offshore shallow portion of the subduction zone, can be quite high (e.g., Loveless & Meade, 2010; Schmalzle et al., 2014). Due to the sparsity of station coverage, a multitude of non-unique estimations of plate coupling can be determined for a region. As a result of this uncertainty, different modeling assumptions will lead to different results for the near-trench coupling. Although coupling models are non-unique, they currently

provide one of the best approaches for understanding the influence of regional slip deficits on rupture heterogeneities in a given area.

In this paper, we consider two different coupling models (Figure 1) for the CSZ from Schmalzle et al. (2014). Both represent the “decade scale” distribution of coupling where the effect of transient slip such as slow slip events is accounted for. The first model uses an a priori assumption that complete coupling occurs from the trench to some distance down dip and that at all points along strike coupling fraction decreases to free slip by a shape factor, gamma (K. Wang et al., 2003; further referred to as the “Gamma” coupling model). In contrast, the second approach uses a Gaussian distribution of coupling with depth, dependent on a model parameter, mean depth, and spread, or standard deviation, of the coupling (further referred to as the “Gaussian” coupling model). Due to the Gaussian nature of the coupling pattern, at shallow depths near the trench, the plate has low coupling and is mostly stably sliding. In this model coupling is centralized down dip (Figure 1). These models were computed on an older megathrust geometry from McCrory et al. (2012). However, we translated these models to the updated slab geometry from Hayes et al. (2018) through nearest neighbor interpolation. It is important to note that both of these approaches fit the known on-shore GNSS velocities, tide gauge records, and geologically derived uplift rates with near identical confidence.

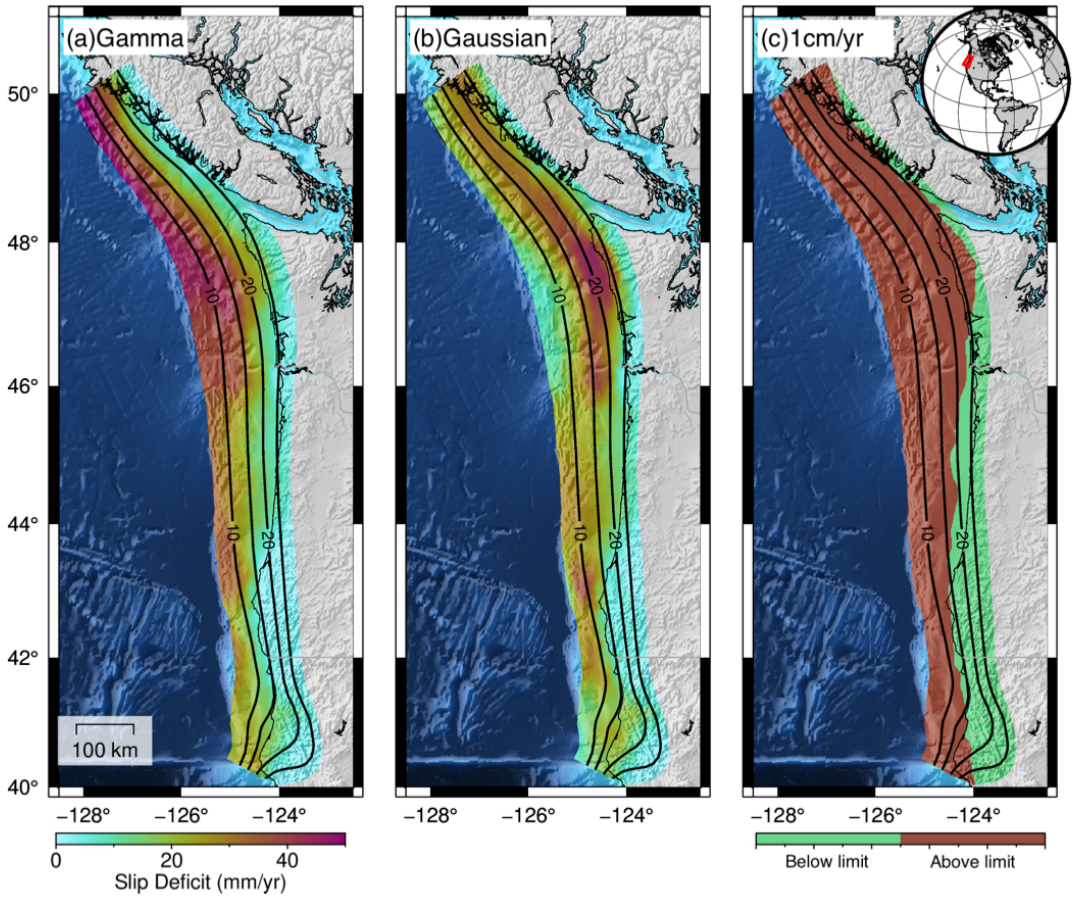

Figure 1. *Fault coupling models from Schmalzle et al. (2014) for the Cascadia subduction zone (CSZ). Color scale details slip deficits where a higher value of slip deficit corresponds to areas with the highest coupling ratio and a slip rate deficit of 0 mm/yr is freely sliding. (a) The Gamma decade-scale coupling model which assumes the slab is fully coupled with large slip rate deficits at the trench and monotonically decays downdip by the shape factor gamma. (b) The Gaussian decade-scale coupling model which imposes a Gaussian distribution of coupling with depth as well as penalties to constrain mean coupling above 30 km in depth. (c) Downdip limit of slip model defined by the Frankel, Chen, et al. (2015) 1 cm/yr coupling contour (25% coupling) limit of slip. Color defines either active regions that may participate in slip (above limit) or regions of the fault that will not (below limit). Contours are the slab depths from Hayes et al. (2018) at 5 km intervals. Inset at top right shows the location of the CSZ.*

2.2.2 Stochastic Ruptures with a Geodetic Coupling Model Constraint

The first step in obtaining a rupture model is to determine which portions of the larger megathrust will contribute to a given earthquake. Since our target magnitudes span a range of M7.8 to M9.1 not all portions of the megathrust will participate in any given rupture. To select a subset of the megathrust we follow the approach detailed in Melgar, LeVeque, et al. (2016). Given a target magnitude, we determine the length, L, and width, W, of the rupture. We make a random draw from probabilistic scaling laws (Blaser et al., 2010) which state that length and width follow the magnitude dependent log-normal distribution with mean and standard deviation given by

$$\log_{10} L \sim N(-2.37 + 0.57M, \sigma_L),$$
$$\log_{10} W \sim N(-1.86 + 0.46M, \alpha_w),$$

with standard deviations defined in the original work. By making these random draws, the objective is to obtain a length and width that is consistent with the behavior seen in earthquakes worldwide while retaining the observed variability as well. The probabilistic scaling law thus ensures that for a given magnitude we do not always employ the same fault dimensions. Once these dimensions are known we randomly select a portion of the larger megathrust models that is within these bounds. An example of this can be seen in Figures 2 and 3 where the fault dimensions for a potential M8.7 event have been obtained from the probabilistic scaling laws and used to define a subset of the megathrust to use for the stochastic rupture.

Next, we define the rupture model itself. Slip can be conceptualized as a spatially random field whose heterogeneity can be described by statistical parameters. A number of unique slip realizations can then be determined as long as they are constrained by an underlying probability distribution. Mai and Beroza (2002) found that to best model the spatially random slip field the most suitable autocorrelation function (ACF) is the von Karman ACF. In their proposed approach, the von Karman ACF is enforced using a spectral representation, P(k), of slip in the Fourier domain defined as the ratio of the correlation lengths for along-strike (a_x) and downdip (a_z) directions,

$$P(k) = \frac{a_x a_z}{(1+k^2)^{H+1}},$$

where H is the hurst exponent describing the spectral decay at higher wavenumbers. The radial wavenumber, k, is then defined as

$$k = \sqrt{a_x^2 k_x^2 + a_z^2 k_z^2}\ .$$

The correlation lengths described in the von Karman ACF determine the dominant asperity sizes for the model. Here, it is determined that as magnitudes increase, the correlation lengths increase as well following a log-linear scaling (e.g., Melgar & Hayes, 2019). The Hurst exponent in Equation 3 on the other hand, seems to be magnitude independent and typically is assumed to be between 0.4 and 0.7 (Mai & Beroza, 2002; Melgar & Hayes, 2019).

The approach from Mai and Beroza (2002) is well suited for an approximation of a rectangular fault geometry, however, some complexities such as a multi fault or 3D fault geometry (e.g., the large bend in northern CSZ) can be difficult to account for. Similarly, enforcing prior constraints on the rupture model, such as the geodetic coupling model, is not inherently straightforward. An alternate approach is to work directly in the spatial domain. LeVeque, Waagan, et al. (2016) use the Karhunen-Loeve (K-L) expansion with the von Karman ACF to the same effect as the spectral approach. The spatial representation of the VK-ACF is used,

$$C_{ij}(r_{ij}) = \frac{G_H(r_{ij})}{G_0(r_{ij})}\,,$$

$$G_H(r_{ij}) = r_{ij}^H K_H(r_{ij})\ ,$$

where C_{ij} is the correlation between the i-th and j-th subfaults, KH is the modified Bessel function of the second kind and H is the Hurst exponent. r_{ij} is the inter-subfault distance given by

$$r_{ij} = \sqrt{\left(\frac{r_s}{a_s}\right)^2 + \left(\frac{r_d}{a_d}\right)^2}\ ,$$

where r_s is the along-strike distance and r_d the along-dip distance. These are obtained using a spline interpolation of the 3D fault geometry as detailed by Melgar, LeVeque, et al. (2016). Once all the parameters of the correlation matrix are defined, the covariance matrix is obtained by

$$\widehat{C_{ij}} = \sigma_i C_{ij} \sigma_j\ ,$$

where σ is the standard deviation of slip, which we set here to 0.45, irrespective of magnitude, following Melgar and Hayes (2019). The K-L expansion then states that to obtain a random realization the slip vector, s, that contains each subfault's slip will be

$$s = \mu + \sum_{k=1}^{N} z_k \sqrt{\lambda_k \nu_k} \, .$$

Here, μ, is the mean of s and the statistics of the VK-ACF are enforced by the eigenvalues, λ_k, and eigenvectors,ν_k, of C_{ij} (Equation 8). z_k are normally distributed random numbers with a mean of 0 and a standard deviation of 1 which introduce the desired stochastic variability. N is the number of eigenmodes which corresponds to the number of subfaults or elements of s. If all the eigenmodes are used, then the stochastic realization produces the same results as if the analysis was carried out in the wavenumber domain. For certain applications, such as PTHA, where long period features dominate the resulting tsunami signals, after the first few tens of modes the contributions to tsunamigenesis from the short length-scale modes becomes negligible (LeVeque, Waagan, et al., 2016). In these cases, the summation can be truncated. Here, however, we use all eigenmodes. In the absence of any external knowledge it is commonplace to assume a homogeneous mean slip model, μ. In this case, given the assumed fault dimension and rigidities from the reference Earth model, enough slip is distributed over all subfaults to match the desired target magnitude. In other words, slip is equally likely at all subfaults irrespective of location both along strike and down dip of the fault. Once more, if this is done then the results will be the same as if carrying out the stochastic slip realization in the wavenumber domain. However, here lies the critical advantage afforded by the K-L expansion, we can assume that the mean slip model, μ, is related to, or rather defined by, the geodetic coupling.

The process for defining the mean model, μ, based on the geodetic coupling is as follows and is shown in Figure 2. Once a megathrust segment is selected following the probabilistic scaling laws for the desired magnitude (M8.7 in the example in Figures 2 and 3) the geodetic coupling (Figures 2a and 3a) is re-scaled to slip (Figures 2b and 3b) to match the target moment. This mean slip model now has the same features as the coupling, with higher slip in high coupling areas and lower slip where coupling is low, and even 0 slip where coupling is 0. Figures 2c and 3c then show 8 realizations of stochastic rupture using the K-L expansion with the non-homogeneous mean model. Note that each realization does not look exactly like the coupling model, but on average slip is more likely where coupling is high, as desired.

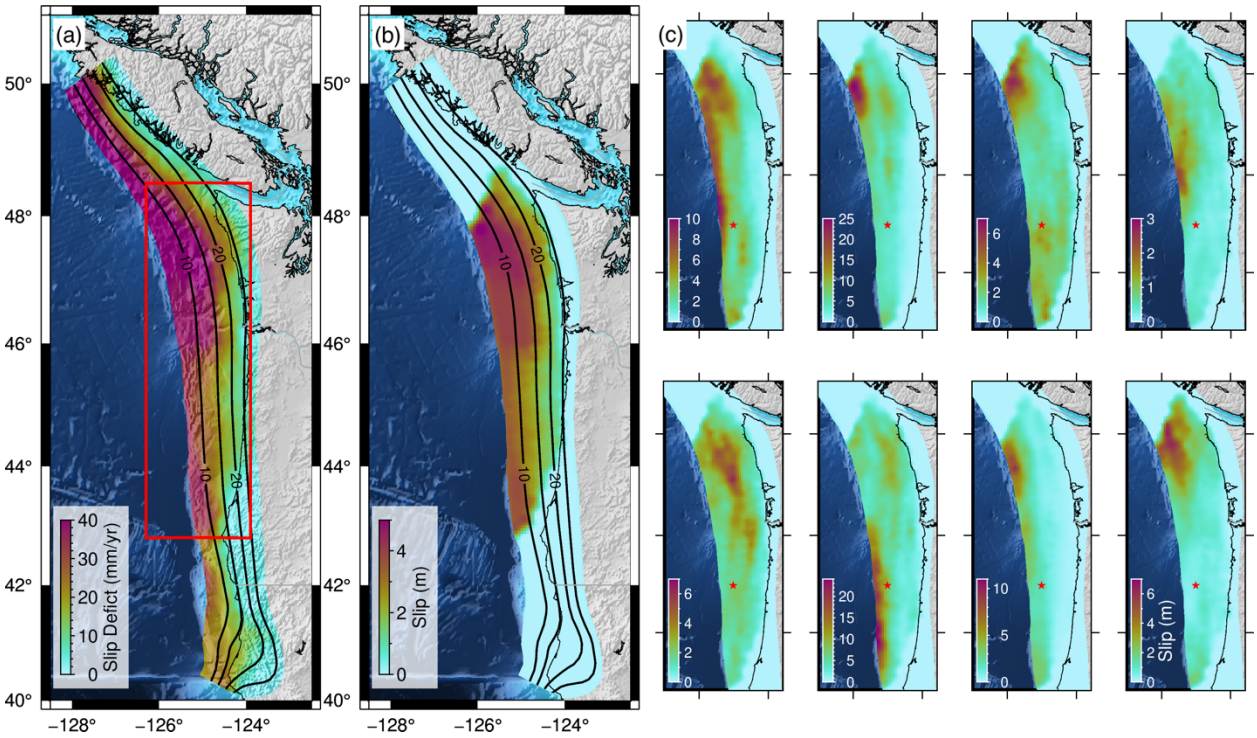

Figure 2. *Creating stochastic slip ruptures from the Gamma coupling model. (a) Gamma coupling model where the red box outlined contains the loose region randomly obtained from the probabilistic scaling laws for modeling ruptures. (b) Mean slip determined from the 8 M8.7 rupture models imaged on the right. Everywhere is defined by zero slip except the rupture area. The modeled ruptures are constrained by the same magnitude, correlation lengths, and hypocentral location. The desired mean slip (μ) in the K-L expansion is defined from the Gamma coupling model. (c) suite of 8 rupture models all defined by the same rupture area from (a) and the desired mean slip from (b). Stars in (c) denote location of hypocenter.*

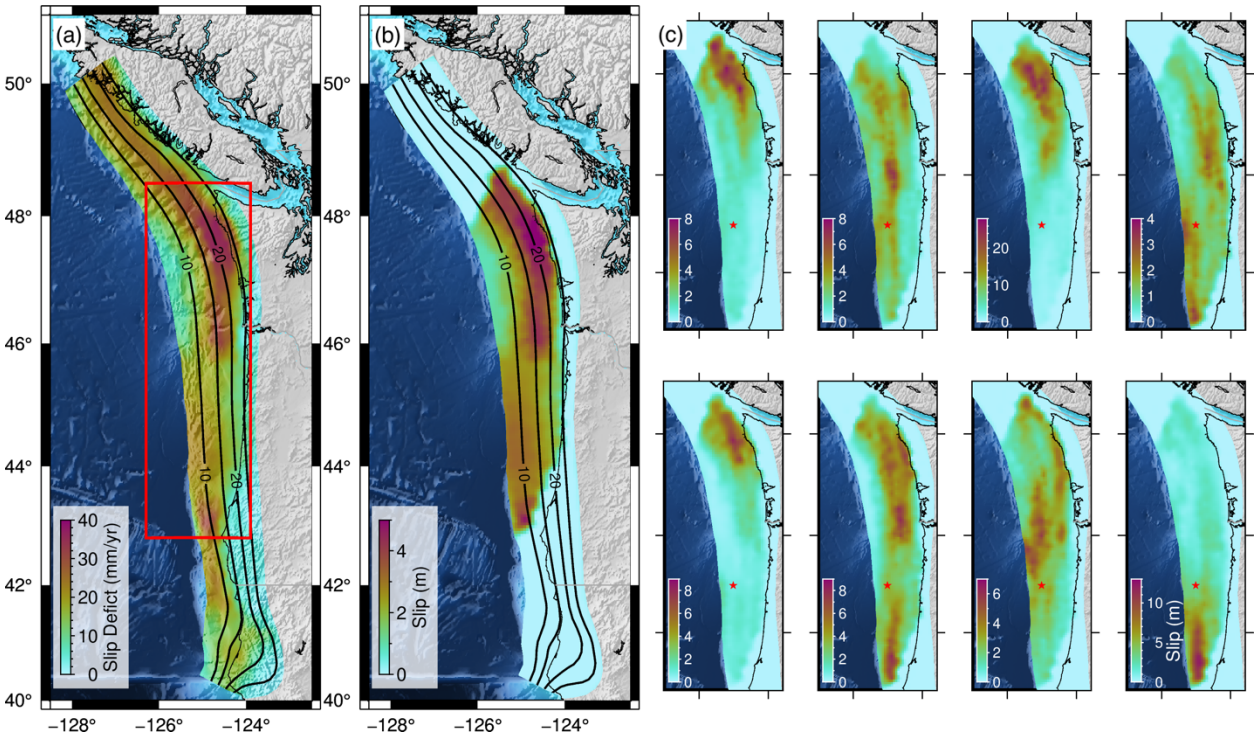

Figure 3. *Creating stochastic slip ruptures from the Gaussian coupling model. Same as Figure 2 but with the Gaussian coupling model included in the rupture modeling.*

To carry out these stochastic realizations constrained by a non-homogeneous mean model we modified the open access forward rupture modeling FakeQuakes module which is part of the forward modeling and inversion code MudPy (Melgar, 2020; Melgar & Bock, 2015; Melgar, LeVeque, et al., 2016). Two-hundred stochastic slip ruptures for 0.1 magnitude bins ranging between M7.8 and M9.1 are modeled for the Gamma, Gaussian, 30 km depth, and 1 cm/yr class scenarios (Figure 1). Following the K-L expansion approach, slip on triangular subfaults are determined using all eigenmodes. Ruptures are fixed to the given desired magnitude and have a mean rake of 90 in order to account for pure thrust motion. Following Graves and Pitarka (2015), we introduce some stochastic variability around the rake value as well. The hypocentral location is also randomly assigned from the selected subfaults. The location of the slip area and the hypocentral location are unconstrained, allowing ruptures to be equally likely anywhere along-strike on the megathrust. Additionally, the degree of slip on a single subfault was given an upper bound of 100 m of slip. Given the two presented coupling models, accumulation of 100 m of slip deficit would take well over 300 years (the time since the last large rupture), however, we consider this to allow for ruptures within a given magnitude bin to vary quite drastically between

scenarios. For the rupture classes that follow more traditional stochastic slip modeling, no tapering of slip downdip is applied. Figures 2 and 3 shows one example of the resulting rupture models calculated using the Gamma and Gaussian model implemented in the stochastic rupture modeling. Although the coupling model is applied as the desired mean slip, variations in rupture slip patterns and resultant displacements are present and are further discussed later.

2.2.3 Tsunami Modeling and Hazard Curves

For each rupture coseismic vertical displacements at the surface are determined using the analytical solution for angular dislocations for triangular subfaults in an elastic half space (Comninou & Dundurs, 1975). This method is an adaptation from the Okada equations (Okada, 1985), which focus on rectangular subfaults. The resulting vertical deformation patterns for 2 scenarios is depicted in Figure 4. This calculated deformation is then used as the initial condition for tsunami modeling. Here we use the finite volume 2D depth-averaged, non-linear tsunami modeling code GeoClaw (http://www.clawpack.org/geoclaw) (LeVeque, George, et al., 2011). Since rupture propagation velocities are much faster than tsunami wave velocities, we assume instantaneous rupture as the initial condition for the system of partial differential equations. This assumption has a negligible effect on near-source modeling as discussed in Williamson, Melgar, and Rim (2019). Topography and bathymetry from the SRTM15 relief model sampled at 15 arcseconds (Tozer et al., 2019) are used in the tsunami modeling. For each scenario we modeled wave propagation for 4 h after rupture initiation, as we are only interested in the variability of regional arrivals. One of the powerful functions of GeoClaw is the adaptive mesh refinement (AMR) which makes the simulations efficient so that more intricate and complex tsunami characteristics are represented by the finest bathymetric resolution and more simple waves are adaptively coarser. We used four levels of refinement with the coarsest level at 3 arcminutes and the finest level at the 15 s of the topography/bathymetry data. Time stepping is variable and determined automatically to guarantee numerical stability by enforcing a Courant-Friedrichs-Lewy (CFL) condition of 0.75.

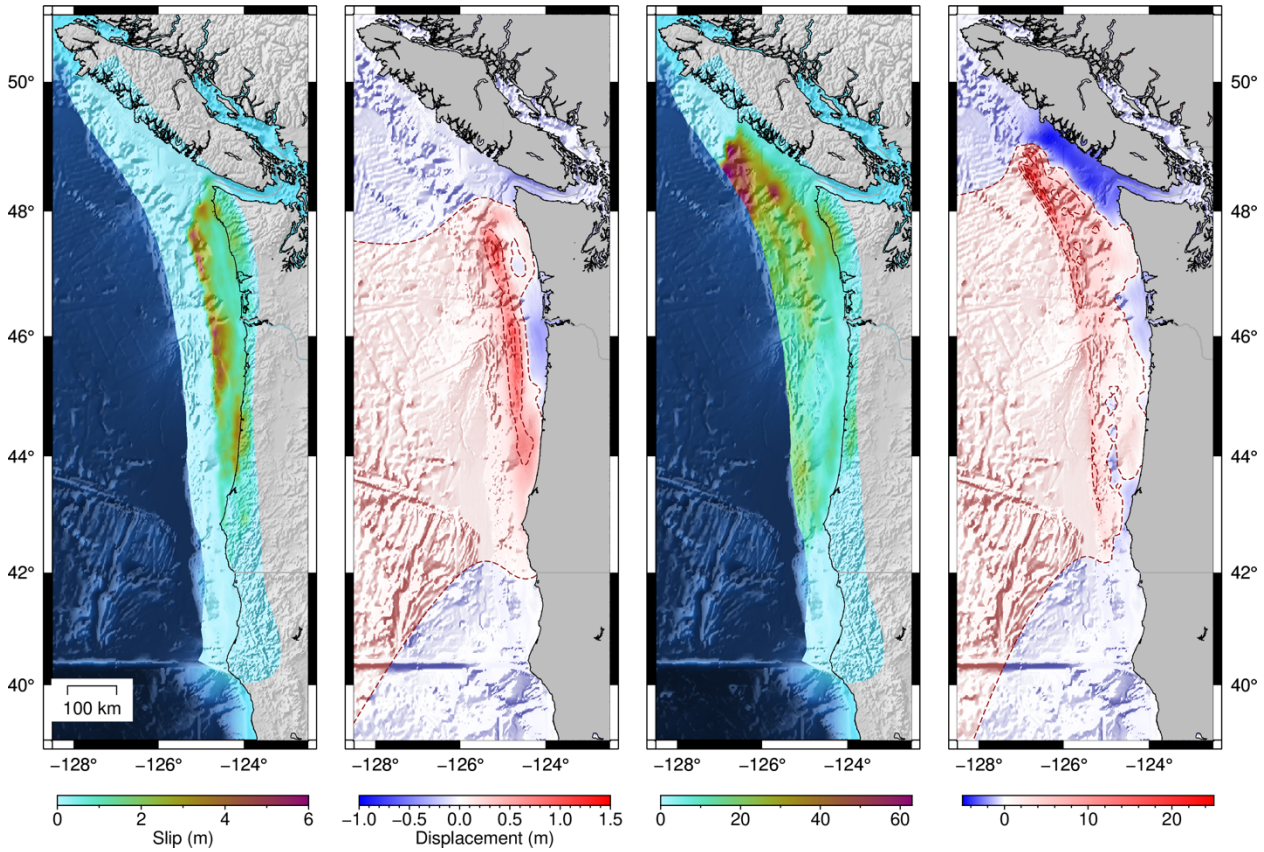

Figure 4. *Example rupture scenarios for M8.3 and M9.1 with implementation of the Gamma decade-scale coupling model. Panels (a and c) both express total coseismic slip on the fault from each scenario. Panels (b and d) express surficial coseismic vertical displacement from the two scenarios. Contours are spaced at 0.5 and 5 m increments for the M8.3 and M9.1 respectively. Dark red contours map vertical uplift and dark blue maps subsidence. Onshore portions are masked over in order to remove interpretations of secondary artifacts.*

We collect output from the model at 1,026 virtual tide gauge points between 39.5° and 50.8° latitude along the coasts of northern California, Oregon, Washington, and Vancouver Island in British Columbia. The gauge points have variable depths offshore, so, in order to homogenize them to a common reference depth we use Green's law to re-scale the wave amplitudes to 1 m depth. Example tsunami models are shown in Figure 5 for the two rupture scenarios detailed prior.

Hazard curves and resulting hazard maps are calculated and reflect the probability of exceedance of tsunami arrival amplitudes for each coastal point over a given return interval. Inherently in the formulation of the hazard curves is the assumption of the time-dependency of

earthquake occurrence. We assume a magnitude-time dependent relationship defined by the Gutenberg-Richter (G-R) distribution,

$$N = 10^{a-b*M_w} ,$$

where N is the number of yearly events for a given magnitude. The constants a and b are assumed to have values of 6.279 and 1, respectively. These values are used because they produce a return period of 526 years for M9 earthquakes. This aligns reasonably well with what is expected for the return period of M9 events for the CSZ from the paleoseismic record (e.g., Goldfinger, Galer, et al., 2017; Goldfinger, Nelson, et al., 2012). It should be noted that the applicability of the G-R distribution breaks down at lower magnitudes for the CSZ, however, since we are not focused on an authoritative hazard assessment for the region, we still employ it for the study. For results to be used for authoritative hazard assessment, other magnitude-frequency distributions should also be considered, for instance, the tapered GR distribution (Rong et al., 2014). Another potential approach is to use expert opinion to build logic trees with suitable rates for different magnitudes (e.g., Frankel, Chen, et al., 2015).

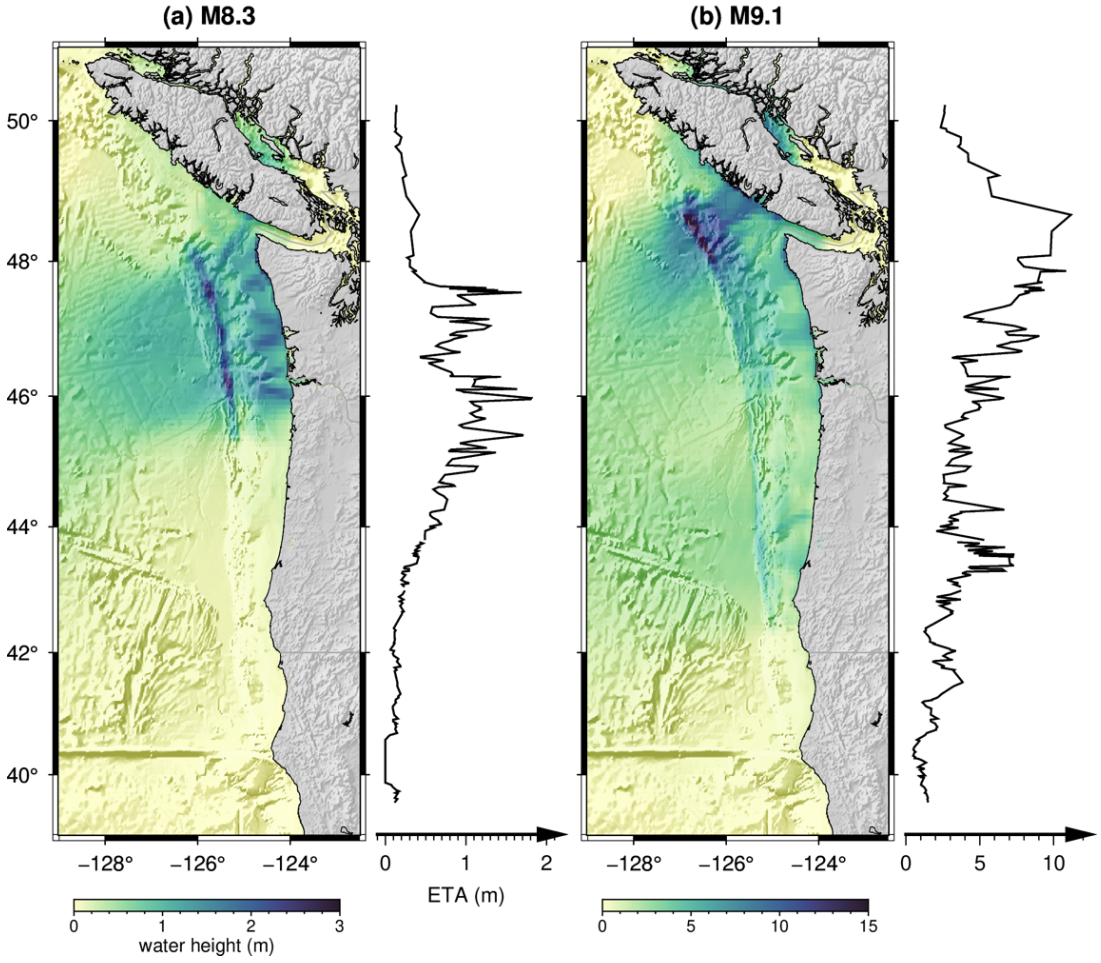

Figure 5*. Maximum sea surface heights observed during tsunami model runs for the M8.3 and M9.1 examples from Figure 4. The adjacent scatter plots to each model show the estimated coastal tsunami amplitudes (ETA) for the 1,026 gauge points.*

After assuming the rates at which earthquakes occur for every coastal location, we compute $P(\eta > \eta_c)$, the probability of the tsunami amplitude at the coast, η, exceeding a given threshold, η_c. Following Geist and Parsons (2006),

$$P(\eta > \eta_c) = 1 - \prod_{i=1}^{k}[1 - (1 - \mathrm{e}^{-\mathrm{N_i}t})P(\eta > \eta_c|M_i)] \ .$$

Here the product operates over K magnitude bins. In our case, there are fourteen bins for Mi = [7.8,9.1] with 0.1 magnitude units between bins. t is the chosen return interval of interest and Ni is the rate at which earthquakes in a given magnitude bin are assumed to occur from the G-R distribution. Finally, $P(\eta > \eta_c)$ is M the conditional probability that the tsunami exceeds the threshold given that earthquakes of a certain magnitude occur. Following Melgar, Williamson, and Salazar-Monroy (2019) this value is obtained empirically from the amplitudes produced at a given point by the 200 tsunami runs in each magnitude bin.

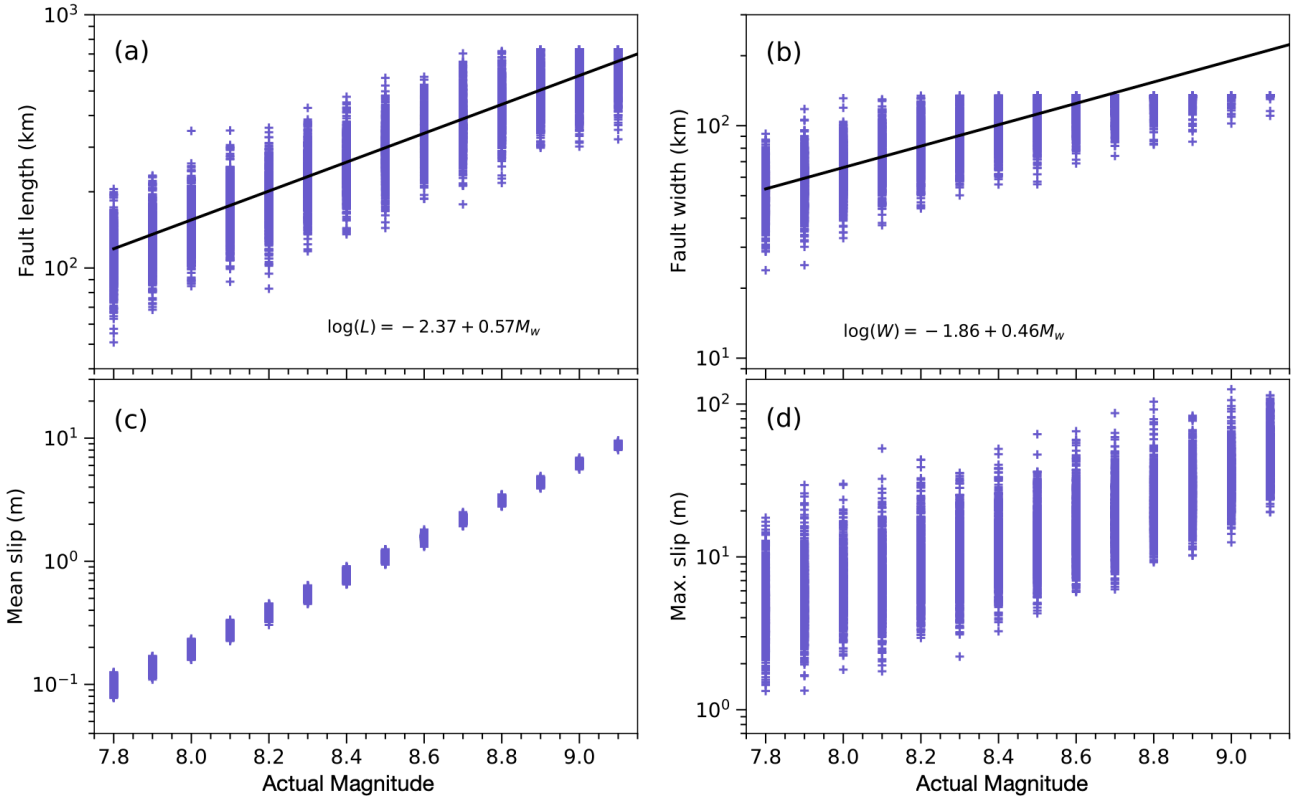

Figure 6. *Statistical summary of all ruptures generated, regardless of model. (a) Fault length, (b) fault width, (c) mean slip of all subfaults, and (d) maximum slip. The black line in panels (a and b) are the scaling laws for length and width of rupture from Blaser et al. (2010).*

2.3 Results

Here we present the results of the 11,200 rupture scenarios and tsunami models created. Our focus is on highlighting how different assumptions on coupling contribute to the estimated hazards, so only coastal tsunami amplitudes are considered. We initially present each model separately, highlighting key features so that comparison between model results is clearer.

Although the rupture area and distribution of slip vary in size for a given magnitude bin, both the rupture area and maximum amount of slip on a subfault does on average increase with magnitude for each model following known scaling laws (Figure 6). At larger magnitudes, events begin to saturate in both length and width due to the actual CSZ fault dimensions. As a result of the von Karman ACF, slip is focused around asperities of favorable length scales, and as stated

prior, asperity size predominantly scales with increasing magnitude. The stochastic nature of the models partitions and redistributes the asperities throughout the rupture extent. Irrespective of the presence of coupling models, ruptures varied between one another. Inherent to the stochastic nature of the rupture modeling, presence and influence of the coupling models is not always immediately obvious for an individual rupture; however, when all ruptures were combined into an averaged slip model, the result subsequently resembles the given desired mean slip model μ (Figures 2b and 3b).

Figure 7 shows summary violin plots of the coastal amplitudes for each of the coupling models assumed and for the no coupling model cases. Each violin represents the kernel density estimate of the distribution of tsunami heights that is possible for a magnitude range at that specific point. Unsurprisingly, within all models calculated, the coastal tsunami arrivals on average increase in response to increasing rupture magnitude irrespective of the coastal latitudinal location. At lower magnitude scenarios (e.g., M8.4) arrival height differences are not as obvious between models. Slight variations in tsunami arrival amplitudes are present at lower magnitudes. Once magnitudes become great enough (~M8.6) and larger swaths of the megathrust participate, differences in the coastal amplitudes that correlate to the particularities of the assumed coupling model become more obvious. The southern extent (below 43° latitude) of the study area on average experiences smaller variations between all classes, even at larger magnitudes. However, the resulting tsunami amplitude variations become increasingly prominent in the northern extent (46°–48° latitude) of the study area off the coast of Washington in comparison to the southern extent.

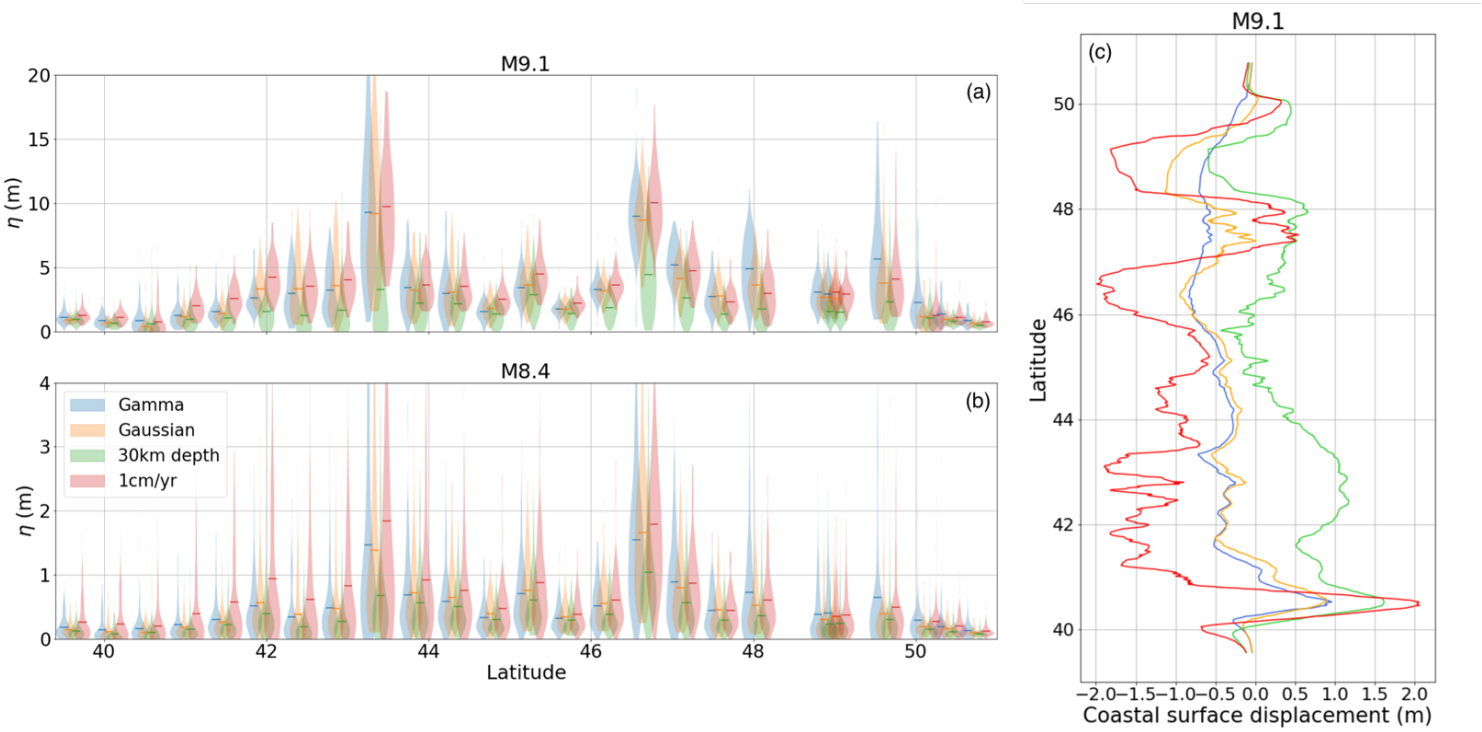

Figure 7*. Tsunami amplitudes along the coast for each rupture class. (a and b) Violin plots showing the density spread of the coastal tsunami amplitude,η, for selected virtual tide gauge points for M9.1 and M8.4 bins. Central bar for each model is the mean value of arrivals for the given magnitude bin. (c) Mean coastal surface displacements for all M9.1 bin ruptures. Negative is subsidence and positive is uplift. Colors refer to legend in (b).*

The Gamma scenarios, which assume larger and shallower offshore coupling, experience the largest tsunami amplitudes in the northern extent, whereas the southern extent is more dominantly subdued in the observed arrivals. The fully coupled zone in the Gamma model may extend throughout the entirety of the trench, but the total area of full coupling is widest starting at about 46° latitude and continuing to the edge of the study area. This separation matches well with the divide between the two regions of southern and northern arrival heights. For instance, at M9.1, the arrival is typically ~1–3 m in the southern region whereas they are ~4–6 m on average in the northern region.

Unlike the Gamma model, there is not as clear of a separation of zones of high and low estimated tsunami amplitudes for the Gaussian coupling model. Interestingly, the Gaussian

decade-scale coupling model contains a prominent region of coupling apparent in both the southern and northern region of the subduction zone; yet unlike the Gamma model, coupling here occurs between 15 and 25 km downdip at its highest coupling ratio. There is a deficiency of slip along the trench in the northern region in comparison to the Gamma model (46°–48°). Although large slip occurs closer to the coast in these scenarios, it also occurs much deeper than the previous models, limiting the surface displacement response and therefore producing a smaller volume of displaced water leading to overall smaller amplitude tsunamis (Figure 7). Tsunami amplitudes between the Gaussian and Gamma models appear relatively similar throughout the model region except near the Olympic Peninsula where coupling model differences are more pronounced.

The 30 km depth class does not see a prominent distinction between regions for the tsunami arrivals. There is a slight increase in the amplitude of arrivals in the northern gauge points than the southern (Figure 7), similar to but less obvious than in the previous two models. Mean recorded gauge point amplitudes do not exceed 4 m even for M9.1 events. Since these models lack any form of constraints to favor slip in particular regions along the slab interface, there is no distinction in the probability of activation of slip at any given subfault. With that in mind, mean consequential tsunamis arrivals should only vary due to the bathymetry and shape of the coastlines and should therefore have smaller variability laterally along the coast as a result of the ruptures themselves.

This is similarly true for the 1 cm/yr class, however, more heterogeneity in amplitudes is present due to the more variable nature of the downdip limit. In the southern region, this class is constrained by a much shallower limit (~15 km) than the northern region (~25 km), limiting the region of slip to occur almost completely offshore in the south (Figure 1). Tsunami arrivals are more similar between the 1 cm/yr class and the two coupling classes. The 1 cm/yr class produces tsunami amplitudes typically ~1 m greater than the Gamma class for M9.1 ruptures in southern Cascadia. In the north, however, this distinction reverses, where the Gamma (and less abundantly Gaussian) class produces slightly larger arrival heights than the 1 cm/yr class.

Coastal subsidence patterns, which influences observed tsunami hazards, vary widely between classes. For all rupture classes except the deeper 30 km depth class, the coast predominantly experiences subsidence (Figure 7). The mean coastal subsidence measurements for the Gaussian and Gamma models are strikingly similar in the southern region. In the Olympic

Peninsula (47°–49°) coastal subsidence values vary more appreciably between the two. The 1 cm/yr class produces on average stronger coastal subsidence throughout the coastal region. This is most notable in the southern extent (41°–43°).

2.4 Discussion

Regardless of rupture class, the ruptures varied considerably between model scenarios for any given magnitude bin. The two different assumed coupling models clearly show differences in the depth dependence of slip. Figure 8 depicts three depth-averaged slip cross-sections for each assumed coupling model for all M8.8–M9.1 ruptures. As expected, the ruptures with a homogeneous mean model (no assumed coupling) contain almost no depth dependency for slip other than the imposed depth limit. This then allows slip to propagate as deep as the downdip limits and therefore slip is as probable to occur in these deeper regions as it is close to the trench. Mean slip varies considerably between these depth constrained models. For instance, in the southern region, where the 1 cm/yr class has a depth limit near the 15 km contour (Figure 1c), mean slip is almost twice as high compared to the 30 km depth class. Meanwhile, for the cases where a coupling pattern is imposed, there is a clear connection between the amount of slip and depth of the slab. The depth dependency of both the ruptures with imposed Gamma and the Gaussian coupling models becomes synonymous to the distribution of coupling for the two regions. In the northern and southern regions of the CSZ where slip deficit is the highest for both models, a dominantly monotonic decrease in amount of slip is seen for the Gamma class and pseudo-Gaussian slip shape is seen for the Gaussian class. As a result of this, the Gamma class experiences far greater slip shallower in depth when compared to the other classes, directly affecting the tsunami generation as seen in the hazard curves and the hazard map (Figures 9 and 10). Areas associated with the smallest coupling ratio see very little slip, predominantly in the southern region of the CSZ. Along strike variations in slip concentration are also present between the models where coupling is included (Figures 2, 3 and 8).

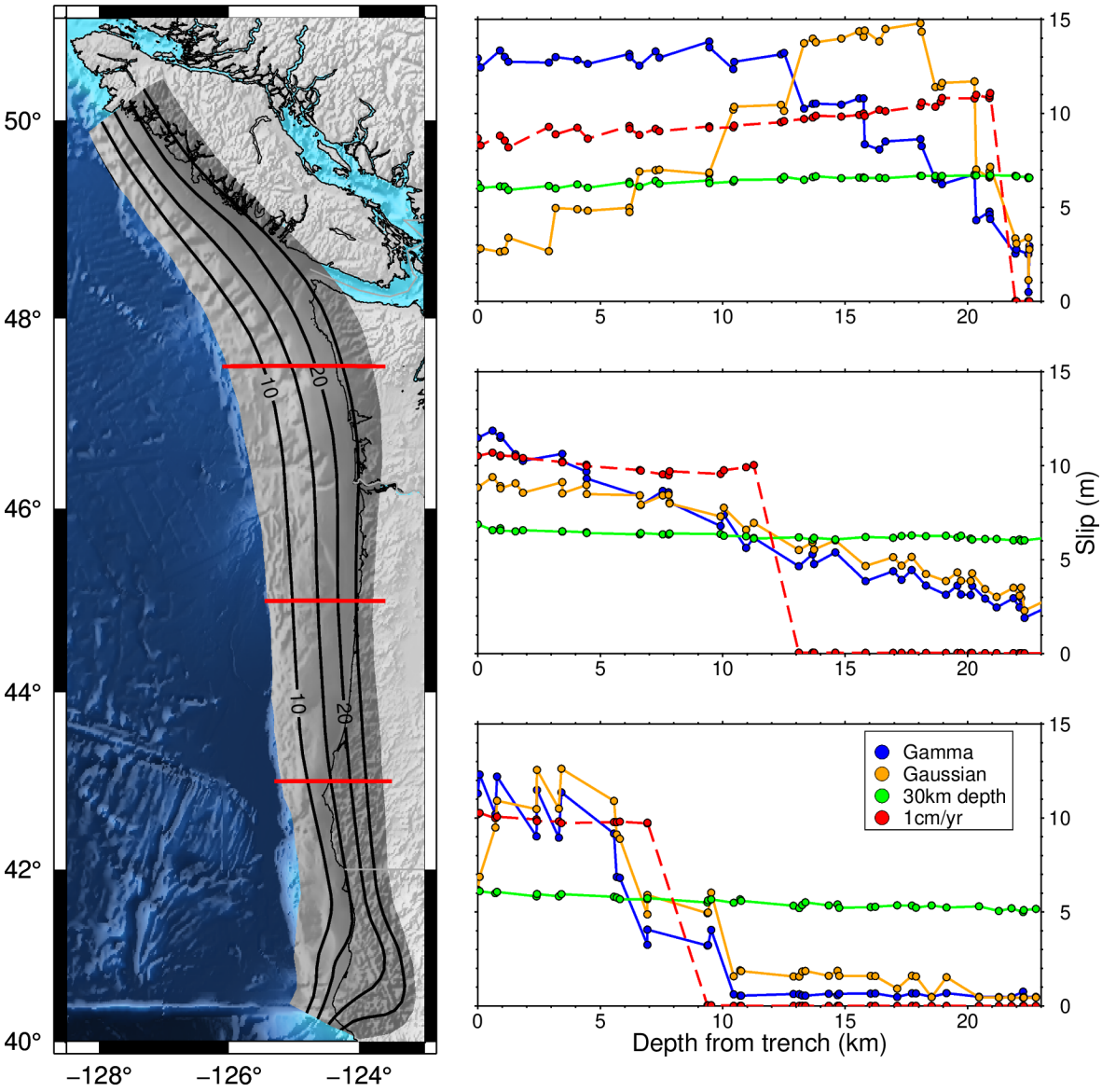

Figure 8. *Mean slip as a function of depth. (a) CSZ, with depth of slab contour intervals at 5 km. Red horizontal lines labeled P1, P2, and P3 depict the locations of the three profiles in the adjacent plots at 47.5°, 45°, and 43° latitude. (b) Profiles depicting slab depth with respect to trench versus mean slip for 800 ruptures between M8.8 and M9.1 between 47.3° and 47.7° latitude for each of the four classes. Gamma, Gaussian, 30 km depth, and 1 cm/yr classes here are depicted as orange, blue, green, and red respectively. Points on each line are the model values at each triangular subfault in the region. (c) The same as (b) but for the region of 44.8°–45.2°. (d) Same as previous but for the region of 42.8°–43.2°.*

Coastal subsidence is prevalent in three of the four classes to a varying degree, for the 30 km depth class, the coastal signal is dominated by uplift (Figure 7). In recent work by Wirth and Frankel (2019) where they model coseismic uplift for M9.0–M9.2 CSZ megathrust events and compare them with coastal subsidence records tied to the 1700 Cascadia event, a dominance of coastal subsidence is recorded for ruptures with down-dip rupture limits corresponding to the 1 cm/yr locking contour. Although at current, coseismic uplift data for the CSZ is restricted to a finite number of locales (∼20 in total) based on paleoseismic estimates (e.g., Kemp et al., 2018; P. L. Wang et al., 2013), we would expect that similar trends in our models would add confidence to constraining class applicability. Since the 30 km depth class is dominated by coastal uplift, it seems more likely that this reference model may produce potential ruptures that are less likely to occur in the CSZ. This then adds weight to the importance of coupling for constraining ruptures, since even the 1 cm/yr class is based in some aspect on local coupling patterns.

It is important to reiterate that the coupling fraction does not perfectly correlate to where the slip occurs for any given rupture. Rather, the coupling as implemented here (Equation 9) will define regions where slip is more likely or less likely to occur. Since there is a sparse record of the earthquake history of the CSZ, coupling should only be used as a first order constraint. Further research on more earthquake cycles, past and future, will then allow us to better constrain the accuracy and applicability of coupling as it relates to the rupture characteristics.

Additionally, in our implementation we have assumed that a coupling ratio of 0 (fully creeping) corresponds to parts of the megathrust that cannot participate in the coseismic process. However, recent modeling studies have argued that dynamic effects can push the rupture into transition regions of the subduction zone. Areas of 0 coupling may, under certain circumstances, participate seismically (Ramos & Huang, 2019). An example in recent is the July 2020 M7.8 earthquake off the Alaskan-Aleutian arc is believed to have ruptured in the eastern portion of the previously assumed, seismically uncoupled Shumagin Gap (Crowell & Melgar, 2020). Observational studies have also shown potential overlap between regions with slow slip and regions with coseismic slip (e.g., Lin et al., 2020). However, since the dynamic effects and their influences in rupture propagation into transition zones are not yet well understood in terms of what controls them and how to quantify their likelihood of occurrence, we do not include them in the rupture modeling process. This has little effect on PTHA since shallow slip contributes far

more to the overall hazard. However, for other applications it is potentially important as it would allow for slip further inland and closer to large population centers on the CSZ.

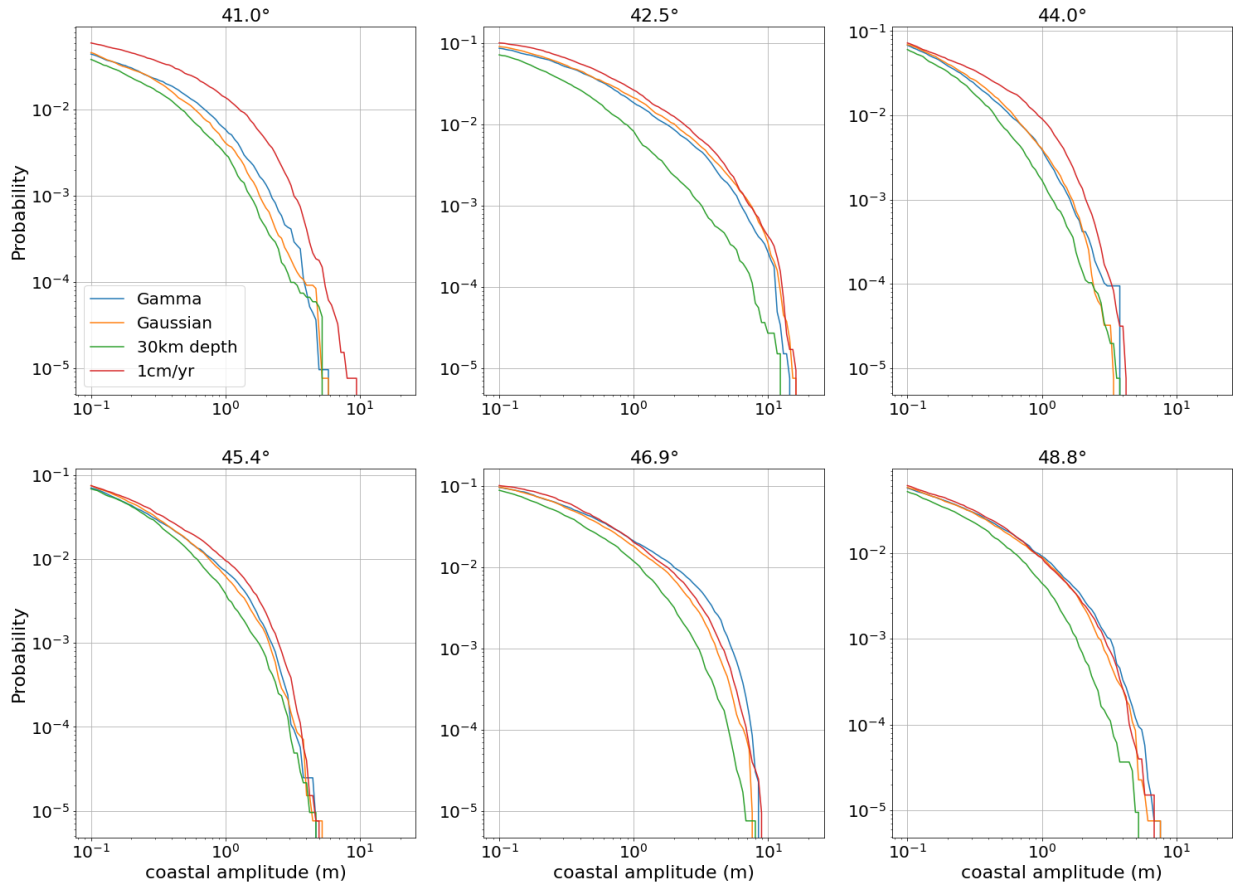

Figure 9. *Hazard curves of a 1 year return period for six coastal gauge points with locations depicted in Figure 10. The four distinct classes are colored accordingly. Curves are determined using a magnitude time distribution defined by the Gutenberg-Richter scaling relation and the method is described previously. It should be noted that the GR distribution does not constrain CSZ seismicity well at lower magnitudes. For more authoritative hazard assessments, other distributions should be explored.*

Following the rupture model patterns, the associated tsunami hazards tend to increase toward the north of the study area. Figure 9 shows hazard curves at six coastal locations (shown in Figure 10) for a 1 year return period. These curves give a good quantitative measure to the associated tsunami hazards for the rupture models. Although these are site specific, it becomes

quite clear that there are pronounced effects in the associated hazards when coupling is included in modeling. Differences in probabilities of even a relatively small tsunami (<1 m) are apparent between the 30 km depth class and the other three classes, however, for several gauge points throughout the region, distinguishing between the other three are difficult. Because hazard curves are site specific, associated hazards can vary between points in larger regions. In the southern and central CSZ, the 1 cm/yr produces more probable large tsunamis and the two coupling classes produce similar probabilities (Figures 9 and 10). Recall that for the 1 cm/yr class, slip in this region is more shallowly constrained (15–20 km) than the other classes. Similarly, in the central portion of the subduction zone interface between 44° and 46° latitude (Figure 1), the slip deficit is much smaller, and therefore the coupling ratio is much smaller.

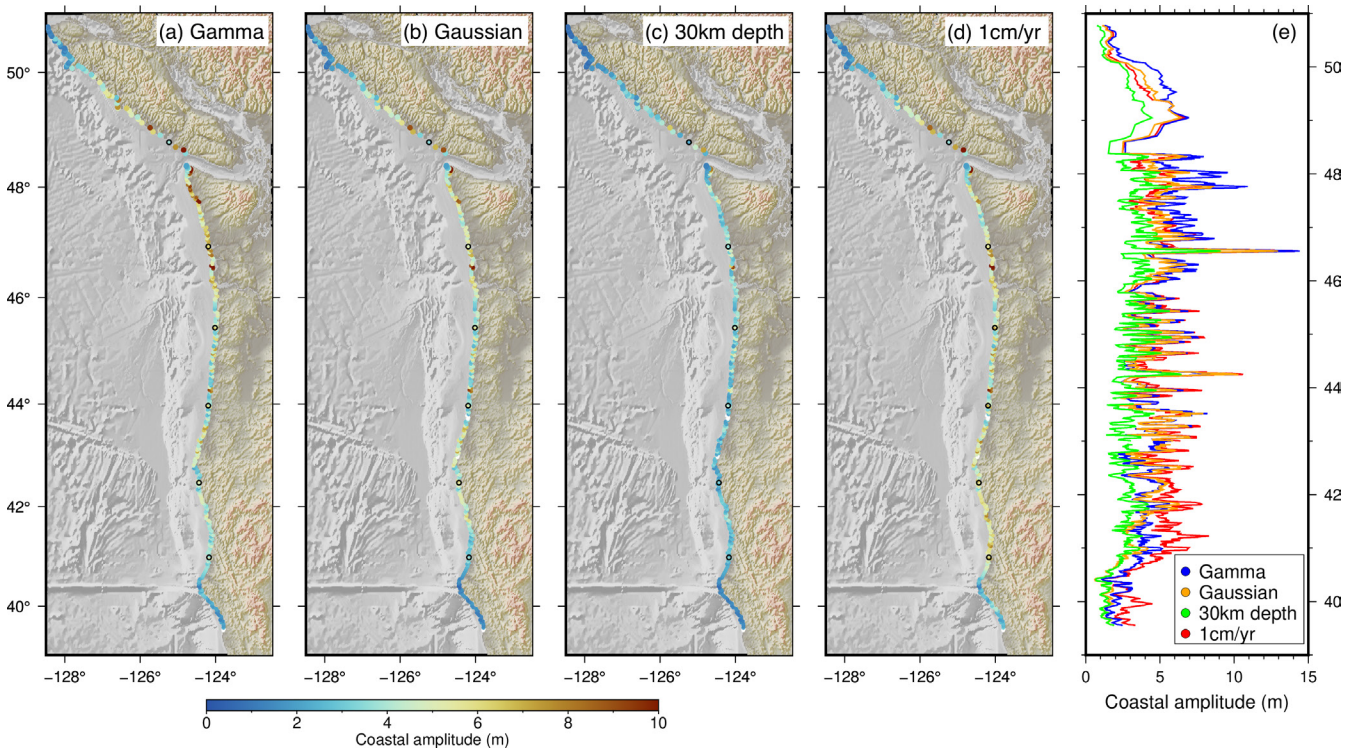

Figure 10. *Hazard maps for the four classes showing the 2% probability of tsunami threshold exceedance for a 50 year return period at each of the 1,026 modeled coastal gauge points. (a) Gamma coupling model, (b) Gaussian coupling model, (c) 30 km depth, and (d) 1 cm/yr. Color scale describes η for each gauge point. (e) η at each gauge point location in latitude for the four classes.*

Tsunami amplitude arrivals and associated hazards between the two coupling classes are variable throughout the coastal region, with the most pronounced variations in the southernmost region near California and the northern region of the Olympic Peninsula. This is highlighted by the 2% probability of exceedance in 50 years hazard maps for the four classes depicted in Figure 10. The stark difference in amplitudes in the north highlights the effects the coupling models have on the ruptures. Between 46° and 42° latitude the Gaussian and Gamma coupling models have similar patterns of coupling. At higher latitudes, where the slab bends and the slab dip shallows, coupling varies more noticeably, with the strongest coupling for the Gaussian model occurring between 15 and 25 km depth and the Gamma model is strongly coupled from 15 km all the way to the trench. With larger and shallower coupling regions in the Gamma model, more slip is observed closer to the trench (Figure 8) and therefore the resulting tsunamis appear much larger.

The hazard variability along strike observed in the stochastic slip models without imposed coupling is associated with variations present in the downdip limit of slip, tsunami propagation path, and the site conditions (the shape of the coastline). The tsunami path and site conditions are dominantly controlled by the bathymetry and distance from the tsunami initiation loci to the coast. The influence of the surficial expressions in hazard generations are the only sources of variability for the downdip limit classes, whereas the models with coupling are more heterogeneous. Around 44° latitude, the distance of the trench to the coast begins to widen quite drastically and the bathymetry becomes more heterogeneous over a larger distance. The estimated tsunami amplitude for gauge points south of 44° are on average noticeably smaller than those north. For the 30 km depth class, tsunami hazards are lower than the other three classes for all coastal sites (Figure 10). This is not the case for the 1 cm/yr class. Coastal tsunami hazards associated with the 1 cm/yr class are greater for the southern region. In the norther region (above 46° latitude), the Gamma class experiences overall greater hazards than the 1 cm/yr class. In general, the differences between the coupling and 1 cm/yr classes are no greater than 1–2 m for the 2% hazard maps, yet some coastal points notice differences of 4–5 m. This variability has large implications on potential hazards and required tsunami hazard preparedness. Tsunami hazards associated with either coupling model do not vary significantly between either the Gaussian or Gamma models, but two regions of variable hazards persist: the southern Cascadia region around 41°–42° latitude as well as northern Cascadia around 47°–48° latitude.

One important point for assessing tsunami hazards in this way is whether the 200 ruptures simulated for each magnitude bin are sufficient to capture all the possible variability in the resulting tsunamis. In order to assess the statistical stability of the models, we refer to Figure 11 where the conditional probabilities, $P(\eta > \eta_c \,|M_i)$, are plotted for four magnitude bins against the number of scenarios observed. The conditional probabilities are relatively stable even after only ~100 scenarios are included, however, our results detailed prior are determined using all 200 scenarios. Although here we plot the Gamma class, the results are similar for the three other classes. A formal CSZ hazard assessment should consider whether the stability observed in these conditional probabilities is sufficient or whether more scenarios are needed.

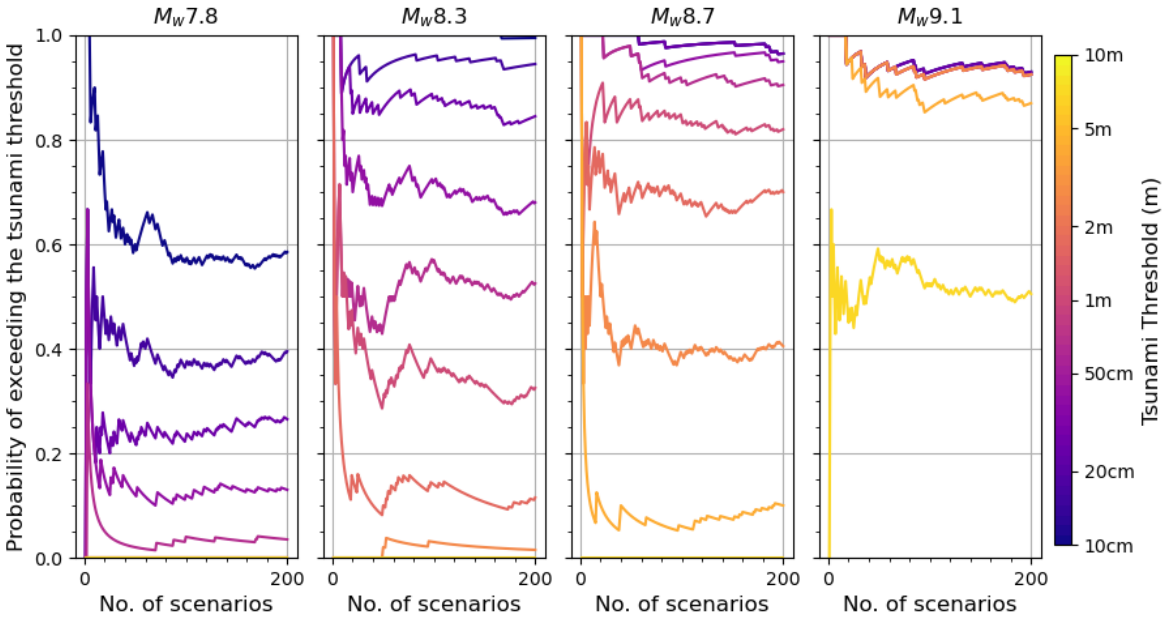

Figure 11. *Conditional probability of exceeding the tsunami threshold given that a number of scenarios has occurred for a given magnitude using the Gamma class,* $P(\eta > \eta_c|M_i)$ *. Four different magnitude bins are depicted, all plotted for the gauge point at 46.9° latitude (Figures 9 and 10). The other three rupture classes produce similar probable stabilities at around 100 scenarios.*

We note as well that we have assumed a fairly simple geometry for the shallow most megathrust with no splay faults. These have been inferred to exist in the CSZ (Booth-Rea

et al., 2008) and coseismic motion on them can have a significant effect on the resulting tsunami (e.g., Gao et al., 2018). Similarly, we have considered only simple elastic deformation. Distributed deformation of the heavily sedimented deformation front (Han et al., 2017) could affect the ensuing tsunami as has been noted in places like Indonesia (Hill et al., 2012). Likewise, plastic deformation of the wedge can increase the amount of vertical deformation and lead to larger than expected tsunami (Ma & Nie, 2019).

The results discussed above are a compelling argument to include the influence of coupling for both the possible slip and rupture geometry generated as well as the subsequent tsunami hazards. However, without stronger confidence in the specifics of the coupling for the region, large uncertainties are still present. The two coupling models included here differ significantly, especially in the near-trench region. There is currently no way to distinguish between them because they produce the same onshore inter-seismic velocity field (Schmalzle et al., 2014). Additionally, there are other potential coupling models for the region (e.g., D. Li & Liu, 2016; S. Li, Wang, et al., 2018; Michel et al., 2019) which include different assumptions, such as long-term viscoelastic relaxation of the upper mantle. Nonetheless, the two models we have used here, can be thought of as depicting two end member cases of the possible coupling distribution throughout the CSZ. The other existing coupling models share similar features to either of these two. Although dominant similarities are present between the ruptures and hazards associated with the coupling models, larger-scale variations are present. This large uncertainty between models highlights the necessity of the community to further seafloor instrumentation and seafloor geodesy in order to constrain the shallow coupling. Constraining coupling using hybrid modeling of both on land and seafloor geodetic instrumentation has already been implemented for the Nankai Trough along the coast of Japan (Yokota et al., 2016). Use of the coupling model present by Yokota et al. (2016) has also been implemented in tsunami wave propagation modeling from the two Kii Peninsula earthquakes of 2004 (Watanabe et al., 2018).

Finally, we note once more that these results should not be used as an authoritative hazard assessment for the CSZ. Further work remains to be done in order to improve accuracy for future applications: we have used a number of simplifying assumptions, considered only one kind of tsunami source, and cannot at this point distinguish which of the two coupling models is more likely. Our results instead highlight the large variations in rupture patterns and the resultant tsunami hazards created by including inter-seismic coupling, a key property of the megathrust.

This shows that disregarding important information, like inter-seismic coupling, in rupture modeling can lead to hazards estimates that are potentially underestimated.

2.5 Conclusion

Current stochastic rupture modeling techniques do not consider the influence of some first-order fault zone characteristics like inter-seismic coupling patterns. A correlation between high slip patches and areas of greatest coupling ratios has been noticed for recent large earthquakes on megathrusts globally and suggests that this information should be taken into account. Here we presented an updated mathematical formalism to introduce coupling models as prior information into stochastic rupture modeling. We compared two end member models of coupling, one with a fully coupled zone extending to the trench and another with coupling deeper downdip and determined the variable influence that this has on the resulting rupture models. These were compared with two classes of ruptures defined by variable downdip limits of slip: a depth limit defined by the top of the tremor zone and a shallower depth limit defined by the 1 cm/yr coupling contour (25% coupling). Large variations in slip distribution are present in the rupture models and correlate well with areas with the largest differences in slip deficit. To exemplify the importance of this the ruptures were then used in a probabilistic tsunami hazard assessment of the CSZ. We found that the tsunami amplitudes generated are more uncertain throughout the region when coupling is used to condition the rupture models when compared to the tremor zone depth condition. Hazards associated with the 1 cm/yr class were more similar to the coupling classes than the previous class, however, important variations in resultant hazards were present throughout. More specifically, in the northern extent of the CSZ, associated hazards are larger where differences in coupling distribution are more drastic. Although large uncertainties are present in the accuracy of modeled coupling, imposing either constraint created variable hazard estimations. To bridge the uncertainties in present inter-seismic coupling and therefore refine our knowledge of first order fault characteristics for future hazard assessments, expanded seafloor instrumentation is vital.

References Cited

Barnhart, W. D., Murray, J. R., Briggs, R. W., Gomez, F., Miles, C. P., Svarc, J., et al. (2016). Coseismic slip and early afterslip of the 2015 Illapel, Chile, earthquake: Implications for frictional heterogeneity and coastal uplift. Journal of Geophysical Research: Solid Earth, 121(8), 6172–6191. https://doi.org/10.1002/2016jb013124

Barrientos, S., & Pérez-Campos, X. (2018). Preface to the focus section on geophysical networks and related developments in Latin America. Seismological Research Letters, 89(2A), 315–317. https://doi.org/10.1785/0220180026

Bijelić, N., Lin, T., & Deierlein, G. G. (2018). Validation of the SCEC broadband platform simulations for tall building risk assessments considering spectral shape and duration of the ground motion. Earthquake Engineering & Structural Dynamics, 47(11), 2233–2251.

Blaser, L., Krüger, F., Ohrnberger, M., & Scherbaum, F. (2010). Scaling relations of earthquake source parameter estimates with special focus on subduction environment. Bulletin of the Seismological Society of America, 100(6), 2914–2926. https://doi.org/10.1785/0120100111

Bock, Y., & Melgar, D. (2016). Physical applications of GPS geodesy: A review. Reports on Progress in Physics, 79(10), 106801. https://doi. org/10.1088/0034-4885/79/10/106801

Booth-Rea, G., Klaeschen, D., Grevemeyer, I., & Reston, T. (2008). Heterogeneous deformation in the Cascadia convergent margin and its relation to thermal gradient (Washington, NW USA). Tectonics, 27(4).

Bürgmann, R., Kogan, M. G., Steblov, G. M., Hilley, G., Levin, V. E., & Apel, E. (2005). Interseismic coupling and asperity distribution along the Kamchatka subduction zone. Journal of Geophysical Research: Solid Earth, 110(B7). https://doi.org/10.1029/2005jb003648

Comninou, M., & Dundurs, J. (1975). The angular dislocation in a half space. Journal of Elasticity, 5(3–4), 203–216. https://doi.org/10.1007/ bf00126985

Crowell, B. W., & Melgar, D. (2020). Slipping the Shumagin Gap: A kinematic coseismic and early afterslip model of the MW 7.8 Simeonof Island, Alaska, earthquake. Geophysical Research Letters, 47(19), e2020GL090308. https://doi.org/10.1029/2020gl090308

De Risi, R., & Goda, K. (2017). Simulation-based probabilistic tsunami hazard analysis: Empirical and robust hazard predictions. Pure and Applied Geophysics, 174(8), 3083–3106. https://doi.org/10.1007/s00024-017-1588-9

Field, E. H., Jordan, T. H., Page, M. T., Milner, K. R., Shaw, B. E., Dawson, T. E., et al. (2017). A synoptic view of the third Uniform California Earthquake Rupture Forecast (UCERF3). Seismological Research Letters, 88(5), 1259–1267. https://doi.org/10.1785/0220170045

Frankel, A., Chen, R., Petersen, M., Moschetti, M., & Sherrod, B. (2015). 2014 update of the Pacific Northwest portion of the US National Seismic Hazard Maps. Earthquake Spectra, 31(1_suppl), S131–S148. https://doi.org/10.1193/111314eqs193m

Frankel, A., Wirth, E., Marafi, N., Vidale, J., & Stephenson, W. (2018). Broadband synthetic seismograms for magnitude 9 earthquakes on the Cascadia megathrust based on 3D simulations and stochastic synthetics, Part 1: Methodology and overall results. Bulletin of the Seismological Society of America, 108(5A), 2347–2369.

https://doi.org/10.1785/0120180034 Gao, D., Wang, K., Insua, T. L., Sypus, M., Riedel, M., & Sun, T. (2018). Defining megathrust tsunami source scenarios for northernmost Cascadia. Natural Hazards, 94(1), 445–469. https://doi.org/10.1007/s11069-018-3397-6

Geist, E. L., & Parsons, T. (2006). Probabilistic analysis of tsunami hazards. Natural Hazards, 37(3), 277–314. https://doi.org/10.1007/ s11069-005-4646-z

Goldberg, D. E., & Melgar, D. (2020). Generation and validation of broadband synthetic P waves in semistochastic models of large earthquakes. Bulletin of the Seismological Society of America, 110(4), 1982–1995. https://doi.org/10.1785/0120200049

Goldfinger, C., Galer, S., Beeson, J., Hamilton, T., Black, B., Romsos, C., et al. (2017). The importance of site selection, sediment supply, and hydrodynamics: A case study of submarine paleoseismology on the northern Cascadia margin, Washington USA. Marine Geology, 384, 4–46. https://doi.org/10.1016/j.margeo.2016.06.008

Goldfinger, C., Nelson, C. H., Morey, A. E., Johnson, J. E., Patton, J. R., Karabanov, E. B., et al. (2012). Turbidite event history—Methods and implications for Holocene paleoseismicity of the Cascadia subduction zone (No. 1661-F). US Geological Survey.

Graves, R., Jordan, T. H., Callaghan, S., Deelman, E., Field, E., Juve, G., et al. (2011). CyberShake: A physics-based seismic hazard model for southern California. Pure and Applied Geophysics, 168(3–4), 367–381. https://doi.org/10.1007/s00024-010-0161-6

Graves, R., & Pitarka, A. (2015). Refinements to the Graves and Pitarka (2010) broadband ground-motion simulation method. Seismological Research Letters, 86(1), 75–80. https://doi.org/10.1785/0220140101

Grezio, A., Babeyko, A., Baptista, M. A., Behrens, J., Costa, A., Davies, G., et al. (2017). Probabilistic tsunami hazard analysis: Multiple sources and global applications. Reviews of Geophysics, 55(4), 1158–1198. https://doi.org/10.1002/2017rg000579

Grezio, A., Cinti, F. R., Costa, A., Faenza, L., Perfetti, P., Pierdominici, S., et al. (2020). Multisource Bayesian probabilistic tsunami hazard analysis for the Gulf of Naples (Italy). Journal of Geophysical Research: Oceans, 125(2), e2019JC015373. https://doi.org/10.1029/2019jc015373

Han, S., Bangs, N. L., Carbotte, S. M., Saffer, D. M., & Gibson, J. C. (2017). Links between sediment consolidation and Cascadia megathrust slip behaviour. Nature Geoscience, 10(12), 954–959. https://doi.org/10.1038/s41561-017-0007-2

Hayes, G. P., Moore, G. L., Portner, D. E., Hearne, M., Flamme, H., Furtney, M., & Smoczyk, G. M. (2018). Slab2, a comprehensive subduction zone geometry model. Science, 362(6410), 58–61. https://doi.org/10.1126/science.aat4723

Hill, E. M., Borrero, J. C., Huang, Z., Qiu, Q., Banerjee, P., Natawidjaja, D. H., et al. (2012). The 2010 Mw 7.8 Mentawai earthquake: Very shallow source of a rare tsunami earthquake determined from tsunami field survey and near-field GPS data. Journal of Geophysical Research: Solid Earth, 117(B6). https://doi.org/10.1029/2012jb009159

Kemp, A. C., Cahill, N., Engelhart, S. E., Hawkes, A. D., & Wang, K. (2018). Revising estimates of spatially variable subsidence during the AD 1700 Cascadia earthquake using a Bayesian foraminiferal transfer function revising estimates of spatially variable subsidence. Bulletin of the Seismological Society of America, 108(2), 654–673. https://doi.org/10.1785/0120170269

Konca, A. O., Avouac, J. P., Sladen, A., Meltzner, A. J., Sieh, K., Fang, P., et al. (2008). Partial rupture of a locked patch of the Sumatra megathrust during the 2007 earthquake sequence. Nature, 456(7222), 631–635. https://doi.org/10.1038/nature07572

LeVeque, R. J., George, D. L., & Berger, M. J. (2011). Tsunami modelling with adaptively refined finite volume methods. Acta Numerica, 20, 211–289. https://doi.org/10.1017/s0962492911000043

LeVeque, R. J., Waagan, K., González, F. I., Rim, D., & Lin, G. (2016). Generating random earthquake events for probabilistic tsunami hazard assessment. In Global tsunami science: Past and future (Vol. 1, pp. 3671–3692). Birkhäuser. https://doi.org/10.1007/s00024-016-1357-1

Li, D., & Liu, Y. (2016). Spatiotemporal evolution of slow slip events in a nonplanar fault model for northern Cascadia subduction zone. Journal of Geophysical Research: Solid Earth, 121(9), 6828–6845. https://doi.org/10.1002/2016jb012857

Li, L., Switzer, A. D., Chan, C. H., Wang, Y., Weiss, R., & Qiu, Q. (2016). How heterogeneous coseismic slip affects regional probabilistic tsunami hazard assessment: A case study in the South China Sea. Journal of Geophysical Research: Solid Earth, 121(8), 6250–6272. https://doi.org/10.1002/2016jb013111

Li, S., & Freymueller, J. T. (2018). Spatial variation of slip behavior beneath the Alaska Peninsula along Alaska-Aleutian subduction zone. Geophysical Research Letters, 45(8), 3453–3460. https://doi.org/10.1002/2017gl076761

Li, S., Wang, K., Wang, Y., Jiang, Y., & Dosso, S. E. (2018). Geodetically inferred locking state of the Cascadia megathrust based on a viscoelastic Earth model. Journal of Geophysical Research: Solid Earth, 123(9), 8056–8072. https://doi.org/10.1029/2018jb015620

Lin, J. T., Aslam, K. S., Thomas, A. M., & Melgar, D. (2020). Overlapping regions of coseismic and transient slow slip on the Hawaiian décollement. Earth and Planetary Science Letters, 544, 116353. https://doi.org/10.1016/j.epsl.2020.116353

Loveless, J. P., & Meade, B. J. (2010). Geodetic imaging of plate motions, slip rates, and partitioning of deformation in Japan. Journal of Geophysical Research: Solid Earth, 115(B2). https://doi.org/10.1029/2008jb006248

Ma, S., & Nie, S. (2019). Dynamic wedge failure and along-arc variations of tsunamigenesis in the Japan Trench margin. Geophysical Research Letters, 46(15), 8782–8790. https://doi.org/10.1029/2019gl083148

Mai, P. M., & Beroza, G. C. (2002). A spatial random field model to characterize complexity in earthquake slip. Journal of Geophysical Research: Solid Earth, 107(B11), ESE-10. https://doi.org/10.1029/2001jb000588

McCaffrey, R., Qamar, A. I., King, R. W., Wells, R., Khazaradze, G., Williams, C. A., et al. (2007). Fault locking, block rotation and crustal deformation in the Pacific Northwest.

Geophysical Journal International, 169(3), 1315–1340. https://doi.org/10.1111/j.1365-246x.2007.03371.x

McCrory, P. A., Blair, J. L., Waldhauser, F., & Oppenheimer, D. H. (2012). Juan de Fuca slab geometry and its relation to Wadati-Benioff zone seismicity. Journal of Geophysical Research: Solid Earth, 117(B9). https://doi.org/10.1029/2012jb009407

McGuire, J. J., Smith, D. E., Frankel, A. D., Wirth, E. A., McBride, S. K., & de Groot, R. M. (2021). Expected warning times from the ShakeAlert earthquake early warning system for earthquakes in the Pacific Northwest (No. 2021-1026). US Geological Survey.

Melgar, D. (2020). dmelgarm/MudPy: v1.2 (version v1.2). Zenodo. https://doi.org/10.5281/zenodo.3703200

Melgar, D., & Bock, Y. (2015). Kinematic earthquake source inversion and tsunami runup prediction with regional geophysical data. Journal of Geophysical Research: Solid Earth, 120(5), 3324–3349. https://doi.org/10.1002/2014jb011832

Melgar, D., & Hayes, G. P. (2019). The correlation lengths and hypocentral positions of great earthquakes. Bulletin of the Seismological Society of America, 109(6), 2582–2593. https://doi.org/10.1785/0120190164

Melgar, D., LeVeque, R. J., Dreger, D. S., & Allen, R. M. (2016). Kinematic rupture scenarios and synthetic displacement data: An example application to the Cascadia subduction zone. Journal of Geophysical Research: Solid Earth, 121(9), 6658–6674. https://doi.org/10.1002/2016jb013314

Melgar, D., Williamson, A. L., & Salazar-Monroy, E. F. (2019). Differences between heterogenous and homogenous slip in regional tsunami hazards modelling. Geophysical Journal International, 219(1), 553–562.

Michel, S., Gualandi, A., & Avouac, J. P. (2019). Interseismic coupling and slow slip events on the Cascadia megathrust. Pure and Applied Geophysics, 176(9), 3867–3891. https://doi.org/10.1007/s00024-018-1991-x

Moreno, M., Melnick, D., Rosenau, M., Bolte, J., Klotz, J., Echtler, H., et al. (2011). Heterogeneous plate locking in the South–Central Chile subduction zone: Building up the next great earthquake. Earth and Planetary Science Letters, 305(3–4), 413–424. https://doi.org/10.1016/j.epsl.2011.03.025

Moreno, M., Rosenau, M., & Oncken, O. (2010). 2010 Maule earthquake slip correlates with pre-seismic locking of Andean subduction zone. Nature, 467(7312), 198–202. https://doi.org/10.1038/nature09349

Okada, Y. (1985). Surface deformation due to shear and tensile faults in a half-space. Bulletin of the Seismological Society of America, 75(4), 1135–1154.

Ozawa, S., Nishimura, T., Suito, H., Kobayashi, T., Tobita, M., & Imakiire, T. (2011). Coseismic and postseismic slip of the 2011 magnitude-9 Tohoku-Oki earthquake. Nature, 475(7356), 373–376. https://doi.org/10.1038/nature10227

Ramos, M. D., & Huang, Y. (2019). How the transition region along the Cascadia megathrust influences coseismic behavior: Insights from 2-D dynamic rupture simulations. Geophysical Research Letters, 46(4), 1973–1983. https://doi.org/10.1029/2018gl080812

Rong, Y., Jackson, D. D., Magistrale, H., & Goldfinger, C. (2014). Magnitude limits of subduction zone earthquakes. Bulletin of the Seismological Society of America, 104(5), 2359–2377. https://doi.org/10.1785/0120130287

Ruhl, C. J., Melgar, D., Grapenthin, R., & Allen, R. M. (2017). The value of real-time GNSS to earthquake early warning. Geophysical Research Letters, 44(16), 8311–8319. https://doi.org/10.1002/2017gl074502

Ruiz, J. A., Fuentes, M., Riquelme, S., Campos, J., & Cisternas, A. (2016). Numerical simulation of tsunami runup in northern Chile based on nonuniform k−2 slip distributions. Natural Hazards, 79(2), 1177–1198.

Schmalzle, G. M., McCaffrey, R., & Creager, K. C. (2014). Central Cascadia subduction zone creep. Geochemistry, Geophysics, Geosystems, 15(4), 1515–1532. https://doi.org/10.1002/2013gc005172

Spiess, F. N., Chadwell, C. D., Hildebrand, J. A., Young, L. E., Purcell, Jr., G. H., & Dragert, H. (1998). Precise GPS/Acoustic positioning of seafloor reference points for tectonic studies. Physics of the Earth and Planetary Interiors, 108(2), 101–112. https://doi.org/10.1016/ s0031-9201(98)00089-2

Tozer, B., Sandwell, D. T., Smith, W. H. F., Olson, C., Beale, J. R., & Wessel, P. (2019). Global bathymetry and topography at 15 arc sec: SRTM15+. Earth and Space Science, 6(10), 1847–1864. https://doi.org/10.1029/2019ea000658

Wang, K., Wells, R., Mazzotti, S., Hyndman, R. D., & Sagiya, T. (2003). A revised dislocation model of interseismic deformation of the Cascadia subduction zone. Journal of Geophysical Research: Solid Earth, 108(B1). https://doi.org/10.1029/2001jb001227

Wang, P. L., Engelhart, S. E., Wang, K., Hawkes, A. D., Horton, B. P., Nelson, A. R., & Witter, R. C. (2013). Heterogeneous rupture in the great Cascadia earthquake of 1700 inferred from coastal subsidence estimates. Journal of Geophysical Research: Solid Earth, 118(5), 2460–2473. https://doi.org/10.1002/jgrb.50101

Watanabe, S. I., Bock, Y., Melgar, D., & Tadokoro, K. (2018). Tsunami scenarios based on interseismic models along the Nankai trough, Japan, from seafloor and onshore geodesy. Journal of Geophysical Research: Solid Earth, 123(3), 2448–2461. https://doi.org/10.1002/2017jb014799

Williamson, A., Melgar, D., & Rim, D. (2019). The effect of earthquake kinematics on tsunami propagation. Journal of Geophysical Research: Solid Earth, 124(11), 11639–11650. https://doi.org/10.1029/2019jb017522

Williamson, A. L., Melgar, D., Crowell, B. W., Arcas, D., Melbourne, T. I., Wei, Y., & Kwong, K. (2020). Toward near-field tsunami forecasting along the Cascadia subduction zone using rapid GNSS source models. Journal of Geophysical Research: Solid Earth, 125(8), e2020JB019636.

Wirth, E. A., & Frankel, A. D. (2019). Impact of down-dip rupture limit and high-stress drop subevents on coseismic land-level change during Cascadia megathrust earthquakes. Bulletin of the Seismological Society of America, 109(6), 2187–2197. https://doi.org/10.1785/0120190043

Wirth, E. A., Frankel, A. D., Marafi, N., Vidale, J. E., & Stephenson, W. J. (2018). Broadband synthetic seismograms for magnitude 9 earthquakes on the Cascadia megathrust based on 3D simulations and stochastic synthetics, Part 2: Rupture parameters and variability. Bulletin of the Seismological Society of America, 108(5A), 2370–2388. https://doi.org/10.1785/0120180029

Yokota, Y., Ishikawa, T., Watanabe, S. I., Tashiro, T., & Asada, A. (2016). Seafloor geodetic constraints on interplate coupling of the Nankai Trough megathrust zone. Nature, 534(7607), 374–377. https://doi.org/10.1038/nature17632

CHAPTER 3

Can Stochastic Slip Rupture Modeling Produce Realistic M9+ Events?

From Small, D. T., & Melgar, D. (2023). Can stochastic slip rupture modeling produce realistic M9+ events?. *Journal of Geophysical Research: Solid Earth*, *128*(3), e2022JB025716.

3.1 Introduction

Unlike other rupture modeling techniques, stochastic slip modeling utilizes a reduced-physics approximation. Rather than solving for a fully dynamic rupture that includes fault zone characteristics like stress drop, material properties, and friction, it assumes that ruptures can be more simply described by only a few different statistical parameters inferred from observations of real earthquakes (Mai & Beroza, 2002). In this view, slip distributions are realizations of an underlying probability density function. The computational cost of determining ruptures for large magnitude events is reduced significantly, allowing for a greater quantity of unique events to be calculated in a short amount of time with modest resources. Studies that have shown to greatly benefit from use of stochastic models include earthquake early warning, where ruptures produced can be used to test existing algorithms (e.g., Ruhl et al., 2017), train advanced machine learning algorithms (e.g., Lin et al., 2021), as well as to seismic and tsunami hazard assessments where ruptures inform localized hazards (e.g., Graves et al., 2011; LeVeque et al., 2016; Small & Melgar, 2021).

In this work, we focus on the technique first introduced by Mai and Beroza (2002) where they determined that the best fitting autocorrelation function (ACF) that describes the stochastic nature of slip is the von Karman ACF (VK ACF). The approach has also been used by Lavallée & Archuleta, 2003, however, their procedures differ slightly on how they compute the power spectrums. This is not the only way to carry out stochastic rupture modeling. Herrero and Bernard (1994) first proposed the “k-square” spectral decay approach to generating synthetic finite fault models which assumes a fractal representation of slip. The k-square method has been

used and modified throughout the years (e.g., Davies et al., 2015; Ruiz et al., 2007). The k-square and the VK ACF method differ predominantly on their assumptions of the necessary length scales across which slip correlates. The k-square method only requires a single characteristic source dimension, whereas the VK ACF additionally uses correlation lengths to describe the dominant slip asperities following the findings from Somerville et al. (1999). Some of these stochastic methods have been validated in some manner based on past ruptures and their ensuant tsunamis, however, the von Karman ACF method has not been tested for its applicability and ability in producing great earthquakes.

Indeed, as new earthquakes occur, there have been numerous efforts to validate the different scaling laws and statistical parameters underpinning these approaches (e.g., Goda et al., 2016; Melgar & Hayes, 2019). Previous studies that have attempted to validate the stochastic method have done so by comparing against the tsunami that results from actual ruptures, rather than by a comparison to the slip patterns themselves. For instance, Geist et al. (2007) tested the stochastic slip approach's ability to reproduce run-up observations consistent with the 2004 M9.2 Sumatra earthquake. In a similar approach, Davies et al. (2015) tested nine variations of a k-square approach to generating synthetic finite fault models and evaluated them by comparing the tsunami they produced to that obtained from slip inversions. Of these nine variations, the favored method was then used by Davies (2019) to test the stochastic tsunamis generated at DART buoy locations from 17 M > 7.8 global ruptures. Goda et al. (2015) and Mori et al. (2017) tested the sensitivity and variability of inundation from stochastic models. These were generated using a known slip inversion as a reference or “background” model. They also tested ruptures produced without knowledge of the slip model. Mori et al. (2017) determined that tsunami inundation was strongly influenced by the source model applied when calculating the synthetic ruptures.

Other previous works have been focused on testing the uncertainties and sensitivities of utilizing stochastic slip ruptures for probabilistic tsunami hazard assessment (PTHA, e.g., Murphy et al., 2016; Sepúlveda et al., 2019; Scala et al., 2020). Murphy et al. (2016) uses a modified stochastic slip approach that incorporates systematic ruptures features observed in dynamic models focused on the 2011 M9 Tohoku event. With these modified models, they calculate the probability of wave height exceedance along the Japan coast and compare these statistics with the observed wave heights from the actual tsunami.

Additionally, there have been proposals to incorporate more detailed geophysical knowledge while maintaining computational efficiency into stochastic slip models. Small and Melgar (2021) proposed a way to utilize interseismic coupling to inform slip distribution. In this method, the goal is to use a fault zone's coupling pattern as the "background" model to pre-condition stochastic slip distributions, so that the resultant hypothetical ruptures correlate to it and the calculated ruptures are potentially more representative of the specific region's earthquake potential. In this work we leverage that approach. For many recent large ruptures where coupling models existed prior to the event, a modest correlation between large coseismic slip patches and regions of high coupling ratio has been noted. This correlation is seen in Chile (Barnhart et al., 2016; Metois et al., 2013), Peru (Perfettini et al., 2010; Villegas-Lanza et al., 2016), Alaska (Li & Freymueller, 2018), and Japan (Loveless & Meade, 2015). By including coupling in the modeling process, we posit that ruptures may have a greater likelihood of being more realistic. Yet, we acknowledge that this correlation does not necessarily equate to causation. The presence of a highly coupled zones may not directly indicate the location of large slip propagation, creating uncertainty in the slip pattern predictive nature of coupling. For instance, some previous earthquakes have ruptured only a portion of the highly coupled zone (e.g., Konca et al., 2008; Moreno et al., 2010; Perfettini et al., 2010). Similarly, our lack of instrumentation offshore in the shallow-most portion of the subduction zones creates great uncertainty in coupling models (e.g., Lindsey et al., 2021; Wang & Trehu, 2016). The question of the validity of the ruptures generated using a coupling model as a pre-condition is important to answer.

In this work, we explore two basic research questions. (a) Can the von Karman ACF approach to stochastic slip rupture modeling reproduce slip distributions that match great (M9+) earthquakes recorded in instrumental time? (b) If interseismic coupling is included as a priori constraint, does this better reproduce large ruptures? We use this study as a formal check for the application of stochastic slip modeling in calculating "realistic" large ruptures.

To answer these questions, we look at four different M9+ events: the 2011 Tohoku-Oki, Japan M9.0–9.1, 1960 Chile M9.2–9.4, 2004 Sumatra M9.1–9.3, and 1964 Alaska M9.2. We note that since reliable coupling models are not available for all four events, we only compare the influence of the coupling constraint for the 2011 Tohoku-Oki event. We compare modeled slip distributions to previously published finite fault slip inversions for each of the four ruptures. The assessment of slip distributions is done using a metric to determine the dissimilarity between

the slip patterns. We first focus on the 2011 Tohoku-Oki event and compare three different rupture classes to the slip model from Minson et al. (2014) (hereafter called the "Minson model"). Two of these rupture classes utilize the coupling constrained stochastic approach, each constrained by different end member coupling models from Loveless and Meade (2016). The other class of ruptures uses a homogeneous slip potential for the stochastic approach, which can be considered the more traditional approach (e.g., Frankel et al., 2018). We obtain unique dissimilarity values for each class. For a subset of these ruptures, we model tsunami inundation for the eastern coast of Japan between 35° and 41°N and compare the inundation results to a survey proceeding the 2011 tsunami by Mori et al. (2012).

After studying the Tohoku earthquake, we widen our focus to three other subduction zones and determine whether stochastic modeling has similar capabilities irrespective of rupture or region. In short, our findings will be that stochastic slip rupture modeling can reproduce "realistic" slip distributions for all M9+ ruptures. For the 2011 Tohoku-Oki earthquake, including the coupling constraint, has varying effects on the results: one coupling model noticeably improved the similarity to the Tohoku earthquake, and one was not able to produce any ruptures that were similar to the earthquake, indicating that in the absence of a well-constrained coupling model, assuming no coupling constraint is likely a safer choice.

We note that we use the term "realistic" in a rather confined sense. We are focused only on determining if the stochastic slip approach can create slip patterns that resemble real M9+ events. We do not test the "full stack" of a PTHA calculation, such as whether we can reliably reproduce yet to occur ruptures, their statistics, or rates of occurrence at a given subduction zone. These results are a basic, but fundamental, steppingstone for assessing the applicability of the stochastic slip methodology for use at other subduction zones and future great earthquakes.

In this sense, the findings of this work still leave uncertainty in the full distribution of potential synthetic ruptures produced by stochastic modeling. For strong certainty and confidence in stochastic slip rupture modeling when applied to hazards related studies, we not only need to know if the process has the potential to reproduce slip patterns seen in previous large earthquakes, but also if the general patterns produced in all other synthetic ruptures are representative of the global history of earthquakes. This latter question is very challenging and the subject of ongoing work. As a community, we do not yet understand global earthquake history and slip potentials as well as needed to answer that question. Instead, here we inch closer

to that full answer by assessing the ability of the stochastic slip approach for producing slip distributions similar to the subset of M9+ ruptures we have observed in instrumental times.

3.2 Data and Methods

3.2.1 Input Models

3.2.1.1 Slip Models

In this study, we will focus first on the 2011 M9 Tohoku-Oki event first since it is the best studied great earthquake (Lay, 2018); however, we will also make note of three other M9+ ruptures in Section 3.3. The ruptures calculated using the coupling constraint technique, along with ones generated without the constraint, will be compared to a slip distribution model for the 2011 M9 Tohoku-Oki rupture.

The Honshu Island region of Japan is the most densely instrumented area globally for geophysics-based observations. The dense instrumentation and the great societal impact of the rupture made this event of wide interest to the scientific community (see Lay, 2018 for a review)—well over 50 slip inversions have been calculated. Nine example slip inversions are shown in Figure 1. Rupture dimensions of slip models range from 475 to 600 km along strike and 200–275 km along dip. While there is some variability between these models, they all image a large slip asperity centered at 38°N. Some of the inversions were determined from teleseismic body and/or long period surface waves (Ide et al., 2011; Shao et al., 2011; Yagi & Fukahata, 2011), GPS and strong ground motions (Wei et al., 2012), tsunami data, or any combination of multiple techniques and datasets (Ammon et al., 2011; Minson et al., 2014; Wei et al., 2011; Yamazaki et al., 2011; Yue & Lay, 2013). Out of these nine models, only Yue and Lay (2013) and Minson et al. (2014) combined all listed data types. Of all previously determined models or the 2011 Tohoku-Oki earthquake, the Minson model is particularly compelling because it is a Bayesian non-linear inversion. Peak slip ranges from 45 to 75 m between models, and while there is still considerable uncertainty involving the “exact” nature of the coseismic slip distribution, most of these inversions share similar features like their dominant slip asperity shape and location, and their shallow high slip. For instance, the Minson model has a very similar slip pattern to Yue and Lay (2013), Wei et al. (2012), and Yagi and Fukahata (2011).

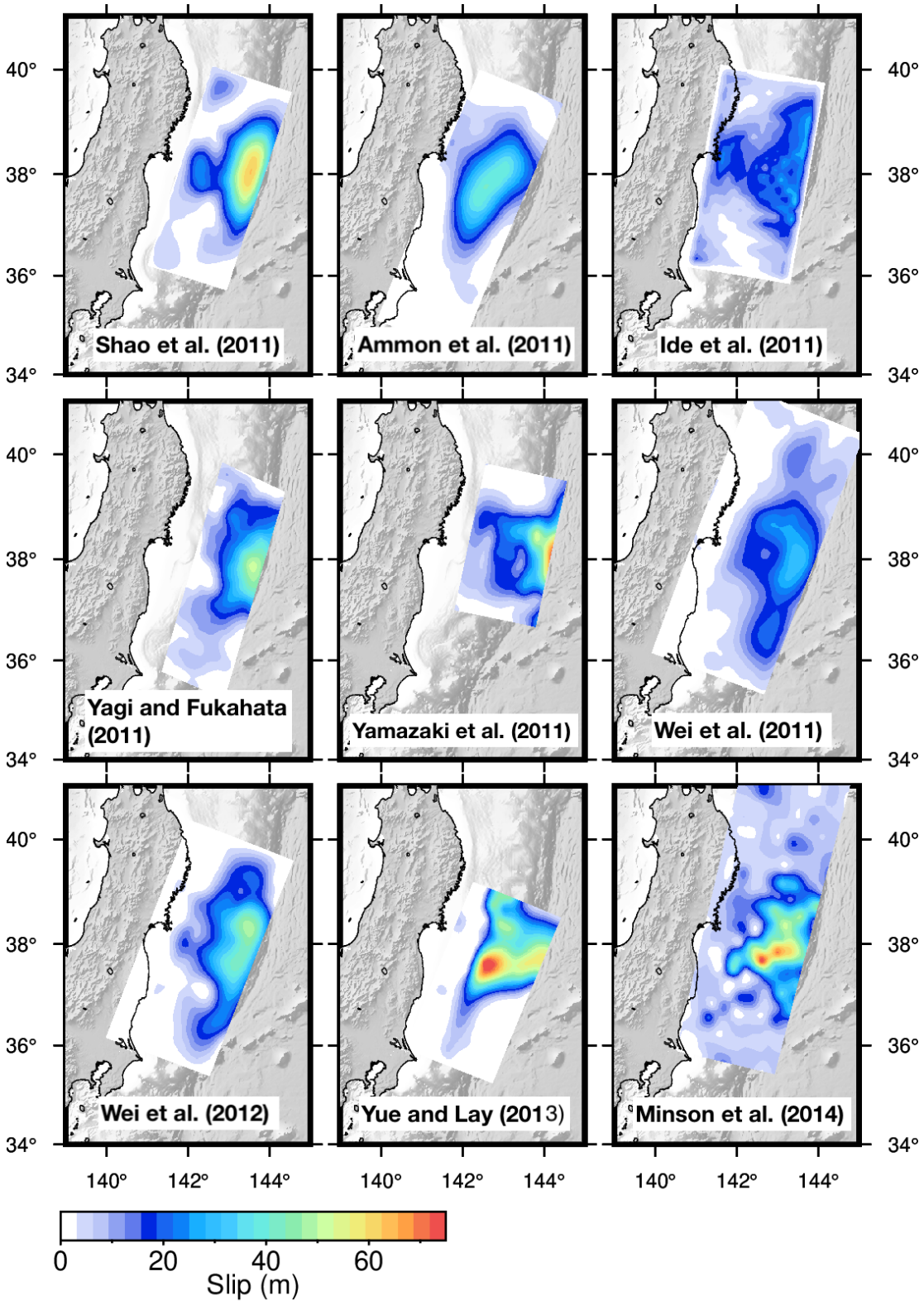

Figure 1. *Nine example finite fault slip inversions for the 2011 Tohoku-Oki earthquake.*

For our comparison between stochastic ruptures and aimed slip we focus on only one of the models for the earthquake from Minson et al. (2014) expressed in Figure 2a. This model concentrates most of the slip of the rupture between 10 and 20 km in depth, with the magnitude of slip reaching 75 m high within this region. As stated prior, the Minson model is a fully Bayesian inversion, determined from simultaneously inverting for 1 Hz kinematic high-rate GNSS data, static GNSS offsets, seafloor geodesy, and tsunami data. For these reasons, and because it still shares many similarities with other inversions, we consider it to be one of the best resolved slip distributions for the earthquake.

For the other global earthquakes, we similarly focus on one slip model for each event. We utilize the finite fault slip inversion from Ho et al. (2019) ("Ho model," Figure 2c) for the 1960 M9.2–9.4 Chile event. The inversion was determined by jointly inverting tsunami waveforms and local geodetic data obtained from post-event leveling surveys. The model indicates slip extending along-strike for over 800 and 150 km along-dip. Slip is concentrated in three large slip asperities, each with a width of about 200–300 km and magnitude of peak slip around 40 m.

For the 2004 M9.1–9.3 Sumatra, we implement the inversion from Rhie et al. (2007) ("Rhie model"). This model was calculated by jointly inverting long period teleseismic data and local geodetic surface displacements (Figure 2d). One large slip asperity (~40 m) occurs in the southern portion of the rupture zone; however, slip extends almost 1,300 km along the Nicobar-Andaman Island chain. The relative size of the asperity is quite small in relation to the rupture region where more dispersed small slip occurs. Several other slip models have been proposed for this rupture (e.g., Ammon et al., 2005; Bletery et al., 2016; Gopinathan et al., 2017; Ji, 2005), however, these models utilize either teleseismic data or geodetic and tsunami data only for their inversions. So, we focus here on only the Rhie model for comparison against the stochastic ruptures calculated.

Lastly, we use the inversion model determined by Ichinose et al. (2007) for the 1964 M9.2 Alaska earthquake. Suito and Freymueller (2009) also presented a model for this rupture, however, we focus on the Ichinose model as it is expressed with finer resolution. Both inversions depict very similar slip patterns so either model would suffice as the example. The Ichinose model was calculated using a least squares inversion of teleseismic P waves, tide gauge data, and geodetic leveling surveys. Here, a 680 km segment of the Aleutian megathrust is modeled with a peak slip of 14.9 m and a mean slip of 4.9 m across the domain (Figure 9b). There are three

dominant asperities along the Aleutian megathrust with peak slip values noticeably smaller than the three previous ruptures. In combination with the megathrust rupture, slip propagated along the Patton Bay splay fault (PBF) with a higher peak slip of 17.4 m (Ichinose et al., 2007). 10 m of uplift that was observed that was predominantly resulted from the PBF slip (Plafker, 1967). For this study we do not include the PBF in our synthetic slip models.

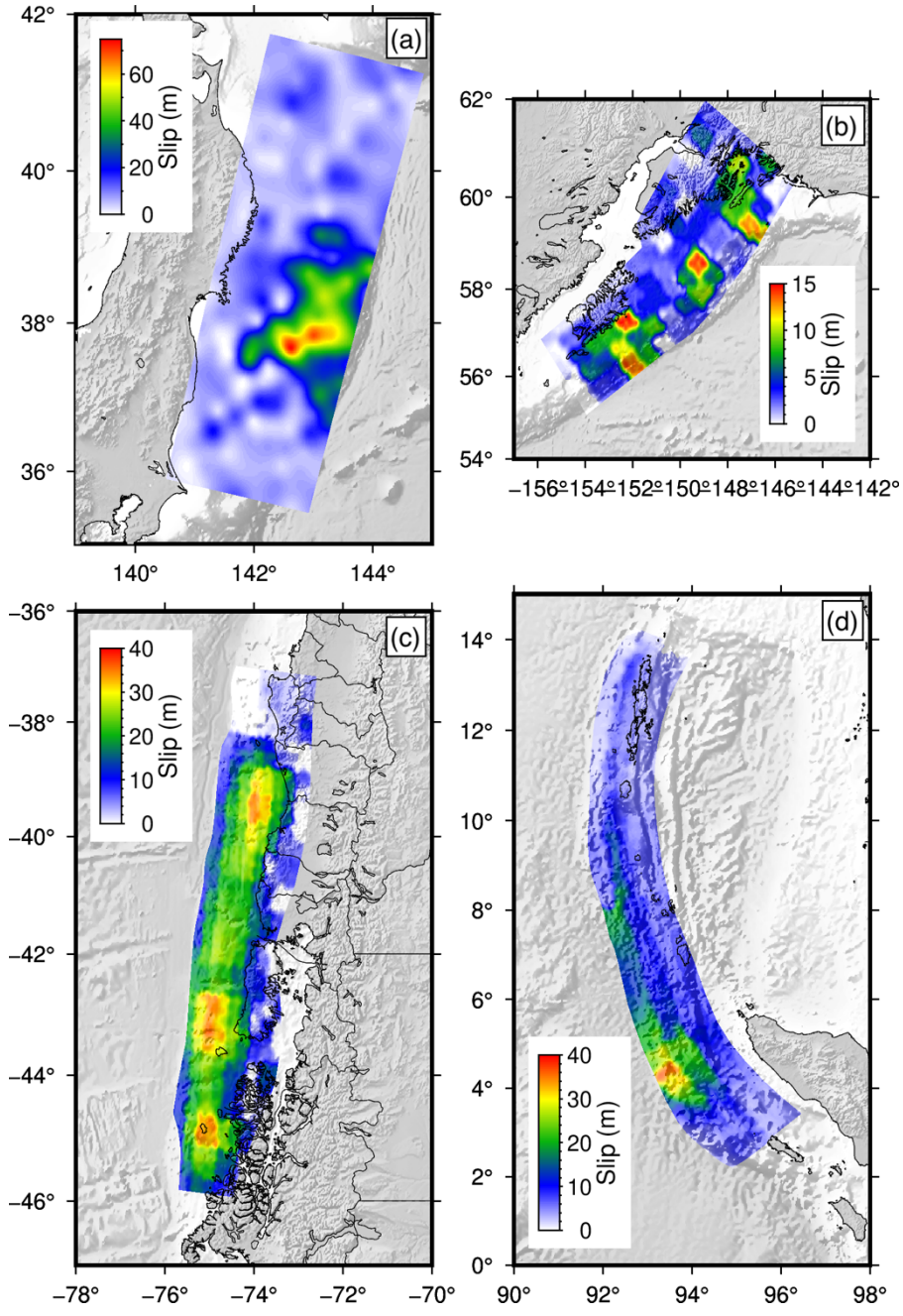

Figure 2. *Finite fault slip models used in this study. (a) 2011 M9.1 Tohoku rupture model from Minson et al. (2014). (b) 1964 M9.2 Alaska rupture model from Ichinose et al. (2007). (c) 1960 M9.2–9.4 Chile rupture model from Ho et al. (2019). (d) 2004 M9.1–9.3 Sumatra rupture model from Rhie et al. (2007).*

3.2.1.2 Interseismic Coupling Models

Where interseismic coupling models are available, we want to utilize these as the background slip models in the coupling constrained stochastic approach presented in Section 2.2. However, since reliable GNSS data prior to the rupture is only available at the Japan Trench, we only include coupling models for this region in our Tohoku example. The other three global ruptures presented in this study do not include the coupling constraint.

We look at two different slip deficit rate (SDR) models for the Japan Trench from Loveless and Meade (2016) (Figure 3). These models will be used as "background" models implemented in the stochastic method to constrain output slip patterns. Both models are constrained using roughly 19 years (1996–2014) of geodetic observations from the national geodetic network for Japan (GEONET). The time-series data is split into five, 3.75-year epochs and the SDR models are determined using the block model approach from Meade and Loveless (2009). The final SDR models are calculated by taking the average of the results of the five epochs. The models are determined using the same inputs as one another; however, they vary based on an imposed constraint of coupling (or no coupling) at the trench. Figure 3a imposes a constraint that the shallowest portion of the subduction zone creeps at an equal rate as the Pacific Plate rate. This model follows the idea that the shallowest portion of the megathrust cannot accumulate interseismic elastic strain. This is posited to be the result of the high percentage of clay composition at the trench (Oleskevich et al., 1999). On the other hand, the model in Figure 3b eases this constraint, permitting variable coupling to occur up to the trench. Due to the lack of instrumentation offshore, the shallowest portions of the megathrust are poorly resolved, evident by the wide variability in SDR between the two models predominantly in the shallowest depths. Without more robust offshore GNSS instrumentation, determining which model is more accurate is nearly impossible. Therefore, we utilize both models for the study.

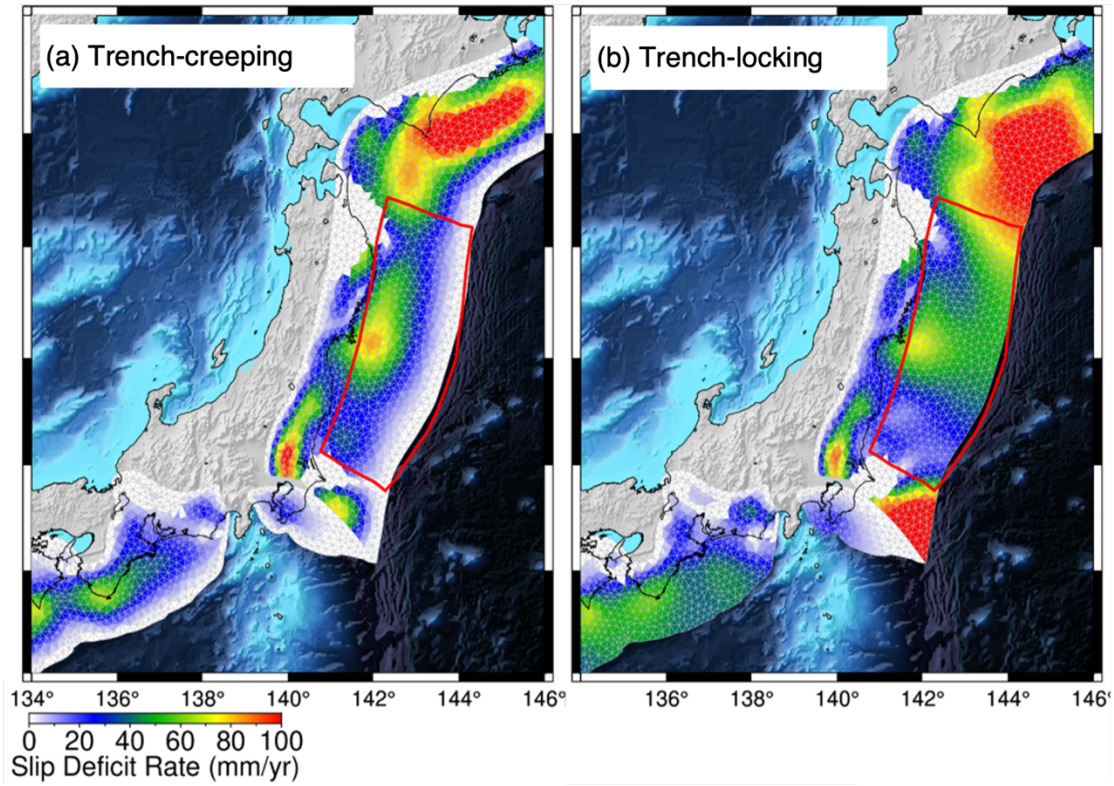

Figure 3. *Slip deficit rate (SDR) models for the Japan Trench region. (a) "Trench-creeping" SDR model with the imposed constraint of creeping (or SDR = 0 mm/yr) from 5 km downdip to the trench. (b) "Trench-locking" slip deficit rate (SDR) model where no constraint on coupling near the trench so slip deficit is present up to the trench. Both coupling models come from Loveless and Meade (2016). Red outline follows the Minson model that is used as the domain for the synthetic models.*

3.2.2 Stochastic Models

Here, we briefly detail the method of stochastic modeling, as well as how coupling patterns are introduced in the process to inform the resultant slip models. These methods can be found described in greater detail in LeVeque et al. (2016), Melgar et al. (2016), and Small and Melgar (2021). The process described below is for the Tohoku rupture case. The same process is used for the other global ruptures without the addition of the coupling constraint.

The first step is to define the megathrust as a 3D mesh surface composed of discrete subfaults using the three-dimensional finite element mesh generator, GMSH (Geuzaine & Remacle, 2009). The slab mesh is generated with the Slab2 model from Hayes et al. (2018) with an average subfault vertex length of 15 km. We constrain the 3D mesh to the domain of slip in the Minson

model rather than using the entirety of the Japan subduction zone. Recall, our focus here is only to test the ability of the stochastic approach to reproduce rupture patterns. Since we are only focused on creating ruptures with "realistic" slip patterns, we do not worry about utilizing a full subduction zone domain to model on. This same process is used for the Sumatra case, where the rupture domain is defined from Slab2. For the Chile case, we utilize the slab model from Rodriguez and Russo (2020) rather than the Slab2 since the latter does not reach the entirety of our rupture domain. For the Alaska case, however, we maintain a simple rectangular domain that follows the Ichinose model. Rather than modeling in 3D, we maintain a simple geometry because interpolating from the original fault geometry from Gudmundsson and Sambridge (1998) to Slab2.0 would create too many irregularities and potentially alter the magnitude of the interpolated model.

Once the mesh is defined, a subfault is selected at random as the synthetic rupture hypocenter. For a given target magnitude, the rupture length and width are determined based on a probabilistic scaling law (Blaser et al., 2010), which for any earthquake magnitude led to a log-normal distribution of length and width. As the rupture magnitude increases, the dimensions of the rupture also on average increase. The log-normal distribution allows for variability within the dimensions of ruptures of equal magnitude.

Then, we utilize the method of stochastic modeling introduced by Mai and Beroza (2002) to calculate the rupture itself. Mai and Beroza (2002) determined that the autocorrelation function that best represents slip as a spatially random field is the von Karman autocorrelation function (VK ACF),

$$P(k) = \frac{a_x a_z}{(1+k^2)^{H+1}},$$

where the a denotes the correlation lengths along-strike and downdip, H is the Hurst exponent, and k is the wavenumber. The correlation lengths principally describe the dominant asperity size of the ruptures. As the magnitude and dimensions of a rupture increases, the correlation lengths also increase. With the VK ACF, there are only three necessary assumptions needed to define earthquake slip patterns: the correlation lengths in the along-strike and down-dip, and the Hurst exponent that models the roughness of the slip pattern. We apply the results from Melgar and Hayes (2019) for defining correlation lengths based on a log-linear scaling of magnitude and correlation lengths and a magnitude independent Hurst exponent.

The method above is expressed in the spectral domain of slip rather than the spatial domain. To account for 3D fault geometries and enforce prior constraints (e.g., geodetic coupling), we apply the Karhunen-Loeve (K-L) expansion to the VK-ACF, where slip can now be represented spatially (LeVeque et al., 2016). The K-L expansion states that a slip vector, s, is described as

$$s^g = \mu^g + \sum_{k=1}^{N} z_k \sqrt{\lambda_k^g \nu_k^g}.$$

This defines *s* as the sum of the background slip model, μ, and the summation over the desired number of eigenmodes, N, of the eigenvalues and eigenvectors from the VK-ACF, λ_k and ν_k. Further stochastic behavior of the resultant ruptures is included in the equation thanks to z_k, which defines a normally distributed set of random numbers with a mean of 0 and a standard deviation of 1. The variable z allows us to create any number of unique slip distributions for a given magnitude and rupture dimensions. A difficulty that arises in using the K-L expansion is the possibility of producing negative slip values. Negative slip would produce normal faulting behavior, inconsistent to the desired sense of faulting. This is not observed in nature, so, to remedy it LeVeque et al. (2016) used a lognormal distribution that inherently restricts slip values to be strictly positive. In Equation 2, the superscript g denotes a lognormal distribution.

For ruptures where all subfaults have equal potential for slip and no prior constraints are applied, μ is simply a homogeneous mean model with enough slip to match the desired target magnitude. However, we can instead impose a mean slip model that is informed by the coupling pattern as μ. For instance, for a given desired magnitude and rupture dimensions are selected from the scaling laws, the coupling pattern in the segment is re-scaled into slip pattern. This is then used as μ and stochastic variability is applied to create the output ruptures.

In this method, the coupling model does not inform how much slip will occur at a given location. But rather, it provides a greater probability for areas of high SDR to have greater coseismic slip. It is still possible in this method for a region of high SDR to rupture in smaller slip than a region with relatively smaller SDR. In this method however, regions where SDR = 0 should not produce coseismic slip. The actual influence of the coupling constraint is often difficult to discern for a single given rupture, but in observation with a large suite of ruptures, the mean pattern of slip for all the ruptures in the suite resembles the initial coupling pattern constraint.

To calculate the ruptures, we use the Fakequakes implementation of the aforementioned methods. This is a module of the open-source forward modeling and inversion code MudPy (Melgar & Bock, 2015; Melgar, LeVeque et al., 2016; Small & Melgar, 2021). Fakequakes can calculate both homogeneous and coupling constrained synthetic rupture models. For each of the three classes mentioned prior, we calculated a total of 4,000 ruptures with starting magnitudes between M8.8 and M9.1 in magnitude bins of 0.1. The maximum slip on any given subfault is limited to 100 m. Although this is quite large, the 2011 Tohoku-Oki event is considered to have slipped over 70 m in some patches (Minson et al., 2014). The rupture domain lies between 35°N and 41°N, with a down dip limit of slip at 50 km depth. The domain follows the slip region of the Minson model (Figure 2a). Rupture area and magnitude are unconstrained, so any portion of the domain may be considered or neglected, and the final magnitude for a given area may vary from the starting magnitude based on dimensions and scaling laws. We also leave the hypocenter location unconstrained, meaning the code selects at random any subfault to nucleate the rupture. For the coupling constrained stochastic models, regions where the SDR is 0 cannot slip nor act as the hypocenter. A Hurst exponent of 0.75 is used along with all eigenmodes (equal to the number of subfaults) in our models. Typically for tsunami modeling purposes, a smaller amount of eigenmodes can be used to reasonably represent a rupture (LeVeque et al., 2016); however, here we use all eigenmodes in order to reduce possibilities of uncertainty.

Similar Fakequakes setup for homogeneous mean model ruptures is implemented for the other M9+ earthquakes. For each of the global ruptures, we model 2,500 ruptures in 0.1 magnitude bins. Since we do not include the coupling constraint for the global ruptures, ruptures are only calculated with the homogeneous background model. Like the Tohoku case, rupture area and magnitude are unconstrained and a downdip limit of 50 km depth is applied. More information on the setup for the other events is described in Section 3.3.

3.2.3 The Dissimilarity Metric

Since we are interested in comparing the generated stochastic slip distributions to known slip inversions, it is important to define a quantitative assessment of likeness between models. To do this, we calculate the numerical dissimilarity between ruptures using the normalized square metric (Kragh & Christie, 2002; Razafindrakoto et al., 2015). There are other metrics for

quantifying dissimilarity (e.g., gray scale metric, Wilson et al., 1997), however, we focus on the normalized square metric as it is both numerically simple and efficient.

In comparison to other dissimilarity metrics, the normalized square metric is best for capturing the magnitude differences between two objects and is sensitive to image translation. The normalized square mean metric expresses dissimilarity, D, as

$$D(A,B) = 100\frac{\sum_i[A(i)-B(i)]^2}{(\sum_i[A(i)]^2-\sum_i[B(i)]^2)/2}.$$

Dissimilarity between two slip models, A and B, is expressed as the sum of square of the difference between the models individual subfaults divided by the mean of the individual squared values. A and B in the equation are regular grids of subfaults. Prior to interpolating to a regular grid, we first interpolated the Minson model to the Slab2 geometry to maintain uniformity in the process. We then interpolate the 3D triangular mesh ruptures and slip model using the spline interpolation method.

Kragh and Christie (2002) previously define this metric as a percentage with values between 0% and 200%. The more dissimilar the two models are from one another, the greater the value. D = 0 denotes identical slip models and the greater the differences between the two models, the greater the value of D is. For ease of understanding, we scale the dissimilarity metric by dividing it by two, making it a metric from 0 to 100.

3.2.4 Tsunami Inundation Modeling

Although the dissimilarity value provides a basis for quantifying likeness between the slip models, only analyzing the one metric may still produce uncertainty in determining whether a rupture is realistic when compared to the earthquake model of focus. While low dissimilarity between a stochastic model and the inversion is encouraging, there is no clear distinction on what values of dissimilarity qualify as “good enough” for considering one of the hypothetical ruptures comparable to the specific slip inversion. To determine the dissimilarity values that can be considered, for example, “Tohoku-like,” we take the extra step of modeling tsunami inundation and compare inundation values to recorded survey points. Specifically, we compare how well our synthetic ruptures can match the post-event survey points from Mori et al. (2012) based on the percentage of points inundated and their inundation heights. This analysis provides an observable phenomenological rationale for comparing impacts of ruptures since the rupture pattern directly controls the extent of the tsunami. We note here that only inundation modeling in this study is

done so for the Tohoku example. The other three rupture cases do not have as extensive inundation surveying following the tsunamis as did the Tohoku event. Though we cannot directly compare the phenomenological observations for the other global ruptures, we cautiously utilize the results from the Tohoku case in the global rupture analyses.

Post-event tsunami inundation surveys measure the maximum height of the tsunami wave propagation onshore. Here, we define inundation with respect to mean sea level. We model inundation at 3,244 survey points from Mori et al. (2012) (Figure 4). In the study, they record over 5,000 total tsunami data points onshore between 35° and 41°N. In their data set, they also record run-up height, which is the maximum height the tsunami propagated to onshore (the run-up distance) with respect to sea level. We do not consider these points for our study since modeling for run-up distance and height is difficult. The data set for inundation is extensive along the coast, however, a gap in data between roughly 37–38°N is present. Data distribution is not recorded equally along the coast, with the greatest abundance of points in the Sendai Bay and Sanriku Coast in Iwate Prefecture (37.5–38.4°N). The inundation points range from 0 to 40 m in height, with over 75% of all inundation points below 10 m. Some inundation points are also recorded as far as 5 km inland, but the majority of the points occur less than 1 km from the shore.

To model tsunami inundation for calculated ruptures, we first must determine the resultant coseismic vertical deformation to be applied as the initial condition for tsunami wave generation. We utilize the analytical solution for angular dislocation for triangular subfaults in an elastic half space (Comninou & Dundurs, 1975), which is an adaptation of the Okada equations for rectangular subfaults (Okada, 1985). We use the radially symmetric Earth structure model from Gregor et al. (2002) developed for the Cascadia subduction zone for calculating the surface deformations. Tsunami inundation is calculated using the finite volume, 2D depth-average, non-linear tsunami modeling code Geoclaw (http://www.clawpack.org/geoclaw) (LeVeque et al., 2011). We assume an instantaneous starting condition since rupture propagation velocities are much faster than tsunami wave velocities (e.g., Williamson et al., 2019).

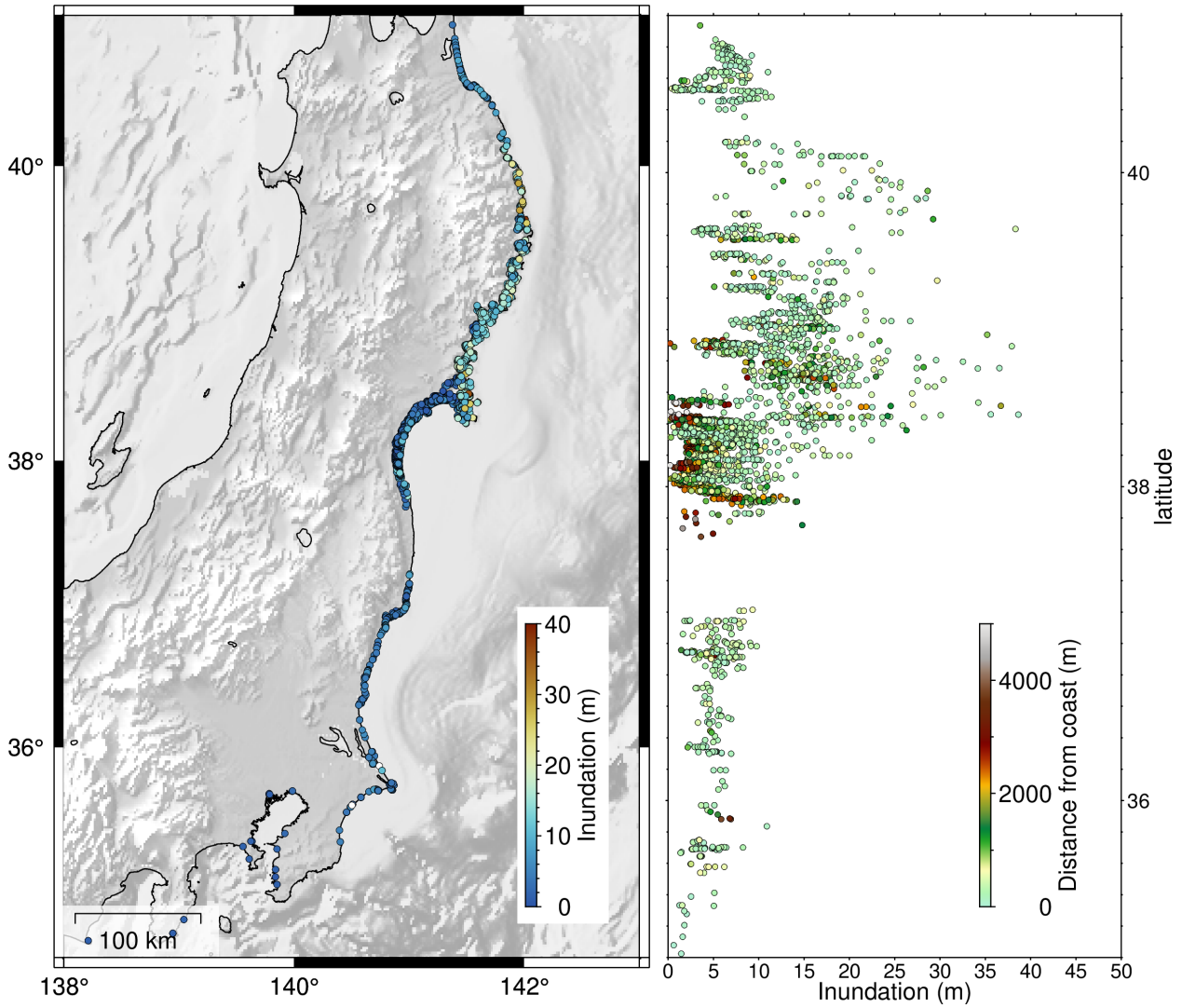

Figure 4. *Tsunami inundation survey of the 2011 Tohoku-Oki tsunami from Mori et al. (2011). (a) Map view depiction of survey points where color scale depicts recorded inundation height in meters. (b) Plot of tsunami inundation versus latitude with the color scale depicting the distance the survey point is from the coast. Most recorded points are less than 100 m from the coast, but in the Sendai Plain (~38°N) points are recorded several kilometers from the coast.*

We model tsunami generation and inundation for points between 34.5° and 41°N. Topography and shallow water bathymetry must be sampled with very fine resolution for accurate inundation modeling. Because our modeled domain is quite extensive (7° in latitude and longitude) and we need fine resolution bathymetry and topography data for coastal regions, we utilize one coarser bathymetry/topography file for the entire domain and finer scale subregions

for the coastal areas of interest to decrease computational cost. We use SRTM15 with a sampling rate of 15 arcseconds (~450 m pixels) for our overall bathymetry/topography domain (Tozer et al., 2019). We then stitch together SRTM1 topographic data (1 arcsecond sampling rate, ~30 m pixels) and 1 arcsecond bathymetry data from the "M7000" data set purchased from the Japan Hydrographic Association in eight rectangular segments that extend to 200 m below sea level between 34.5°N and 41°N. We resample these fine segments from 1 to 3 arcseconds as 1 arcsecond was too costly for the tsunami models to run even with 40 CPUs in hand. To increase efficiency even more, we utilize the adaptive mesh refinement (AMR) within GeoClaw where the more complex portions of tsunami propagation occur and proximity to regions of interest decrease, the mesh can adaptively become finer. We use five different AMR levels that go from coarsest to finest: 2', 1', 30", 15", and 3", respectively.

Even with these capabilities, modeling inundation for over 3,000 points along a region of 7° latitude is costly. Using 25 threads, each tsunami inundation model took over 4 hr to complete. So, rather than calculating all 12,000 tsunami models, we instead took a subset of ruptures, totaling 330. These ruptures were chosen at random, however, we favored adding more ruptures with lower dissimilarities (below D = 50). Since our main interest is determining the efficacy of the von Karman ACF stochastic approach at producing great earthquakes, our focus is naturally on the lowest valued dissimilarities. From Equation 3, the more similar the stochastic model is to the slip inversion, the lower the dissimilarity value is. So, lower dissimilarity ruptures become increasingly more important than larger valued ones. For each of the runs, we compare the inundation residual between the modeled points and the surveyed points using the root mean squared error (RMSE), and we also look at the percentage of points inundated, regardless of inundation height. We utilize the RMSE rather than another statistical metric as it allows us to directly observe error in the same dimensions as our data. The inundation percentage on the other hand, allows us to observe a simpler binary statistical measure.

3.3 Results

3.3.1 Rupture Modeling and Dissimilarity for the Tohoku-Oki Case

In total, 12,000 ruptures were generated and split evenly between the three different rupture classes. Although initial magnitudes range from M8.8 to 9.1, final magnitudes fall between M8.6 and 9.4 since we modeled ruptures without magnitude constraint. All three ruptures classes have

similar distributions of final magnitudes. Rupture dimensions vary across the fault zone, however, due to the more confined model domain where ruptures may propagate over, there is a tendency for ruptures to slip the entire domain.

For all ruptures, we calculate the dissimilarity between the slip distribution and the Minson model using the normalized squared metric. The values for all ruptures are shown in Figures 5a–5c, where they are plotted in histograms based on rupture class. From the histograms, we can split the three classes into two distinct groups based on their distributions of dissimilarity values. The trench-creeping class produces ruptures with higher values than the other two classes, with a minimum value of 35. The distribution has a mode around a dissimilarity of 60. The trench-locking and homogeneous classes, on the other hand, have a dissimilarity distribution relatively like one another. The minimum dissimilarity for the two classes is 12 for the trench-locking and 16 for the homogeneous class. To first order, the two classes appear to have similar rupture dissimilarity distributions, yet there is a tendency in the trench-locking ruptures toward lower values overall. In comparison to the trench-creeping class, the homogeneous class has almost 400 ruptures below the least dissimilar trench-creeping rupture, about 10% of the total homogeneous ruptures. The trench-locking class, however, has almost 600 ruptures below the trench-creeping class, or 15%.

From these dissimilarity values, we would like to better understand at what dissimilarity value can a rupture most likely be considered "Tohoku-like." The accompanying rupture models in Figure 5 show three ruptures for each class with varying rupture dissimilarities. We generally see noticeable differences between ruptures with the lowest dissimilarities (Figures 5g–5j) and the highest dissimilarity (Figures 5f–5l). Besides the lowest dissimilarity ruptures, it is difficult to confidently distinguish just by observation which rupture has the lower dissimilarity in the second two columns.

There is a trend for ruptures below a value of 35 to have large slip patches around 38°N and between 10 and 30 km downdip similar to the Minson model. Because the normalized square metric assesses dissimilarity by a point-by-point comparison, even if a rupture has a similar asperity size and shape to the Minson model, if the location of the patch is offset, this will influence the dissimilarity outcome. This metric is also more heavily affected by larger slip differences. So, if larger slip patches are not represented or expressed in other areas than the location of the Minson large slip patch, this negatively influences the outcome dissimilarity. As

the rupture dissimilarities increase, the variability in the patterns of slip distribution increases. For instance, some ruptures with larger dissimilarities do not rupture up-dip and some experience their largest slip patches farther North or South of the Tohoku slip patch in disagreement to the Tohoku earthquake.

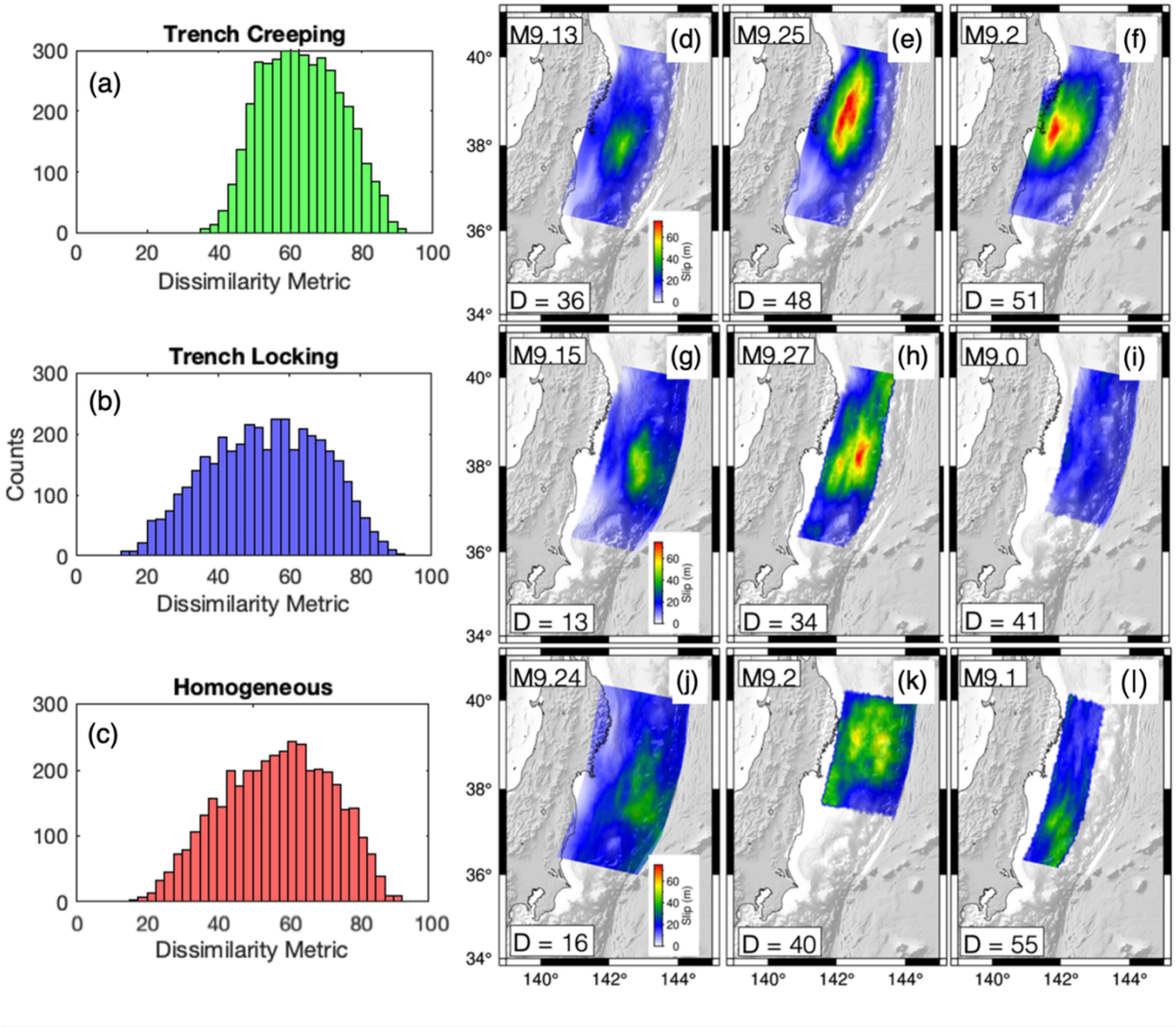

Figure 5. *Dissimilarity results for each of the three rupture classes. (a–c) Dissimilarity metric histograms with a bin width of 2.5 for the three rupture classes. (d–f) Example stochastic rupture slip models with varying dissimilarity values, D, for the trench-locking class, with lowest values toward the left. Rupture magnitudes are presented in the top left corner of each map. (g–i) Same as above but for the trench-locking class. (j–l) Same as above but for the homogeneous class.*

3.3.2 Tsunami Inundation Results for the Tohoku-Oki Case

Dissimilarity alone is a useful metric to determine a rupture's likeness to the slip model; however, there is some ambiguity by using the metric alone. Thus, we include inundation modeling as an extra dimension of likeness. By observing both inundation and dissimilarity, we can have a better sense of the finer differences between ruptures of variable dissimilarities.

Along with modeling tsunami propagation for the 330 synthetic ruptures, we model tsunami inundation as a result of the Minson inversion to establish a comparison baseline. All applied conditions for tsunami propagation are the same for the Minson scenario in comparison to the stochastic models. The Minson slip model can inundate 91% of all inundation points and fits with an RMSE of 7.1 m. The synthetic ruptures, on the other hand, have a spread of RMSE values between 7 and 10.5 m, and a large range of inundation percentages between 10% and 100%. The inundation from the Minson scenario is very well modeled, however, still with error. The Minson model has the most difficulty in accurately inundating points along the Sanriku coast where survey points record the largest wave heights. Still, it is able to inundate most points with a relatively small RMSE compared to the suite of synthetic ruptures.

Figure 6 shows two example stochastic ruptures with differing dissimilarity values and their tsunami inundation. The first example is a rupture with a low dissimilarity value of 12.3. In comparison to the post-event survey, the model inundated 92% of the 3,244 survey points. The RMSE of the inundation model is 7.03 m with respect to the survey. The modeled tsunami residuals for this rupture are biased toward the positive which represents a larger tsunami than the recorded tsunami. By considering both the very low dissimilarity value and the high percentage of points inundated from this rupture, we can say this rupture is “Tohoku-like.” In contrast, the second rupture shown has a dissimilarity much greater than the first, with $D = 50.65$. From inspection of the slip distribution, we can see that it does not contain a large shallow slip patch as required by the Minson slip inversion. This rupture rather experiences the largest slip toward the North of the domain. Its tsunami model only inundates 56% of the survey points, far less than the 92% inundation from the previous rupture. This rupture does not appear to inundate far inland from the coast—almost all survey points past 1 km do not experience inundation. We can see from this example that this rupture should not be considered “Tohoku-like” based on its high dissimilarity and fits the inundation data poorly.

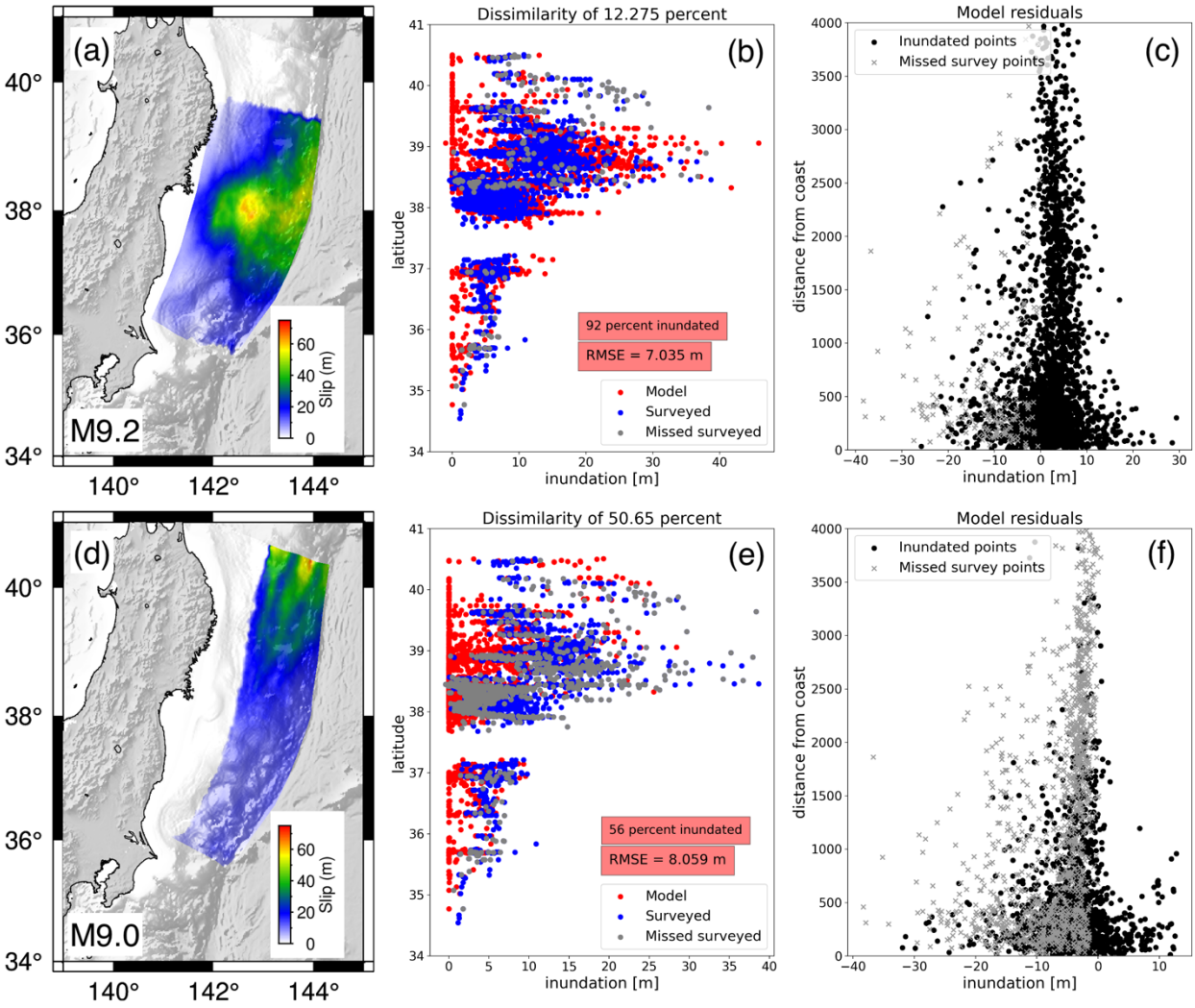

Figure 6. *Example ruptures with their resultant tsunami inundation results. (a) M9.2 rupture model in the trench-locking class. (b) Inundation in meters at each of the survey point locations versus latitude. Points are color coded as red, blue, and gray for the modeled points from the rupture in (a), the recorded survey points, and the missed survey points that did not get inundated by the model, respectively. The dissimilarity value for the rupture is presented at the top of the plot. (c) Tsunami inundation residual in meters between the modeled points and the surveyed points versus the distance from the coast in meters at each point. Points are denoted by a gray X for missed surveyed points and so the residual is simply the inundation height from the survey. (d) M9.0 rupture model in the trench-locking class. © Same as (b) but for the rupture model in (d). (f) Same as (c) but for the rupture model in (d).*

If we consider all the ruptures that we performed inundation modeling for, we can understand the relative importance and "threshold" of the dissimilarity metric. In Figure 7, the dissimilarity metric is plotted with respect to the inundation percentage for all three of the rupture classes. Each scatter point is scaled by the rupture's RMSE for inundation. There is a clear distinction between ruptures with high and low dissimilarity values. The points generally follow a linear path along which the dissimilarity metric decreases, the inundation percentage increases and the RMSE decreases. So, as the ruptures approach the top left corner of the plot, the ruptures become more "Tohoku-like." There is some variability associated with these metrics, especially in the more moderate (30–60) dissimilarity values. For instance, for a given moderate dissimilarity value, inundation percentage varies by almost 40%–50%. As the dissimilarity percentage decreases, however, the degree of variability in all three metrics decreases.

To maximize the rupture's similarity to the Tohoku event and specifically the Minson model, we look for dissimilarity values that both maximize the inundation percentage and minimize the RMSE. From the results, we fit an arbitrary threshold for what can be considered a "Tohoku-like" rupture at D = 20. At this threshold, inundation percentage for all points is over 80% and there is the smallest variation in the distribution of inundation percentages. The RMSE for all ruptures is consistently under 8m, with an average RMSE of 7.34 m, which is over 1m smaller than the total average. Recall that the Minson model inundated 91% of the points and has an RMSE of 7.1 m. The synthetic ruptures that have a dissimilarity of under 20 generally share similar inundation results to that of the Minson model (example rupture shown in Figure 6a). There are 57 trench-locking, 14 homogeneous and 0 trench-creeping ruptures that fit this threshold. If we increase the threshold by 5, we observe 169 trench-locking 68 homogeneous, and still no trench-creeping ruptures. Although an increase in the threshold of 5 still has a dominance of ruptures with over 80% inundation and RMSE average of 7.6 m, the range in inundation results begins to widen much greater here (Figure 7). There is a general consistency in ruptures below a dissimilarity of 20, however, past 20 a sharper negative trend is present in inundation as the dissimilarity increases. So, we conservatively keep the lower threshold presented. We note that any threshold we pick is arbitrary; because of the way the dissimilarity value is calculated, there is still substantial variability in slip distributions and slip magnitudes. But, beneath this threshold for the synthetic ruptures, the dominant slip asperity is reproduced, and the tsunami metrics are fit reasonably well.

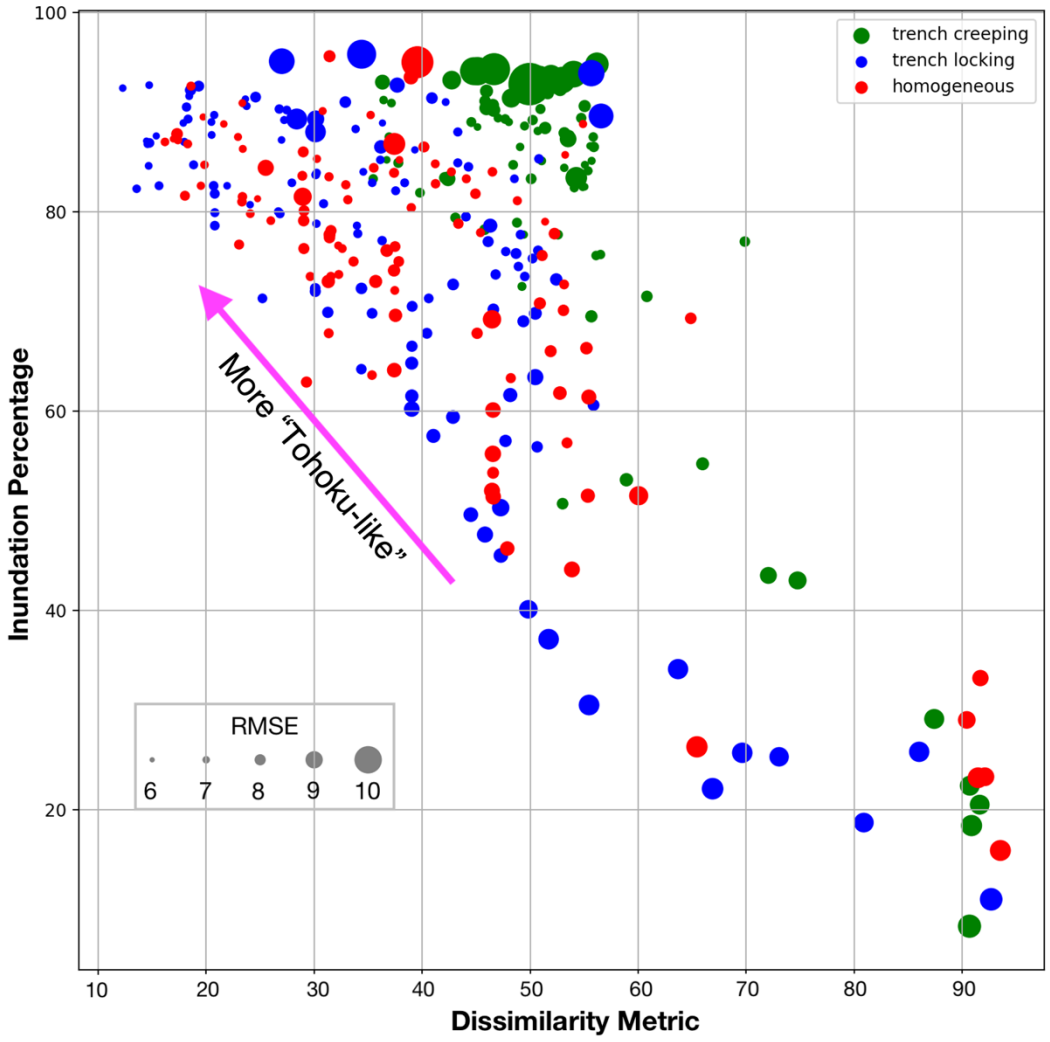

Figure 7*. Dissimilarity metric versus inundation percentage plot for all 330 ruptures that we performed inundation modeling for. The points are scaled with their RMS error and color coded based on their rupture class. The arrow depicts the trend of more "Tohoku-like" ruptures based on the three metrics.*

In Figure 7, there are some models that inundate almost all of the survey points but also have some of the largest RMS errors and variable dissimilarity. Though these ruptures occur across each class, the trench-creeping constraint produces the largest amount of them. These ruptures all

have the common characteristic of producing a large slip patch at 30 km downdip from the trench close to the shoreline of the Sanriku Coast. The dominant slip patch for these ruptures may be relatively deep, resulting in smaller surface deformation in comparison to a slip patch further up dip; however, the proximity to the coast and the magnitude of slip (over 60 m on average) generates a large tsunami relatively close to the shore. It should be recognized here that although the inundation percentages are very high for these examples (over 95%), they have relatively large dissimilarity values and RMS errors. Even though one metric appeared similar, the combination of all three metrics is important to determine the similarity to the real rupture.

3.3.3 Results for Other Global Ruptures

We now broaden our focus to the results of modeling other great earthquakes to determine if this stochastic approach can reproduce previously determined slip distributions at other subduction zones. For other M9+ events, there are not as robust inundation surveying and calculated slip inversions as there are for the 2011 Tohoku-Oki event. For the following ruptures, we only calculate dissimilarity and visually inspect ruptures to compare the stochastic ruptures to the finite fault models. Previously, we determined a specific "threshold" for acceptable dissimilarity values for ruptures for the 2011 M9.1 Tohoku event. We do not directly utilize the threshold for the preceding cases, but instead compare dissimilarity values and dominant slip distribution characteristics to evaluate whether ruptures are comparable to the slip inversions. Here, we will focus on three other M9+ events: 1960 M9.3–9.4 Chile, 2004 Sumatra M9.2, and 1964 Alaska M9.2. As stated prior, we do not have reliable coupling models for any of these event locations prior to the ruptures, we only model them using the homogeneous stochastic approach. Below are the results for the three earthquakes.

3.3.3.1 1960 Chile

We model 2,500 ruptures in 0.1 magnitude bins between M9.2 and 9.6. The domain is constrained between 37° and 46°S along strike and a down dip limit of 50 km. The simple rectangular geometry of the Ho model is first interpolated to the same slab geometry as the stochastic ruptures prior to dissimilarity analysis. The rupture domain is subdivided into 1790 triangular subfaults, with lengths around 10 km wide on average. Final magnitudes vary from M8.9 to 9.7.

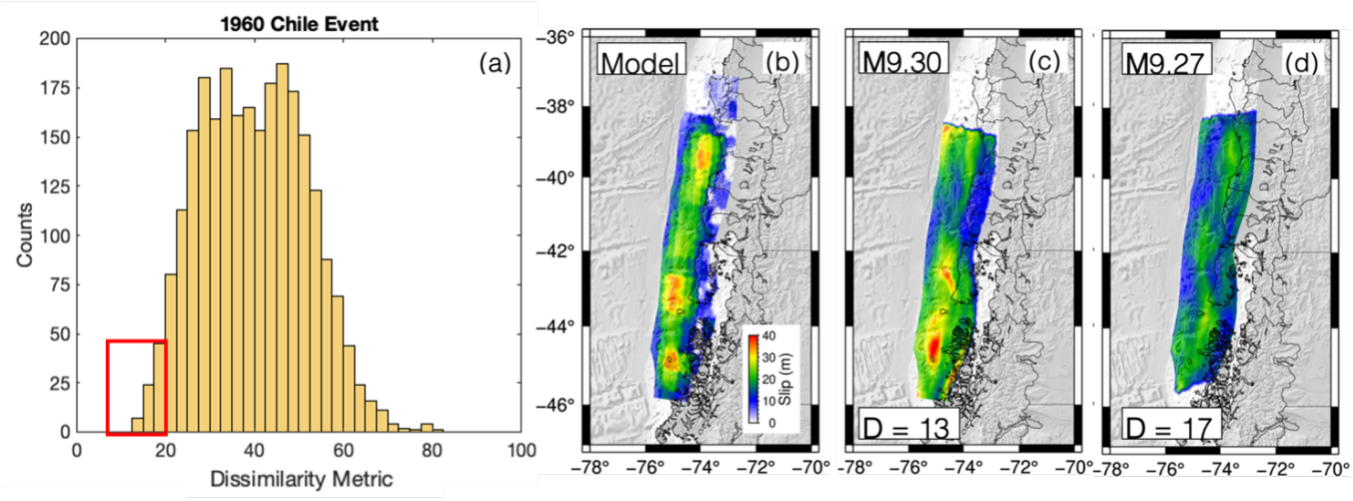

Figure 8. *(a) Dissimilarity histogram distribution with a bin width of 2.5 for the 1960 Chile rupture. Red box indicates ruptures below the Tohoku case threshold. (b) Slip model from Ho et al. (2019) that is used as the model we are trying to reproduce with the stochastic ruptures. (c) Example M9.3 rupture that has the lowest dissimilarity compared to any other modeled rupture. Color is represented by slip in meters shown in (a). (d) Same as (c) but for a M9.27 rupture and a slightly larger dissimilarity, but still beneath the threshold of dissimilarity.*

There is a similar distribution of dissimilarities with low values compared to the Tohoku example (Figure 8a). While we will not directly apply the threshold for the case prior, we will loosely use it as a comparison point. Figures 8c and 8d show two synthetic ruptures with varying dissimilarity values. The first matches the maximum slip observed in the Ho model well and there appears to be three distinct slip patches with similar peak slip values that correlate well with the locations seen in the Ho model. This stochastic rupture has a dissimilarity of 13, which is the lowest in the suite of ruptures and comparable to the lowest Tohoku rupture. The next rupture has a slightly higher dissimilarity of 17. Although the maximum slip observed does not reach over 30 m as opposed to the 40 m seen in the Ho model, the dominant slip patches are still relatively well resolved. As the dissimilarity value increases, the ability to resolve the three slip asperities quickly decreases. There are 75 ruptures of the 2,500 total ruptures that fit below the dissimilarity threshold determined for the Tohoku case. This is an increase in the percentage of ruptures that fall beneath the threshold in comparison to the homogeneous class for the Tohoku event (75 compared to 14 ruptures). Although we do not model tsunami inundation for the Chile

case, through visual inspection and calculation of dissimilarity values, we see that this stochastic slip method is able to reproduce the Chile slip inversion reasonably well.

3.3.3.2 2004 Sumatra

We now look at the 2004 M9.2 Sumatra event, which is the spatially longest rupture in instrumental history. Following from the previous analysis, we model 2,500 ruptures in 0.1 magnitude bins between M9.0 and 9.4. Since we do not fix final magnitude, final ruptures are between M8.8–9.6. The domain extends from 2°N to 14°N and slip is limited to above 50 km down dip, with a total of 1,084 subfaults of around 20–25 km in length each. The Rhie model is first interpolated to the domain geometry and then both ruptures and the slip model are interpolated to a regular grid for the dissimilarity analysis.

Figure 9 shows two examples of rupture models that have relatively low dissimilarity values. The first rupture (Figure 9c) has a large slip patch with similar peak slip as the Rhie model and dispersed smaller slip (10 m and below) throughout the rest of the model. The slip patch extends further south along the subduction zone than the Rhie model. The second rupture shown has a slightly higher dissimilarity value and is smaller than the Rhie model (Figure 9d). Its dominant slip patch is located further south but close to the Rhie model and has more scattered larger slip throughout the model.

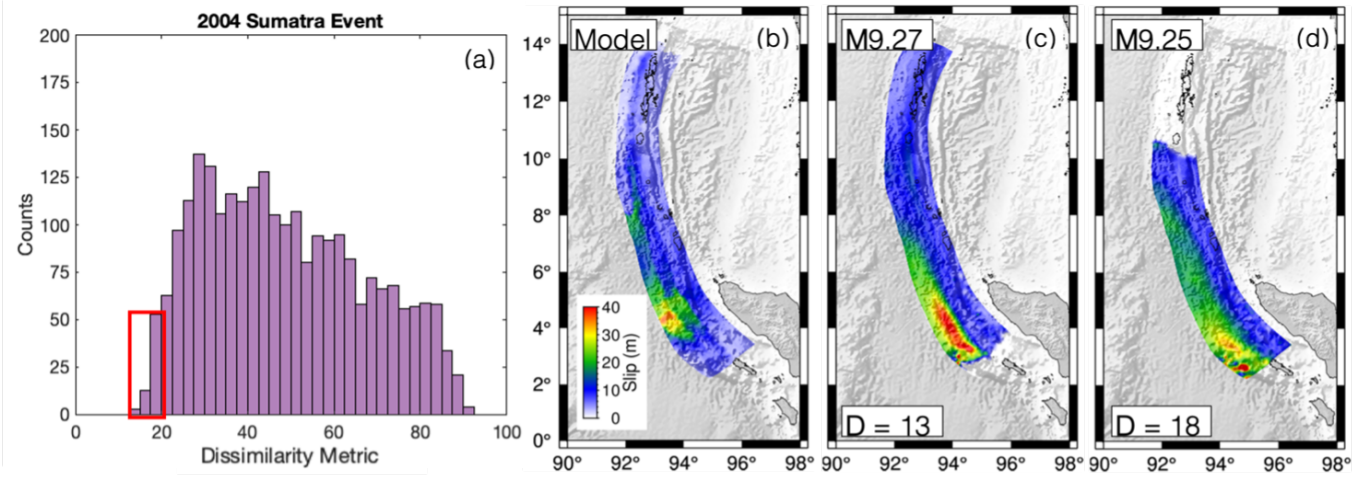

Figure 9. *(a) Dissimilarity histogram distribution with a bin width of 2.5 for the 2004 Sumatra rupture. Red box indicates ruptures below the Tohoku case threshold. (b) Slip model from Rhie et al. (2007) that is used as the model we are trying to reproduce with the stochastic ruptures. (c)*

Example M9.27 rupture that has the lowest dissimilarity compared to any other modeled rupture. Color is represented by slip in meters shown in (a). (d) Same as (c) but for a M9.25 rupture and a larger dissimilarity.

Like the Chile example, we cannot completely apply the Tohoku dissimilarity threshold to the Sumatra case. Instead, we still consider it while also using visual inspection to determine likeness. There are 79 out of the 2,500 ruptures that have dissimilarity values below the threshold, which is greater than any of the rupture classes for Japan or Chile. Within these ruptures that fall within the Tohoku threshold, all have either a dominant slip patch centered around 3°–4°N or dispersed slip throughout the entire domain. As the dissimilarity increases, the magnitude and size of the slip patch or the extent of the background slip varies more substantially. This variation is noticed in the two examples shown below. The lowest dissimilarity ruptures ($D < 15.5$) have both the dominant slip patch and the dispersed slip along most of the domain. There are 6 ruptures that have large slip patches with similar peak slip values and background slip that extends through most of the subduction zone. All the ruptures that fall below the previous Tohoku dissimilarity threshold on average express the dominant trends characterized by the Rhie model. Even though the Sumatra rupture is spatially larger and has relatively more dispersed slip throughout, stochastic modeling is still able to reproduce the slip inversion well.

3.3.3.3 1964 Alaska

Our final earthquake of interest is the 1964 M9.2 Alaska event, the largest earthquake to occur in North America and the second largest globally in instrumental history. Once more, we model 2,500 ruptures in a 0.1 magnitude bin size between M9.0–9.4. We do not interpolate the Ichinose model and calculate ruptures along the Ichinose model domain with 765 rectangular subfaults of size 16 × 16 km.

In Figure 10, we show the dissimilarity values for all 2,500 ruptures along with two ruptures with low dissimilarity to compare against the slip model. Compared to the other M9+ earthquakes, the Alaska event is not able to be fit with as low of dissimilarity values. Similar to the Tohoku case, the distribution of rupture dissimilarities is quite similar still. The mode of dissimilarity values for the homogeneous class of the Tohoku ruptures is around 50, matching the

Alaska case well. There are ruptures with relatively low dissimilarity and can fit the dominant trends of the Alaska slip inversion (Figures 10c and 10d). Both ruptures shown below experience three slip asperities in a similar location to the Ichinose model, with slip between 10 and 15 m in each region. Figure 10d experience a greater degree and dispersion of large slip throughout the modeled region, but still matches the slip inversion decently.

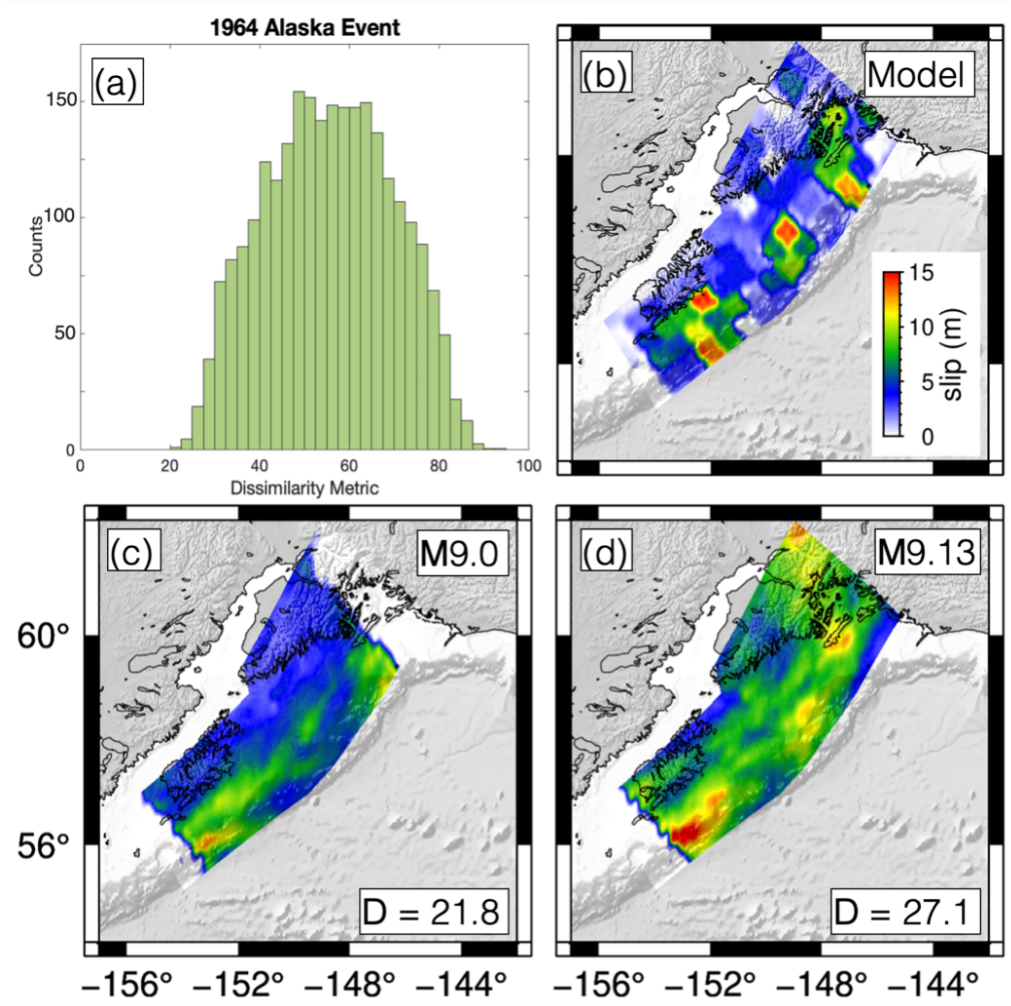

Figure 10. *(a) Dissimilarity histogram distribution with a bin width of 2.5 for the 1964 Alaska event. (b) Slip model from Ichinose et al. (2007) that is used as the model we are trying to reproduce with the stochastic ruptures. (c) Example M9.0 rupture that has the lowest dissimilarity compared to any other modeled rupture. Color is represented by slip in meters shown in (a). (d) Same as (c) but for a M9.13 rupture and a larger dissimilarity.*

While there are no ruptures that fall below the threshold we applied for the Tohoku event, we note that this is an imperfect qualifier potentially specific for Japan. Several ruptures for the Alaska event both matched the slip asperity location and peak slip relatively well, with relatively small dissimilarity values. We still consider the stochastic approach used here to successfully reproduce the dominant trends associated with the Ichinose slip pattern for some example synthetic ruptures as seen by Figure 10.

3.4 Discussion

It is worth repeating here the intent of our study. We are focused on using these past large ruptures to validate the VK ACF method for stochastic slip rupture modeling. With few and rather general constraints applied to the method, we want to validate that this method can produce realistic large ruptures. Importantly, the ruptures are all completely blind to the inversion they are being compared to. The ability of this stochastic approach to produce ruptures at different subduction zones that match these historic earthquakes will provide weight and a measure of validation that the technique may be used for future studies globally. We note, however, that there is still uncertainty in the “full stack” of a PTHA calculation.

Assessing and determining an appropriate numeric qualifier for reproducing past ruptures is difficult. For the Tohoku case, we utilize three metrics to quantify a rupture's likeness to the past event: one based on direct slip pattern dissimilarity and two based on inundation analyses. Still, there is considerable uncertainty in the ability to assess likeness between the synthetic ruptures and the event. All metrics used in this study have strengths and weaknesses associated with their results. For instance, inundation percentage is a simple binary metric that is more forgiving of the uncertainties in inundation modeling than other statistical errors would be. Since the percentage only records whether a point is wetted or not, a rupture can grossly over inundate while producing a high inundation percentage. Luckily, for the Tohoku case, we are assessing rupture similarity using three metrics in total (dissimilarity, RMSE, and inundation percentage). Still however, the three metrics presented here are not perfect indicators. We are also limited in this study by the distribution of survey locations following the 2011 tsunami. The inundation points recorded throughout Japan are not equally distributed, but rather are more densely concentrated along the Sanriku Coast and Sendai Bay where the largest concentration of points is present. This may in turn create a bias in the final RMSE even though these is only a small region effected.

Even though there are associated errors and shortcomings with the tsunami metrics, utilizing them in conjunction with the dissimilarity metric provides a greater sense of rupture likeness.

For all 330 ruptures, the RMSE of inundation has a minimum just below 7 m and a maximum just over 10 m. Regardless of rupture class, the Sanriku coast (between 38°N and 39°N) has the largest discrepancies between the model and survey. This region also experienced the largest coastal inundation following the 2011 earthquake, with some areas reaching almost 40 m in amplitude (Figure 4). Inundation residuals between modeled points and surveyed points have the largest values in the Sanriku coastal region. Unsurprisingly, if we look at residuals based on distance from the coast, we observe on average the further the inundation point was recorded, the smaller the residual is for all rupture classes (Figures 6c and 6f). Since the Sanriku coast region is misrepresented more often than other regions, there a general RMSE signal that is contained in all results. This may in turn lead to a range of RMSE values that seem confined in distribution.

It should also be recognized that calculating inundation on land is a complex process. The method for modeling inundation here uses a bare Earth digital elevation model that excludes alterations to topography including vegetation, buildings, and roads which all influence the onshore wave propagation. Similarly, we only model topography and bathymetry to the finest level of 3 arcseconds, or around 90 m resolution. This is fine for offshore wave propagation modeling, however, for terrestrial wave modeling this could still be considered coarse and lead to uncertainties in the resulting inundations. Although we can model topography to 1 arcsecond, the domain used here is so large we are unable to include that level of resolution in elevation data into the workflow. Melgar and Bock (2015) measured the terrain ruggedness index (TRI) along the Japan coast using a 3 arcsecond elevation model. The TRI determines the mean difference between elevation at one pixel and its neighboring pixels. Here they observe that the Sanriku coast has the highest values of TRI and the most instances of non-wetted inundation points by the simulations. This is similarly experienced by all our models. Yet even with the uncertainties of the inundation modeling, we can fit the tsunami inundation percentage data with over 80% for ruptures with relatively low dissimilarity values.

The four recorded earthquakes chosen for this study are all M9+ events that are characterized by a unique coseismic slip characteristics. Based on the Minson model, the 2011 Tohoku rupture experienced near-trench slip over 70 m, which had not been seen prior and was thought to be highly unlikely. The 1960 Chile event is the largest earthquake that has occurred during

instrumental times, with three large slip asperities throughout the rupture area. The 2004 Sumatra event ruptured a portion of the Sumatra-Andaman subduction zone over 1,300 km long, a length that has never been observed before. Although there have been five M9+ earthquakes since the use of seismic monitoring, we omit the 1952 Kamchatka M9.0 event. To our knowledge, while there are some geologic observations of the resulting tsunami (e.g., MacInnes et al., 2010), given the sparsity of geophysical data at the time, there is no heterogenous slip inversion that can be used as basis for comparison.

From analysis of modeling of these events, we can conclude that the stochastic modeling approach can, at least to first order, reproduce realistic ruptures for all the four events we observed, without using coupling as an a priori constraint. We note that the Alaska event had the poorest distribution of dissimilarity values out of the four ruptures. For this case, ruptures did not fall below the dissimilarity threshold set from the Tohoku case. Yet as we said before, this "threshold" is arbitrary and should not be used in full faith for other subduction zones. There are Alaska stochastic ruptures that have relatively low dissimilarity and contain the dominant slip characteristics seen in the example slip model. Because of this, we do still consider this approach applicable at reproducing that event.

Throughout all four cases, we did not vary the input statistics or assumptions for any rupture, besides potential coupling constraints or rupture domain geometry. Similarly, the four earthquakes used in this study all follow the scaling law from Blaser et al. (2010) within 2σ uncertainty for both fault length and width. Both the Alaska and the Japan events fall below 1σ as well as one of the two dimensions for the Sumatra and Chile events. So, the earthquakes used in this study are well accounted for based on the empirical scaling law from Blaser et al. (2010). While maintaining generic statistics derived from worldwide events (e.g., Goda et al., 2016; Melgar & Hayes, 2019), we can reproduce any of the M9+ ruptures relatively well. With this in consideration, the stochastic slip modeling approach does have the capability to represent large magnitude ruptures.

In Melgar and Hayes (2019), an updated value for the Hurst exponent was determined as preferable (0.4 rather than 0.75 from Mai & Beroza, 2002). While we used the older value for the Hurst exponent, we tested the impact this might have on the results mentioned prior by running models for the homogeneous case for the Japan Trench. We then computed the ruptures' dissimilarity to the Minson model and found that applying the updated Hurst exponent did not

impact the results and the observed distribution of dissimilarity values is comparable to the ones mentioned prior. So, while it may be more applicable to run the VK stochastic method with the updated Hurst exponent, for this study we find that either one produces similar results.

Although for the four events we can produce stochastic models with low dissimilarity values (D = 15–20), we could not reproduce the slip distributions with identical or lower dissimilarity values. One way we could determine whether the VK ACF holds valid for these ruptures is by comparing the slip pattern spectra with the power law VK ACF distribution. This will be the subject for future work. There is a potential that changing some of the parameters used could decrease the dissimilarity values, however, as stated above, altering the Hurst exponent had little influence. The correlation lengths used in this study have been shown to fit for the 2010 Maule M8.8 and the 2011 Tohoku events (Melgar & Hayes, 2019). This is not to say that the potential for changing the parameters might contribute to better fits to the slip models but may need to be explored more in future work. Still, we consider the best fit adequate for our study for assessing the applicability of using the VK stochastic method for modeling great earthquakes.

We note here that while we studied four of the five M9+ ruptures in instrumental time, we only focused on a singular slip inversion for each as the representative model we attempted to reproduce using stochastic modeling. For some of these ruptures, there were several other available slip models that we could have used. We provide several reasons that justify our decision for each rupture. For instance, all slip inversions used here share similar slip patterns with most other inversions for their given ruptures. Calculating dissimilarity between these stochastic models and other slip inversions for the same ruptures would not vary substantially given the large similarities between inversions and the dissimilarity metric's increase weight on high slip patches.

Small and Melgar (2021) argued that including coupling to inform slip in the stochastic workflow has the potential to impact the technique's ability to create realistic ruptures. The analyses shown here argue that this can be true. The trench-locking class of Tohoku ruptures produces a greater percentage of ruptures below the dissimilarity threshold and generally leads to a tsunami inundation pattern that more closely replicates what was seen in the post-event survey. Compared to the homogeneous class, the trench-locking class has a probability of creating a “Tohoku-like” rupture that is four times more likely (57 total ruptures compared to 14 in the homogeneous class). Meanwhile for the trench-creeping class, no ruptures below the desired

threshold are produced. This can be interpreted as the trench-creeping class has less ability to produce realistic ruptures. While including the "correct" coupling model has generally positive effects, including the "wrong" model can have very negative effects as well. So, a key finding in this work is that unless coupling is known with some certainty, for example, because it was obtained by including offshore geodetic measurements, it is safer to assume a homogenous distribution. We will note here that the nature is coupling is not fully understood. We assume here a simple relationship between slip potential and coupling ratio. If we include other fault zone characteristics like frictional stability, regions of stable sliding may potentially contribute in slip (Kozdon & Dunham, 2013); however, more is needed to be done to include such potentials in this method.

The drastic difference in the results of the two coupling models highlights the fundamental difference between them and the key characteristic of the Minson model. The 2011 Tohoku-Oki rupture was surprising when it first occurred because of the presence of large slip (~60–80 m) in the shallowest portion of the megathrust (Lay, 2018) (Figure 2a). In this model, the large slip asperity occurs below 20 km in depth, with slip occurring up to the trench. The presence of shallow slip here is directly in contrast to the fundamental assumption of the trench-creeping class. Another direct result of the trench-creeping pattern of coupling is apparent in the tsunami inundation results. At intermediate dissimilarity values (35–50), the trench-creeping class has more accurate inundation results than the other two classes at the same dissimilarity values (Figure 7). For dissimilarity values where the other classes have inundation percentages less than 80%, most of the trench-creeping ruptures are greater than 80% inundated. This discrepancy is due to the location of dominant slip for the trench-creeping class ruptures. The region of largest slip deficit rate is present directly offshore of the Miyagi Prefecture along the Sanriku Coast (38.2°N). Because of this, the megathrust in this region typically has the largest slip in the hypothetical ruptures. Although slip occurring here is at depths greater than 25 km, its proximity to the coast with enough amplitude can still create devastating tsunamis. So, even though a given rupture for the trench-creeping class has a larger dissimilarity value, it may still produce tsunami amplitudes that are similar to those of the real rupture.

The trench-locking class, on the other hand, is defined by a coupling pattern that correlates well with the Minson model. The trench-locking class has SDR accumulating all along the Japan Trench, with over 40 mm/yr of slip accumulation occurring in the same location as the dominant

slip patch in the Minson model. Since there are high SDR rates that correlate with areas of high slip in the Minson model, these areas will have a greater probability of producing higher slip in the calculated rupture models. When we are modeling ruptures, if the correct rupture geometry and magnitude are picked from the scaling laws, the trench-locking class will have the highest probability of reproducing the ruptures.

By adding the right coupling model, we can more likely produce “Tohoku-like” or realistic ruptures. This can be very helpful for future hazard studies in that we may be able to better produce realistic ruptures by including a model for coupling. However, as we have seen, the impact of choosing one model over the other produces drastically different results. Determining which coupling model is more accurate is a difficult problem as it will require extensive seafloor instrumentation (e.g., Yokota et al., 2016). Luckily, the homogeneous class which does not utilize the coupling pattern still produces realistic ruptures as seen by all three of the example global earthquakes we calculated dissimilarity for. Although this produced fewer ruptures under the dissimilarity threshold than the trench-coupling class, it still has the capability to reproduce the slip models. So, rather than potentially misrepresenting the pattern of coupling, it is best to utilize the homogeneous method for stochastic modeling unless there is more certainty in the pattern of coupling.

Finally, we note that there is still uncertainty regarding the “full stack” of a PTHA calculation. The work here is related to that fundamental question of the applicability of the stochastic method for use in hazard related studies. We make a point that this method can produce realistic large ruptures that match reasonably well past observed historic events given the general statistical assumptions. Similarly, there is potential that applying a coupling constrained background slip model in the workflow may produce better fits to the historic ruptures. But this work presented here does not provide insight on whether the method will accurately replicate future yet to occur ruptures. Subduction zones are complex systems with seismic cycles of centurial to millennial time scales which we've only observed for a limited time. The issue of whether stochastic slip can or should be deployed for a PTHA (or PSHA) calculation, given this uncertainty, remains one worthy of debate. Here, we argue that the fact that it can replicate past ruptures suggests that it should play an important role.

3.5 Conclusion

We tested whether the slip distributions calculated using stochastic slip rupture modeling are "realistic" by attempting to reproduce slip distributions that match what is seen in M9+ events recorded in instrumental time. We first started with the 2011 M9.1 Tohoku-Oki earthquake and tsunami where we assessed both a stochastic method with a homogeneous background mean model and an interseismic coupling constrained stochastic method. We quantified the dissimilarity of slip distribution between the modeled ruptures and a slip inversion for the event. In addition to the slip pattern, we modeled high resolution tsunami inundation for 330 ruptures and compared the results to an inundation survey along the eastern coastline of Japan. We found that both the homogeneous and trench-locking classes could reproduce the 2011 Tohoku-Oki slip distribution defined by the Minson model and could model tsunami inundation results matching the post-earthquake tsunami survey. The trench-creeping class, however, could not produce any ruptures that qualified as "Tohoku-like," highlighting the varying effect a coupling constraint holds on the stochastic methodology. Because of the variable influence that either coupling model has on the output ruptures, we note that without strong reason to favor one coupling model over another, coupling should be excluded from the stochastic slip process to not introduce inaccurate biases. We also showed that for other great earthquakes such as the 1960 M9.4–9.6 Chile, 1964 M9.2 Alaska, and 2004 M9.1–9.3 Sumatra stochastic slip modeling has the capability to produce realistic ruptures. So, although the trench-locking class outperformed the homogeneous class for the Tohoku earthquake, all three earthquakes studied here were able to be reproduced using the homogeneous background slip method for stochastic slip modeling. Though we cannot say the stochastic method can perfectly represent subduction zone earthquake slip statistics, we add confidence in this approach's ability to reproduce realistic large magnitude ruptures. To end, we note that by increasing seafloor GNSS instrumentation at subduction zones, we may remedy the uncertainty of the coupling patterns in the shallow most portions of subduction zones so we can utilize the coupling constraint more confidently in future studies.

References

Ammon, C. J., Ji, C., Thio, H. K., Robinson, D., Ni, S., Hjorleifsdottir, V., et al. (2005). Rupture process of the 2004 Sumatra-Andaman earthquake. Science, 308(5725), 1133–1139. https://doi.org/10.1126/science.1112260

Ammon, C. J., Lay, T., Kanamori, H., & Cleveland, M. (2011). A rupture model of the 2011 off the Pacific coast of Tohoku Earthquake. Earth Planets and Space, 63(7), 693–696. https://doi.org/10.5047/eps.2011.05.015

Barnhart, W. D., Murray, J. R., Briggs, R. W., Gomez, F., Miles, C. P., Svarc, J., et al. (2016). Coseismic slip and early afterslip of the 2015 Illapel, Chile, earthquake: Implications for frictional heterogeneity and coastal uplift. Journal of Geophysical Research: Solid Earth, 121(8), 6172–6191. https://doi.org/10.1002/2016jb013124

Blaser, L., Krüger, F., Ohrnberger, M., & Scherbaum, F. (2010). Scaling relations of earthquake source parameter estimates with special focus on subduction environment. Bulletin of the Seismological Society of America, 100(6), 2914–2926. https://doi.org/10.1785/0120100111

Bletery, Q., Sladen, A., Jiang, J., & Simons, M. (2016). A Bayesian source model for the 2004 great Sumatra-Andaman earthquake. Journal of Geophysical Research: Solid Earth, 121(7), 5116–5135. https://doi.org/10.1002/2016jb012911

Comninou, M., & Dundurs, J. (1975). The angular dislocation in a half space. Journal of Elasticity, 5(3), 203–216. https://doi.org/10.1007/ bf00126985

Davies, G. (2019). Tsunami variability from uncalibrated stochastic earthquake models: Tests against deep ocean observations 2006–2016. Geophysical Journal International, 218(3), 1939–1960. https://doi.org/10.1093/gji/ggz260

Davies, G., Horspool, N., & Miller, V. (2015). Tsunami inundation from heterogeneous earthquake slip distributions: Evaluation of synthetic source models. Journal of Geophysical Research: Solid Earth, 120(9), 6431–6451. https://doi.org/10.1002/2015jb012272

Frankel, A., Wirth, E., Marafi, N., Vidale, J., & Stephenson, W. (2018). Broadband synthetic seismograms for magnitude 9 earthquakes on the Cascadia megathrust based on 3D simulations and stochastic synthetics, Part 1: Methodology and overall results methodology

and overall results. Bulletin of the Seismological Society of America, 108(5A), 2347–2369. https://doi.org/10.1785/0120180034

Geist, E. L., Titov, V. V., Arcas, D., Pollitz, F. F., & Bilek, S. L. (2007). Implications of the 26 December 2004 Sumatra–Andaman earthquake on tsunami forecast and assessment models for great subduction-zone earthquakes. Bulletin of the Seismological Society of America, 97(1A), S249–S270. https://doi.org/10.1785/0120050619

Geuzaine, C., & Remacle, J. F. (2009). Gmsh: A 3-D finite element mesh generator with built-in pre-and post-processing facilities. International Journal for Numerical Methods in Engineering, 79(11), 1309–1331. https://doi.org/10.1002/nme.2579

Goda, K., Yasuda, T., Mori, N., & Mai, P. M. (2015). Variability of tsunami inundation footprints considering stochastic scenarios based on a single rupture model: Application to the 2011 Tohoku earthquake. Journal of Geophysical Research: Oceans, 120(6), 4552–4575. https://doi. org/10.1002/2014jc010626

Goda, K., Yasuda, T., Mori, N., & Maruyama, T. (2016). New scaling relationships of earthquake source parameters for stochastic tsunami simulation. Coastal Engineering Journal, 58(3), 1650010-1–1650010-40. https://doi.org/10.1142/s0578563416500108

Gopinathan, D., Venugopal, M., Roy, D., Rajendran, K., Guillas, S., & Dias, F. (2017). Uncertainties in the 2004 Sumatra–Andaman source through nonlinear stochastic inversion of tsunami waves. Proceedings of the Royal Society A: Mathematical, Physical & Engineering Sciences, 473(2205), 20170353. https://doi.org/10.1098/rspa.2017.0353

Graves, R., Jordan, T. H., Callaghan, S., Deelman, E., Field, E., Juve, G., et al. (2011). CyberShake: A physics-based seismic hazard model for southern California. Pure and Applied Geophysics, 168(3), 367–381. https://doi.org/10.1007/s00024-010-0161-6

Gregor, N. J., Silva, W. J., Wong, I. G., & Youngs, R. R. (2002). Ground-motion attenuation relationships for Cascadia subduction zone megathrust earthquakes based on a stochastic finite-fault model. Bulletin of the Seismological Society of America, 92(5), 1923–1932. https://doi. org/10.1785/0120000260

Gudmundsson, Ó., & Sambridge, M. (1998). A regionalized upper mantle (RUM) seismic model. Journal of Geophysical Research, 103(B4), 7121–7136. https://doi.org/10.1029/97jb02488

Hayes, G. P., Moore, G. L., Portner, D. E., Hearne, M., Flamme, H., Furtney, M., & Smoczyk, G. M. (2018). Slab2, a comprehensive subduction zone geometry model. Science, 362(6410), 58–61. https://doi.org/10.1126/science.aat4723

Herrero, A., & Bernard, P. (1994). A kinematic self-similar rupture process for earthquakes. Bulletin of the Seismological Society of America, 84(4), 1216–1228. https://doi.org/10.1785/bssa0840041216

Ho, T. C., Satake, K., Watada, S., & Fujii, Y. (2019). Source estimate for the 1960 Chile earthquake from joint inversion of geodetic and transoceanic tsunami data. Journal of Geophysical Research: Solid Earth, 124(3), 2812–2828. https://doi.org/10.1029/2018jb016996

Ichinose, G., Somerville, P., Thio, H. K., Graves, R., & O'Connell, D. (2007). Rupture process of the 1964 Prince William Sound, Alaska, earthquake from the combined inversion of seismic, tsunami, and geodetic data. Journal of Geophysical Research, 112(B7), B07306. https://doi.org/10.1029/2006jb004728

Ide, S., Baltay, A., & Beroza, G. C. (2011). Shallow dynamic overshoot and energetic deep rupture in the 2011 M w 9.0 Tohoku-Oki earthquake. Science, 332(6036), 1426–1429. https://doi.org/10.1126/science.1207020

Ji, C. (2005). Preliminary rupture model for the December 26, 2004 earthquake, off the west coast of Northern Sumatra, magnitude 9.1.

Konca, A. O., Avouac, J. P., Sladen, A., Meltzner, A. J., Sieh, K., Fang, P., et al. (2008). Partial rupture of a locked patch of the Sumatra megathrust during the 2007 earthquake sequence. Nature, 456(7222), 631–635. https://doi.org/10.1038/nature07572

Kozdon, J. E., & Dunham, E. M. (2013). Rupture to the trench: Dynamic rupture simulations of the 11 March 2011 Tohoku Earthquake. Bulletin of the Seismological Society of America, 103(2B), 1275–1289. https://doi.org/10.1785/0120120136

Kragh, E. D., & Christie, P. (2002). Seismic repeatability, normalized rms, and predictability. The Leading Edge, 21(7), 640–647. https://doi. org/10.1190/1.1497316

Lavallée, D., & Archuleta, R. J. (2003). Stochastic modeling of slip spatial complexities for the 1979 Imperial Valley, California, earthquake. Geophysical Research Letters, 30(5), 1245. https://doi.org/10.1029/2002gl015839

Lay, T. (2018). A review of the rupture characteristics of the 2011 Tohoku-Oki Mw 9.1 earthquake. Tectonophysics, 733, 4–36. https://doi. org/10.1016/j.tecto.2017.09.022

LeVeque, R. J., George, D. L., & Berger, M. J. (2011). Tsunami modelling with adaptively refined finite volume methods. Acta Numerica, 20, 211–289. https://doi.org/10.1017/s0962492911000043

LeVeque, R. J., Waagan, K., González, F. I., Rim, D., & Lin, G. (2016). Generating random earthquake events for probabilistic tsunami hazard assessment. In Global tsunami science: Past and future, volume I (pp. 3671–3692).

Birkhäuser. Li, S., & Freymueller, J. T. (2018). Spatial variation of slip behavior beneath the Alaska Peninsula along Alaska-Aleutian subduction zone. Geophysical Research Letters, 45(8), 3453–3460. https://doi.org/10.1002/2017gl076761

Lin, J. T., Melgar, D., Thomas, A. M., & Searcy, J. (2021). Early warning for great earthquakes from characterization of crustal deformation patterns with deep learning. Journal of Geophysical Research: Solid Earth, 126(10), e2021JB022703. https://doi.org/10.1029/2021jb022703

Lindsey, E. O., Mallick, R., Hubbard, J. A., Bradley, K. E., Almeida, R. V., Moore, J. D., et al. (2021). Slip rate deficit and earthquake potential on shallow megathrusts. Nature Geoscience, 14(5), 321–326. https://doi.org/10.1038/s41561-021-00736-x

Loveless, J. P., & Meade, B. J. (2015). Kinematic barrier constraints on the magnitudes of additional great earthquakes off the East Coast of Japan. Seismological Research Letters, 86(1), 202–209. https://doi.org/10.1785/0220140083

Loveless, J. P., & Meade, B. J. (2016). Two decades of spatiotemporal variations in subduction zone coupling offshore Japan. Earth and Planetary Science Letters, 436, 19–30. https://doi.org/10.1016/j.epsl.2015.12.033

MacInnes, B. T., Weiss, R., Bourgeois, J., & Pinegina, T. K. (2010). Slip distribution of the 1952 Kamchatka great earthquake based on near-field tsunami deposits and historical records. Bulletin of the Seismological Society of America, 100(4), 1695–1709. https://doi. org/10.1785/0120090376

Mai, P. M., & Beroza, G. C. (2002). A spatial random field model to characterize complexity in earthquake slip. Journal of Geophysical Research, 107(B11), ESE-10-1–ESE-10-21. https://doi.org/10.1029/2001jb000588

Meade, B. J., & Loveless, J. P. (2009). Block modeling with connected fault-network geometries and a linear elastic coupling estimator in spherical coordinates. Bulletin of the Seismological Society of America, 99(6), 3124–3139. https://doi.org/10.1785/0120090088

Melgar, D., & Bock, Y. (2015). Kinematic earthquake source inversion and tsunami runup prediction with regional geophysical data. Journal of Geophysical Research: Solid Earth, 120(5), 3324–3349. https://doi.org/10.1002/2014jb011832

Melgar, D., & Hayes, G. P. (2019). The correlation lengths and hypocentral positions of great earthquakes. Bulletin of the Seismological Society of America, 109(6), 2582–2593. https://doi.org/10.1785/0120190164

Melgar, D., LeVeque, R. J., Dreger, D. S., & Allen, R. M. (2016). Kinematic rupture scenarios and synthetic displacement data: An example application to the Cascadia subduction zone. Journal of Geophysical Research: Solid Earth, 121(9), 6658–6674. https://doi.org/10.1002/2016jb013314

Métois, M., Socquet, A., Vigny, C., Carrizo, D., Peyrat, S., Delorme, A., et al. (2013). Revisiting the North Chile seismic gap segmentation using GPS-derived interseismic coupling. Geophysical Journal International, 194(3), 1283–1294. https://doi.org/10.1093/gji/ggt183

Minson, S. E., Simons, M., Beck, J. L., Ortega, F., Jiang, J., Owen, S. E., et al. (2014). Bayesian inversion for finite fault earthquake source models–II: The 2011 great Tohoku-Oki, Japan earthquake. Geophysical Journal International, 198(2), 922–940. https://doi.org/10.1093/gji/ggu170

Moreno, M., Rosenau, M., & Oncken, O. (2010). 2010 Maule earthquake slip correlates with pre-seismic locking of Andean subduction zone. Nature, 467(7312), 198–202. https://doi.org/10.1038/nature09349

Mori, N., Mai, P. M., Goda, K., & Yasuda, T. (2017). Tsunami inundation variability from stochastic rupture scenarios: Application to multiple inversions of the 2011 Tohoku, Japan earthquake. Coastal Engineering, 127, 88–105. https://doi.org/10.1016/j.coastaleng.2017.06.013

Mori, N., Takahashi, T., & 2011 Tohoku Earthquake Tsunami Joint Survey Group (2012). Nationwide post event survey and analysis of the 2011 Tohoku earthquake tsunami. Coastal Engineering Journal, 54(1), 1250001-1–1250001-27. https://doi.org/10.1142/s0578563412500015

Murphy, S., Scala, A., Herrero, A., Lorito, S., Festa, G., Trasatti, E., et al. (2016). Shallow slip amplification and enhanced tsunami hazard unravelled by dynamic simulations of mega-thrust earthquakes. Scientific Reports, 6(1), 1–12. https://doi.org/10.1038/srep35007

Okada, Y. (1985). Surface deformation due to shear and tensile faults in a half-space. Bulletin of the Seismological Society of America, 75(4), 1135–1154. https://doi.org/10.1785/bssa0750041135

Oleskevich, D. A., Hyndman, R. D., & Wang, K. (1999). The updip and downdip limits to great subduction earthquakes: Thermal and structural models of Cascadia, south Alaska, SW Japan, and Chile. Journal of Geophysical Research, 104(B7), 14965–14991. https://doi.org/10.1029/1999jb900060

Perfettini, H., Avouac, J. P., Tavera, H., Kositsky, A., Nocquet, J. M., Bondoux, F., et al. (2010). Seismic and aseismic slip on the Central Peru megathrust. Nature, 465(7294), 78–81. https://doi.org/10.1038/nature09062

Plafker, G. (1967). Surface faults on Montague Island associated with the 1964 Alaska earthquake (p. 42). US Government Printing Office.

Razafindrakoto, H. N., Mai, P. M., Genton, M. G., Zhang, L., & Thingbaijam, K. K. (2015). Quantifying variability in earthquake rupture models using multidimensional scaling: Application to the 2011 Tohoku earthquake. Geophysical Journal International, 202(1), 17–40. https://doi. org/10.1093/gji/ggv088

Rhie, J., Dreger, D., Burgmann, R., & Romanowicz, B. (2007). Slip of the 2004 Sumatra–Andaman earthquake from joint inversion of long-period global seismic waveforms and GPS static offsets. Bulletin of the Seismological Society of America, 97(1A), S115–S127. https://doi.org/10.1785/0120050620

Rodriguez, E. E., & Russo, R. M. (2020). Southern Chile crustal structure from teleseismic receiver functions: Responses to ridge subduction and terrane assembly of Patagonia. Geosphere, 16(1), 378–391. https://doi.org/10.1130/ges01692.1

Ruhl, C. J., Melgar, D., Grapenthin, R., & Allen, R. M. (2017). The value of real-time GNSS to earthquake early warning. Geophysical Research Letters, 44(16), 8311–8319. https://doi.org/10.1002/2017gl074502

Ruiz, J., Baumont, D., Bernard, P., & Berge-Thierry, C. (2007). New approach in the kinematic k−2 source model for generating physical slip velocity functions. Geophysical Journal International, 171(2), 739–754. https://doi.org/10.1111/j.1365-246x.2007.03503.x

Scala, A., Lorito, S., Romano, F., Murphy, S., Selva, J., Basili, R., et al. (2020). Effect of shallow slip amplification uncertainty on probabilistic tsunami hazard analysis in subduction zones: Use of long-term balanced stochastic slip models. Pure and Applied Geophysics, 177(3), 1497–1520. https://doi.org/10.1007/s00024-019-02260-x

Sepúlveda, I., Liu, P. L. F., & Grigoriu, M. (2019). Probabilistic tsunami hazard assessment in South China Sea with consideration of uncertain earthquake characteristics. Journal of Geophysical Research: Solid Earth, 124(1), 658–688. https://doi.org/10.1029/2018jb016620

Shao, G., Li, X., Ji, C., & Maeda, T. (2011). Focal mechanism and slip history of the 2011 Mw 9.1 off the Pacific coast of Tohoku Earthquake, constrained with teleseismic body and surface waves. Earth Planets and Space, 63(7), 559–564. https://doi.org/10.5047/eps.2011.06.028

Small, D. T., & Melgar, D. (2021). Geodetic coupling models as constraints on stochastic earthquake ruptures: An example application to PTHA in Cascadia. Journal of Geophysical Research: Solid Earth, 126(7), e2020JB021149. https://doi.org/10.1029/2020jb021149

Small, D. T., & Melgar, D. (2023). Rupture files [Dataset]. Zenodo. https://doi.org/10.5281/ZENODO.7734845

Somerville, P., Irikura, K., Graves, R., Sawada, S., Wald, D., Abrahamson, N., et al. (1999). Characterizing crustal earthquake slip models for the prediction of strong ground motion. Seismological Research Letters, 70(1), 59–80. https://doi.org/10.1785/gssrl.70.1.59

Suito, H., & Freymueller, J. T. (2009). A viscoelastic and afterslip postseismic deformation model for the 1964 Alaska earthquake. Journal of Geophysical Research, 114(B11), B11404. https://doi.org/10.1029/2008jb005954

Tozer, B., Sandwell, D. T., Smith, W. H., Olson, C., Beale, J. R., & Wessel, P. (2019). Global bathymetry and topography at 15 arc sec: SRTM15+. Earth and Space Science, 6(10), 1847–1864. https://doi.org/10.1029/2019ea000658

Villegas-Lanza, J. C., Chlieh, M., Cavalié, O., Tavera, H., Baby, P., Chire-Chira, J., & Nocquet, J. M. (2016). Active tectonics of Peru: Heterogeneous interseismic coupling along the Nazca megathrust, rigid motion of the Peruvian Sliver, and Subandean shortening accommodation.

Journal of Geophysical Research: Solid Earth, 121(10), 7371–7394. https://doi.org/10.1002/2016jb013080

Wang, K., & Tréhu, A. M. (2016). Invited review paper: Some outstanding issues in the study of great megathrust earthquakes—The Cascadia example. Journal of Geodynamics, 98, 1–18. https://doi.org/10.1016/j.jog.2016.03.010

Wei, S., Graves, R., Helmberger, D., Avouac, J. P., & Jiang, J. (2012). Sources of shaking and flooding during the Tohoku-Oki earthquake: A mixture of rupture styles. Earth and Planetary Science Letters, 333, 91–100. https://doi.org/10.1016/j.epsl.2012.04.006

Wei, S., Sladen, A., & The ARIA Group (Caltech-JPL). (2011). Updated result 3/11/2011 (Mw 9.0), Tohoku-Oki, Japan. Source models of large earthquakes. Retrieved from http://www.tectonics.caltech.edu/slip_history/2011_taiheiyo-oki/index.html

Williamson, A., Melgar, D., & Rim, D. (2019). The effect of earthquake kinematics on tsunami propagation. Journal of Geophysical Research: Solid Earth, 124(11), 11639–11650. https://doi.org/10.1029/2019jb017522

Wilson, D. L., Baddeley, A. J., & Owens, R. A. (1997). A new metric for grey-scale image comparison. International Journal of Computer Vision, 24(1), 5–17. https://doi.org/10.1023/a:1007978107063

Yagi, Y., & Fukahata, Y. (2011). Rupture process of the 2011 Tohoku-Oki earthquake and absolute elastic strain release. Geophysical Research Letters, 38(19), L19307. https://doi.org/10.1029/2011gl048701

Yamazaki, Y., Lay, T., Cheung, K. F., Yue, H., & Kanamori, H. (2011). Modeling near-field tsunami observations to improve finite-fault slip models for the 11 March 2011 Tohoku earthquake. Geophysical Research Letters, 38(7), L00G15. https://doi.org/10.1029/2011gl049130

Yokota, Y., Ishikawa, T., Watanabe, S. I., Tashiro, T., & Asada, A. (2016). Seafloor geodetic constraints on interplate coupling of the Nankai Trough megathrust zone. Nature, 534(7607), 374–377. https://doi.org/10.1038/nature17632

Yue, H., & Lay, T. (2013). Source rupture models for the M w 9.0 2011 Tohoku earthquake from joint inversions of high-rate geodetic and seismic data. Bulletin of the Seismological Society of America, 103(2B), 1242–1255. https://doi.org/10.1785/0120120119

CHAPTER 4

The Likely Slip Distributions of the Mw 9 1700 Cascadia Earthquake

The work detailed in this chapter was made possible by the data collection from SeanPaul La Selle and Andrew Meigs. As well, the workflow and conceptualization were developed in collaboration with my advisor, Diego Melgar. I was the primary person for the analysis, investigation, and did all the writing.

4.1 Introduction

A great megathrust earthquake occurred at the Cascadia subduction zone (CSZ, Fig. 1A) on 26 January 1700. Precise knowledge of this date, unusual for such old earthquakes, was established by association of written records of a tsunami observed in Japan without any accompanying shaking (Satake et al., 1996) and with precise tree ring dating of submerged coastal forests along a ~70km stretch of southern Washington (Yamaguchi et al., 1997). Other terrestrial proxies provide evidence of the event and are widespread across the coastal Pacific Northwest in marshes and lakes – including coastal subsidence inferred from abrupt depositional contact changes and sandy deposits interbedded with tidal marsh mud interpreted as paleotsunami deposits. Marine evidence for such an event also exists – turbidites persist across the CSZ and are inferred to have occurred from coseismic shaking. These additional proxies are not as tightly constrained in age, however, with dating uncertainties of decades to centuries (Staisch, 2024). In aggregate, all these clues are typically assumed to be evidence for a single "wall-to-wall" Mw 9 earthquake spanning from the Mendocino triple junction in the south to Vancouver Island in the north (Fig. 1A). Given dating uncertainties, with just these terrestrial proxies, we cannot in fact rule out the possibility that the last great Cascadia earthquake could rather have been a rupture sequence of events closely spaced in time (years to a few decades apart). Previous modeling determined that the amount of paleoseismically inferred coastal subsidence along with the tsunami observations in Japan can indeed be explained this way

(Satake et al., 2003, Melgar 2021). Similarly, from studies of events prior to the 1700 rupture it is widely accepted that partial ruptures are common (Goldfinger et al., 2012).

The other key piece of evidence for the 1700 event is determined from analysis of a larger catalog of historical Holocene turbidites. From this catalog, it has been interpreted that, in addition to the 1700 event, the CSZ may have ruptured in 18 other full or nearly full margin events in the last 10 ka, creating a recurrence rate of ~500 years (Goldfinger et al., 2012). To interpret the turbitdite records, the "confluence test" and the lithostratigraphic correlation methods, both foundational to the views of how Cascadia is thought to fail, are a matter of debate (Atwater et al., 2014; Howarth et al., 2021; Hill et al., 2022, Sahakian et al., 2024). Recent work focused on using updated assumptions for turbidite age assessment and submarine sedimentological processes has further highlighted the uncertainty and difficulty in determining coeval turbidite deposition (Staisch, 2024). In short, it is not debated that there are widespread earthquake-triggered turbidites in the CSZ, but rather, it is debated that they can be assumed to be synchronous and representative of full margin ruptures. Part of the difficulty is that presently, it is not possible to model the full causal chain from earthquake to ground motion, to triggering of a turbidite, and lastly, to its subsequent deposition. This then makes testing which kinds of ruptures are consistent with observation non-trivial.

Understanding how Cascadia last ruptured is thus still open for debate and important because, to adequately understand future hazard, we must understand past earthquake cycles. The objective of our work is to constrain the possible slip distributions that best fit the proxies that can be modeled at present: the Japan tsunami records, coastal subsidence, and regional paleotsunami deposits. Past studies have attempted this in different ways by focusing on only one or at most two of these proxies (Satake et al., 2002; Leonard et al., 2004, 2010; Witter, Zhang et al., 2012; Wang et al., 2013; Melgar, 2021). Of notable difficulty has been modeling the local and regional tsunami inundation, and assessing which ruptures are consistent with it. Our work does just this: we show which earthquakes can be made consistent with all three proxies, paying particular attention to regional tsunami inundation.

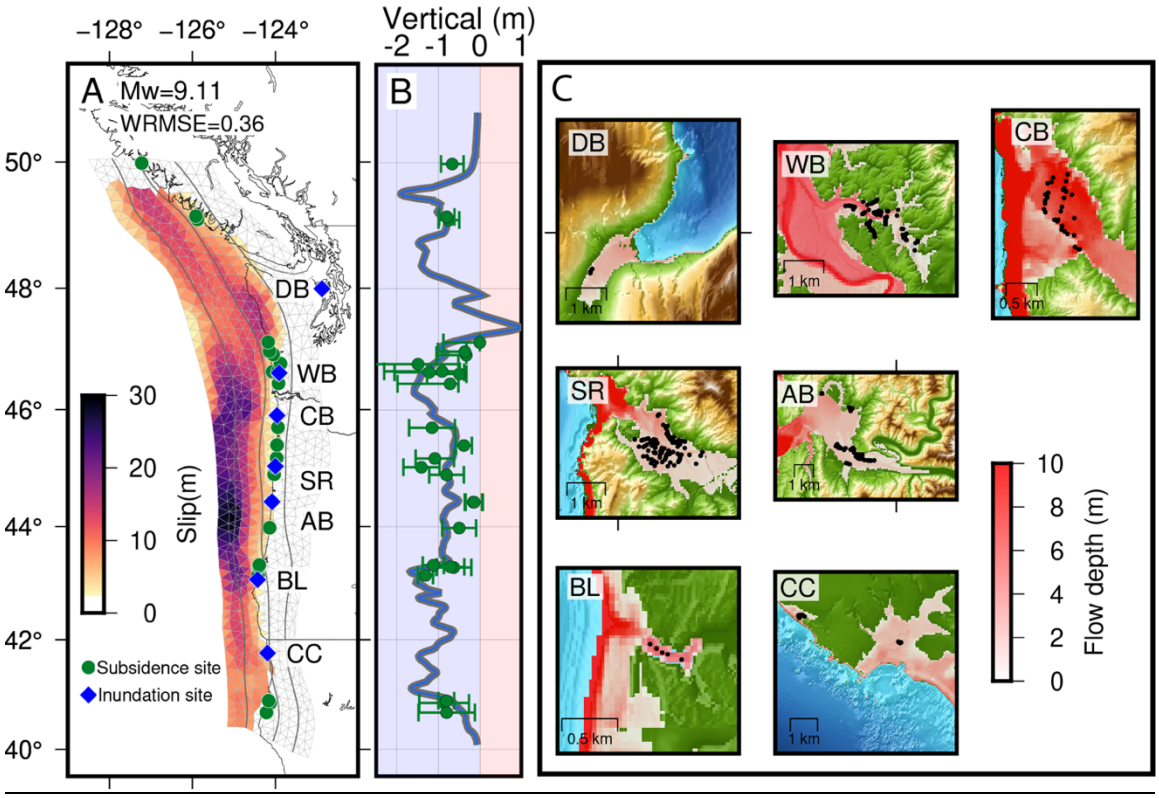

Figure 1: Best fit full margin rupture that fits all 3 paleoseismic proxies used in this study. (A) Slip model for a M9.11 earthquake. Subsidence and inundation sites shown as green dots and blue diamonds. Contours in depth match the 10 km interval for the Slab2 model from (Hayes et al., 2018). (B) Coastal deformation for the slip model in (A). Green points depict subsidence sites with their errors bars estimated from microfossils from (Leonard et al., 2010; Kemp et al., 2018; Padgett et al., 2021). Coastal subsidence for this event fits with a WRMSE of 0.36m. (C) 7 coastal sites with recorded paleotsunami sand deposits and the maximum inundation flow depth for the model in (A). The sites from North to South: Discovery Bay, WA (DB), Willapa Bay, WA (WB), Cannon Beach, OR (CB), Salmon River, OR (SR), Alsea Bay, OR (AB), Bradley Lake, OR (BL), and Crescent City, CA (CC). Points depict locations of sand deposits where the colors black, gray, and red express deposits with flow depth exceeding the depth threshold of 0.5 m and no flow recorded, respectively.

We test the efficacy of full margin events as well as sequences of partial margin ruptures. We utilize a catalog of 37,500 stochastic, heterogenous slip models between Mw 7.8 – 9.2 (Melgar, 2021) (see methods for rupture calculation technique). We use a general workflow for

determining both adequate full margin events and rupture sequences by comparing models against the 3 proxies attributed to the 1700 event. The first two stages of the process focus on deformation modeling for coastal subsidence (Fig. 1B) and tsunami modeling for estimating wave heights in Japan at locations with inferred amplitudes (Satake et al., 2003). The last stage focuses on regional inundation modeling at 6 coastal marsh lands and 1 coastal lake, where the sites span from northern Washington to northern California (Fig. 1). Each of these has well defined geolocations where the tsunami deposits have been identified in gouge cores, as well as estimates for sand bed thickness. Two sites (AB and SR) stand out based on the large numbers of observed sand deposits.

Based on this, we can subset the initial catalog of 37,500 candidate earthquakes to only 900 full and partial margin ruptures that satisfy the first two constraints – around 100 ruptures match the regional coastal subsidence and the estimated tsunami heights in Japan. The other 800 ruptures match their local coastal subsidence but produce tsunami heights in Japan that could be considered unappreciable. As will be discussed later, we must have both types of events ones with appreciable and unappreciable tsunamis in Japan to generate rupture sequences. For each earthquake, we model regional tsunami inundation for 4 hours to confidently record the initial wave arrivals and possible high energy secondary waves created by a complex slip distribution and bathymetry or topography near the sites (see methods) (Fig. 1C). Tide levels during tsunami arrival can influence results by aiding or hindering inundation (Zhang et al., 2011) (Fig. 2). For the ruptures we previously determined to fit the Japan tsunami we apply low tide conditions matching the estimate for the 26 January 1700 earthquake at 21:00 PST (Mofjeld et al., 1997). At several locations along the Cascadia margin, the hindcast tide projection ranges from 0.3-0.7 m above NAVD88 vertical datum. Instead of varying the tide level at each site, we use a generalized static tide level of 0.3 m. For testing the viability of rupture sequences which occur during unknown times, we must assume coastal conditions can vary. Thus, for the tsunamis resulting from ruptures that we do not consider the 1700 mainshock, we use 5 different tide levels between +3 m and -0.8 m, which represent the site averaged extreme high and low along with the MHHW (+2.1 m) and MLLW (0 m) tides in reference to NAVD88 for the Pacific Northwest (see methods).

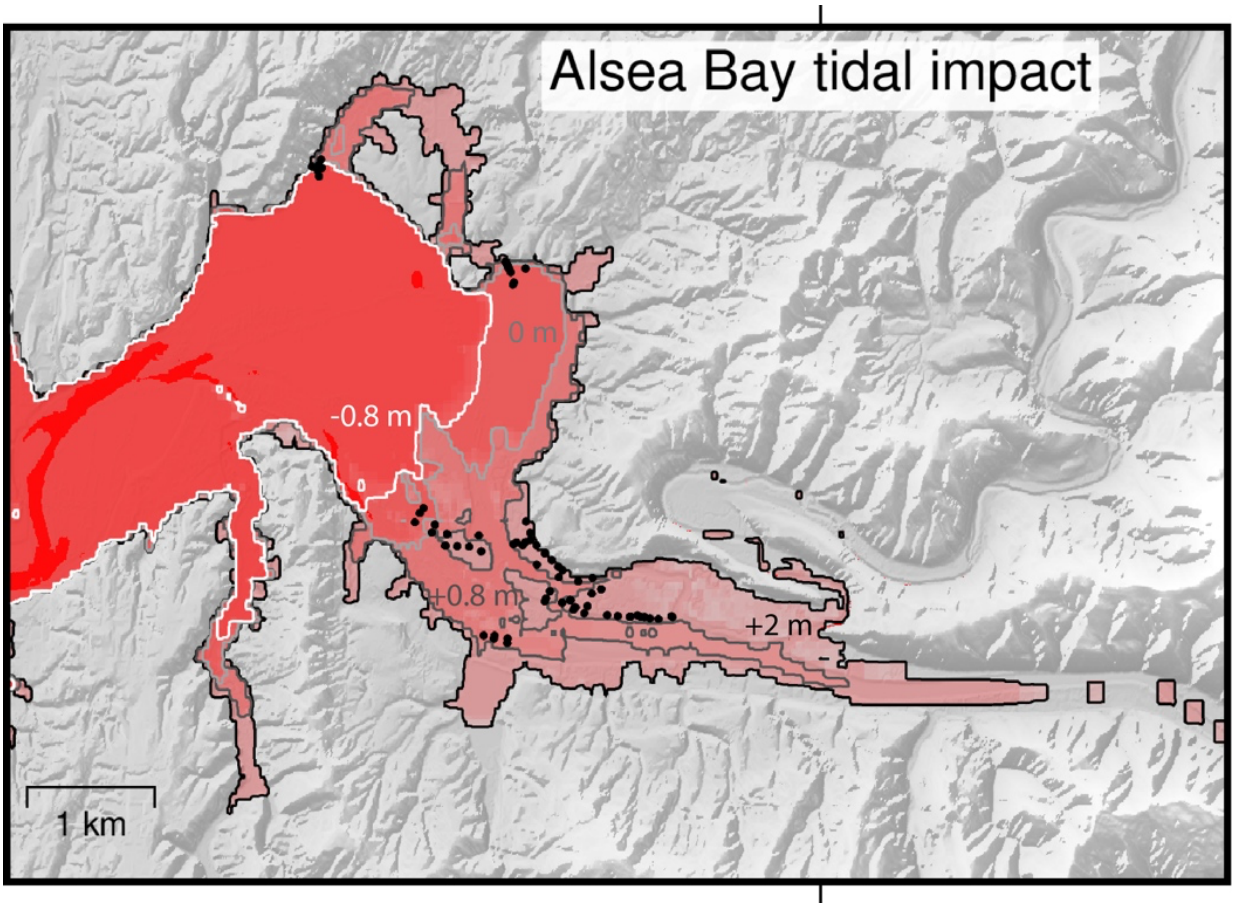

Figure 2: Tidal influence on inundation. Map depicts Alsea Bay, Oregon, showing inundation extent for a M8.76 rupture occurring during 4 different tide stages: +2 m, +0.8 m, 0 m, and -0.8 m. Elevation and tides referenced to NAVD88 vertical datum. Inundation region shows areas where water depth is greater or equal to 0.5 m. Black points show the 1700 tsunami sand deposit locations used in the study from Spruell (2018).

4.2 Data and Methods

4.2.1 Generating Stochastic Slip Ruptures

Here, we describe the process for generating ruptures using the multi-data earthquake source modeling and inversion toolkit MudPy (https://github.com/dmelgarm/MudPy). To forward model kinematic slip distributions used in this study, we utilize the method specifically from Small and Melgar (2021). A complete, step-by-step description for generating stochastic slip ruptures can be found there as well as in the original publication describing the approach (Melgar et al.,

2016). In this work we did not generate new ruptures but instead used a database of 37,500 ones previously generated for Cascadia (Melgar, 2021). Nonetheless, because the stochastic ruptures are so critical to this work we explain the methodology in brief.

The first step for generating ruptures is defining the fault domain on which slip will be allowed to occur. A 3D megathrust fault mesh was created that is discretized into 1,300 triangular subfaults based on the model for the CSZ from Slab2.0 (Hayes et al., 2018). The mesh extends to 40 km depth downdip, however, depending on the assumptions applied, slip may not always occur to this depth, as detailed below.

To create the stochastic slip models, we must first determine the magnitudes of interest. Then, for a simulation to be produced, we pick a subfault at random as the hypocenter and make a random draw from a stochastic scaling law (Blaser et al., 2010) to determine the rupture length and width that can participate in slip. These scaling laws follow a log-normal probability density function, which creates variability in the rupture area between models within the same magnitude bin. As a result, events of the same magnitude will have different dimensions.

Once the fault portion that will participate in the rupture is determined, the pattern of slip must be calculated. Here, we rely on the assumption that slip on a fault can be approximated as a spatially random field best defined by the von Karman auto-correlation function (VK-ACF) (Mai and Beroza, 2002). With the VK-ACF, we calculate a correlation matrix between each of the subfaults based on the distance that separates them. The utility of the VK-ACF results from its simplicity and dependence on only 3 critical parameters inferred from the statistics of slip models of large magnitude earthquake: a_s, a_d, and H. These first two parameters are correlation lengths of the along-strike and along-dip directions that control the dominant asperity sizes in the slip pattern. The last parameter, H, is the Hurst exponent, which controls the short wavelength structure between asperities. The scaling laws used for the correlation lengths, along with the value for the Hurst exponent, have previously been determined characteristics of slip models of past earthquakes (Mai & Beroza, 2002; Goda et al., 2016; Melgar and Hayes, 2019).

With all the parameters of the correlation matrix determined, a formal covariance matrix is obtained from

$$\widehat{C_{ij}} = \sigma_i C_{ij} \sigma_j \ ,$$

where σ is the standard deviation of slip. This is determined from the ratio of the mean slip of an earthquake to the standard deviation and has been previously calculated from the USGS database of earthquakes to be 0.45 (Melgar and Hayes, 2019). Following the generation of the covariance matrix, the Karhunen-Loeve (K-L) expansion is applied (LeVeque et al., 2016). The K-L expansion states that the stochastic vector, s, that contains the slip of each of the contributing subfaults, is defined as

$$s = \mu + \sum_{k=1}^{N} z_k \sqrt{\lambda_k + \nu_k} \, .$$

Here, the statistics of the VK-ACF are enforced by the eigenvalues and eigenvectors, λ_k and ν_k, determined from the correlation matrix, C_{ij}, which are then applied to a background slip model, s. Lastly, z_k is a vector of normally distributed random numbers with a mean of 0 and a standard deviation of 1, which is introduced to apply stochastic variability to the final slip vector.

The application of the K-L expansion allows us to generate any number of unique slip distributions, and importantly, we can create stochastic slip models that are then informed by fault zone characteristics (specifically geodetic coupling) (Small and Melgar, 2021). What this means is when we include a coupling model into the workflow, regions of high coupling will often experience greater slip or are more likely to participate in slip, and regions where coupling is low will likely experience less slip. We incorporate the coupling models as the background mean model by re-scaling the slip deficit rate into slip based on the desired magnitude. This model is then applied to the K-L expansion to then create the final, heterogeneous slip distribution.

To utilize coupling models to inform the hypothetical slip distributions, we rely on the assumption that there is a relationship between slip and coupling, which has been observed in many recent large earthquakes (e.g., Barnhart et al., 2016; Konca et al., 2008; Li & Freymueller, 2018; Moreno et al., 2010; Ozawa et al., 2011). An important issue is whether ruptures produced in this way lead to slip distributions that are realistic for large magnitude events. They do, this has been validated by comparing the outputs to slip distributions from recent and historical Mw 9+ ruptures (Small and Melgar 2023).

Five different assumptions on the background slip models are utilized to create the full suite of 37,500 unique ruptures (Fig. 3). Three of these models are based on previously published

coupling models (called the Gamma, Gaussian, and Li models) (Schmalzle et al., 2014; Li et al., 2018). By using any of these models in the rupture generating workflow, we are introducing the assumption that the pattern of coupling prior to the 1700 event was similar to what is seen today. The other two background slip models are homogeneous slip and vary in the assumed downdip limit of slip available in the models. One is based on the 1 cm/yr slip deficit contour, which is a commonly assumed downdip limit of coseismic slip (Frankel et al., 2015). The last background model corresponds to the observed top of the slow slip zone, about 30-40 km in depth.

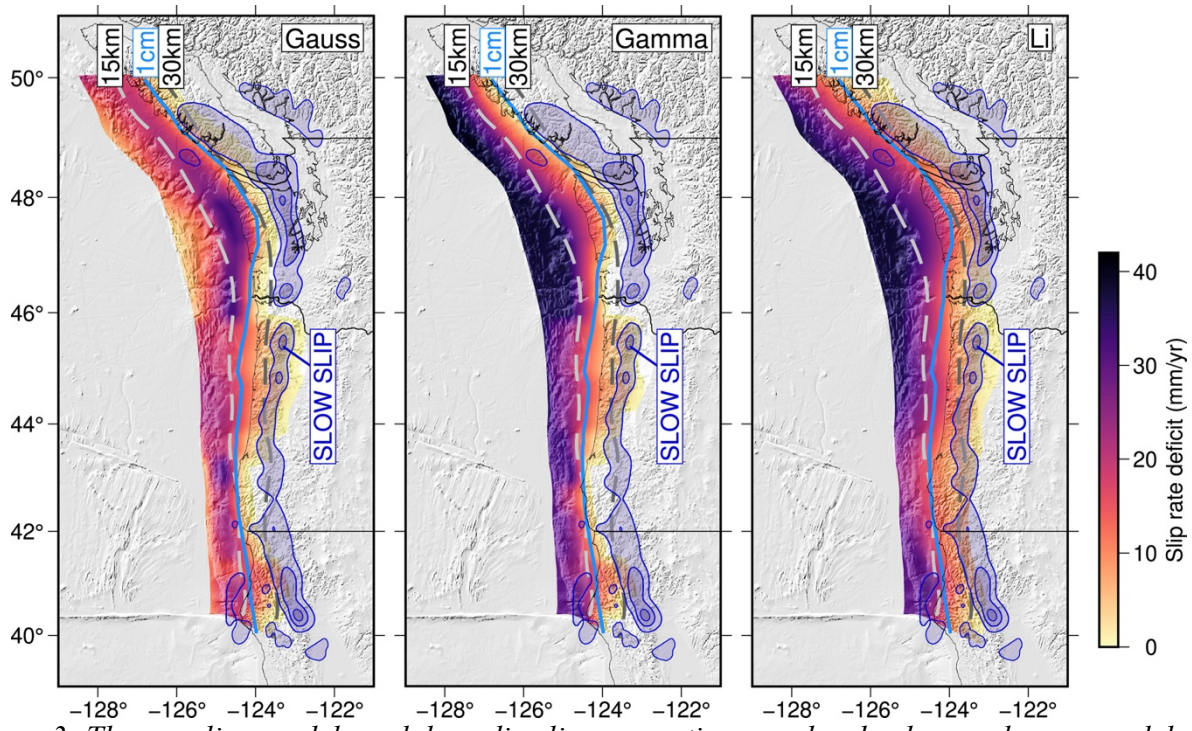

Figure 3: The coupling models and downdip slip assumptions used as background mean models. The three heterogeneous models are representative of the Gauss, Gamma, and Li coupling models (Li et al., 2018; Schmalzle et al., 2014). The dashed lines are depth contours of the slab. The blue line denotes the 1 cm/yr slip deficit contour, and The slow slip region is the aggregated slip zone from Bartlow (2019). Figure from Melgar et al., (2022)

In total, 37,500 stochastic slip models were created between Mw 7.8-9.2. For each of the 5 background models there are 7,500 ruptures. A rake of 90 degrees is assumed for all events, so slip is predominantly occurring in the dip-slip direction. The final magnitude, hypocentral

location, and rupture area are left unconstrained, allowing for slip distributions to vary in all respects from one another.

4.2.2 Deformation Modeling

We calculate the three-dimensional coseismic deformation for both the onshore and offshore portions of the model domain. We assumed a homogenous half-space with a rigidity of 30GPa and used an implementation of the Okada equations (Okada 1985) for triangular subfaults (Comninou & Dundurs, 1975). For tsunami modeling frequently, only the signal from vertical seafloor displacement is utilized, which neglects any influence from the horizontal motion of steeply sloping bathymetric features. This might then underrepresent the full tsunamigenic potential of an earthquake (Tanioka and Satake, 1996). Instead, for the tsunami initial condition we define the surface deformation as the sum of the true vertical displacement plus a "pseudo vertical" displacement which is obtained as the product of the horizontal motion and the gradient of bathymetry (Melgar and Bock, 2015; Bletery et al., 2016). For very steep shelves this can add ~10% extra vertical deformation. We do not, however, incorporate any secondary mechanisms of deformation like submarine slope failures or splay fault activation, which may impact tsunami generation.

For analyzing the fit with the coastal subsidence constraints, we compute the coseismic deformation as a result of each of the rupture models at a 2 km interval along the Pacific Northwest coast and use the node closest to the subsidence sites as their respective values. In this, we assume all deformation occurs coseismically. This may introduce some under or overestimation of the full deformation signals, since postseismic afterslip or bulk mantle relaxation would likely occur and be recorded by the paleosubsidence estimate; however, at current there is no way to disentangle the coseismic influence from the full observed land level change through microfossils alone.

4.2.3 Tsunami Modeling

The modeled seafloor deformation is incorporated as the initial condition into the code GeoClaw (https://www.clawpack.org/geoclaw.html), which solves the finite volume 2-D depth-averaged shallow water equations for flow over varying topography. This code utilizes adaptive mesh refinement (AMR), which allows for regions of interest and tsunami complexity to be

modeled with greater resolution, and others coarser. This allows us to model more efficiently both transoceanic tsunami propagation to Japan as well as onshore tsunami inundation at multiple locations.

Model setup for tsunami propagation varies between those run to Japan and those to 7 inundation sites along the Pacific Northwest. For inundation in Japan, we rely on previous results determined from Melgar (2021) and point there for greater detail on the methods for determining the tsunami heights at those coastal sites. Here, we predominantly focus on the regional tsunami inundation models. We determine inundation percentages at each site by implementing each core location into our tsunami models and utilizing the fixed grid monitoring component of GeoClaw, which determines the highest recorded water height at the given point.

To increase efficiency of model generation, we use 7 AMR levels, with the starting coarseness of 6 arcminutes which is refined with proximity to the coast to its final resolution of 1 arcseconds (~30 m). Depending on the level of refinement, tsunami propagation is run over 3 different bathymetric models: SRTM15+ (Tozer et al., 2019) for levels up to 15 arcseconds, then the US Coastal Relief Model (CRM) up to 3 arcseconds, and for nearshore/onshore propagation with a resolution of 1 arcseconds, the 1/9 arcsecond Continuously Updated Digital Elevation Model (CUDEM) is used. All coastal DEMs are referenced to the NAVD88 vertical datum. Tsunami inundations are run for 4 hours of model time at all 7 sites (see below for site selection). We employ a generalized Manning bottom friction coefficient of 0.025 for the entire domain, onshore and offshore.

We vary the tide levels at which we model inundation during depending on the specific rupture's ability to produce the tsunami heights in Japan. Within Geoclaw, only static homogeneous tide levels may be included as a user defined parameter in the inundation models. Because we model inundation at all sites simultaneously, we use an averaged tide level for all sites, however, tide levels generally vary less than 0.5 m across sites. For ruptures that can satisfy the Japan tsunami criteria (100 total), we only run inundations at an average tide level of 0.3 m that matches the range of hindcast estimates for the 26 January 1700 earthquake at 21:00 PST between northern California and norther Washington (Mofjeld et al., 1997). This is then the only tide level used for all tsunami models for the full margin events. For all other ruptures that do not produce the tsunami heights required in Japan, we model inundation at 5 different tide levels since for these hypothetical ruptures, there is no true constraint on the tide level or occurrence

time. The 5 other tide levels are as followed: +3.0 m, +2.1 m, +0.8 m, 0 m, and -0.8 m with respect to NAVD88 vertical datum. The bounding tide levels match the maximum and minimum recorded tides between July 2021 and July 2022. The second highest and lowest tides (+2.1 and 0 m) fit the average MHHW and MLLW tide projection at the 7 coastal sites, which account for the average of all high and low tide levels computed over a 19 year period. Depending on the tide level used, inundation at each site can be increased or decreased, showing a clear influence that tides can play on inundation potential (Fig. 2 & 4).

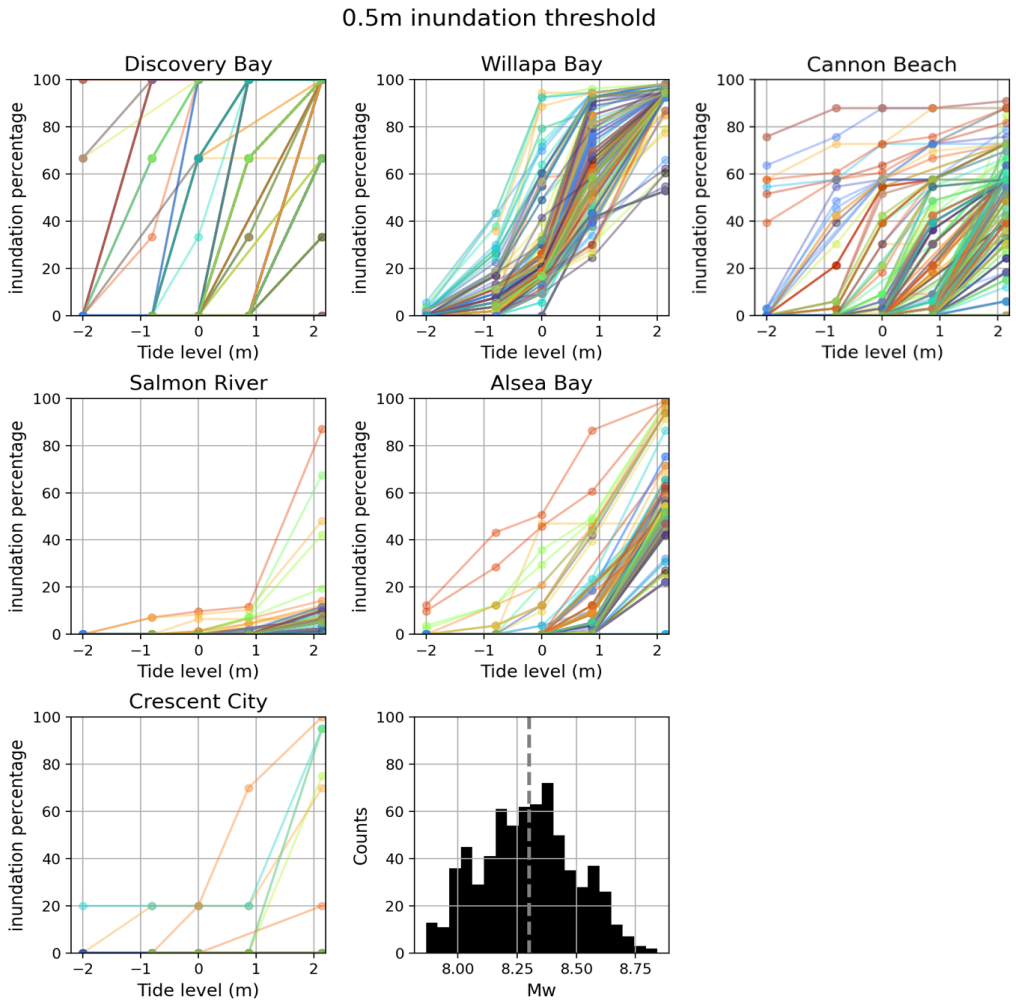

Figure 4: Inundation percentage with respect to tide level during rupture initiation. Each plot depicts inundation at an individual site. Points connected with the same-colored line segments represent inundations from a single rupture. For all sites, as the height of tide increases, the higher the inundation percentage becomes. We neglect to include Bradley Lake here as no

ruptures other than the mainshock events – which are not included here – could inundate this site, regardless of tidal stage. The histogram shows the magnitude distribution of ruptures depicted in the plots. The gray vertical line shows the mean magnitude. No ruptures used here produced the tsunami heights > 30 cm in Japan.

We assess a rupture's ability to adequately inundate each site based on the maximum flow depth recorded at each core deposit location rather than on inundation area. For inundation to be considered at a deposit location, the tsunami flow depth must surpass 0.5 m, which we consider the minimum required flow depth for deposition of sand deposits based on various sediment transport models for some recent earthquakes (Kench et al., 2008; Goto et al., 2014). It is important to note that at some sites with deposits found in current tidal flat zones at an elevation less than 2-3 m (e.g., Alsea Bay), after including tides and coseismic subsidence, some of these deposits are below sea level. If we only consider the maximum water depth at the sites, at the higher tide levels, some of these deposits will always inundate since the combination of the subsidence and tide level make the deposit under at least 0.5 m of water. To remedy this, we require that for inundation to be considered at the deposit, the maximum flow depth must be greater than 0.5 m above the submergence depth created by the possible subsidence and tide.

4.2.4 Subsidence Estimates

Coastal subsidence is recorded stratigraphically in many of Cascadia's coastal wetlands (Fig. 5). These estimates for coseismic deformation come from a variety of geologic methods. Early endeavors for estimating prehistoric coseismic subsidence utilized qualitative and quantitative methods that produced results with rather large error margins, often between +/- 0.5-1.0 m (Shennan et al., 1996). To improve these estimates, studies utilized techniques that incorporate quantitative foraminiferal-based transfer functions where fossil assemblages found stratigraphically are correlated to past tidal elevations, which can more precisely estimate site specific subsidence (e.g., Hawkes et al., 2011). This has led to the development of the Bayesian transfer function (BTF), which models non-unimodal taxa-elevation relationships (e.g., Kemp et al., 2018). Here, we utilize three paleogeodetic subsidence estimate datasets are used as coastal deformation constraints (Leonard et al., 2010; Kemp et al., 2018; Padgett et al., 2021). Most subsidence estimates utilized here were determined through BTF analysis, however, we

incorporate some estimates in Northern California from Leonard et al. that have greater uncertainties; however, these points do not conflict with the more recent neighboring estimates.

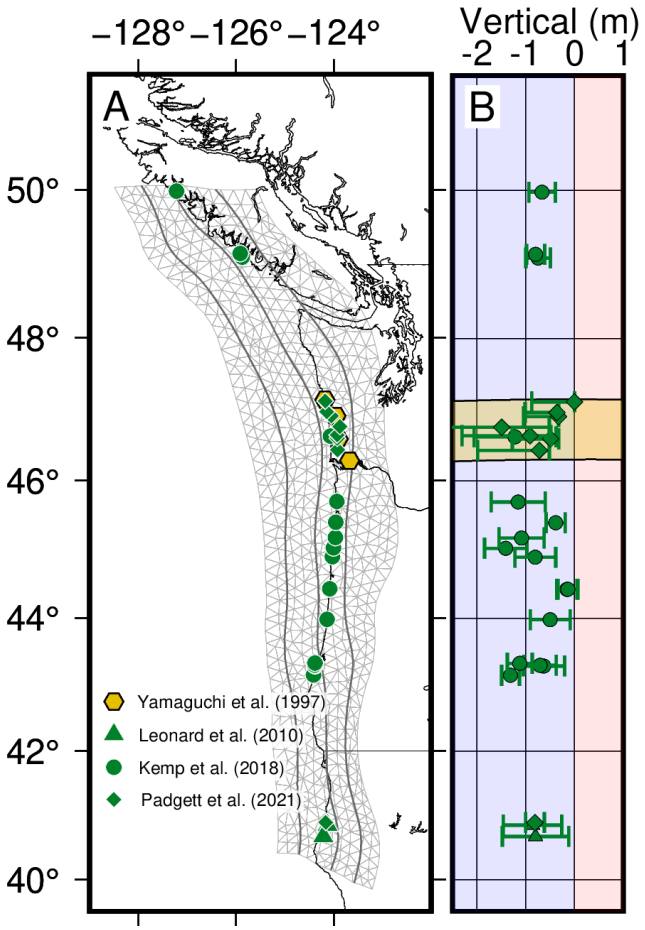

Figure 5: Locations of the paleosubsidence estimates from Leonard et al. (2010), Kemp et al. (2018), and Padgett et al. (2021) with their associated values and uncertainties. Also shown is the locations of submerged ghost forests from Yamaguchi et al. (1997)

The use of subsidence estimates to constrain our rupture models is similar to work previously done (Melgar 2021). Our work builds upon that by incorporating an additional, more recently published dataset (Padgett et al., 2021) in addition to the other two datasets. By doing so, we have increased the number of sites used from 18 coastal locations to 26 (Fig. 5). We also vary our technique for assessing the variation between our modeled deformation and the site estimates. To control for the variable quality of the subsidence estimates, when we employ a

weighted root mean square error (WMRSE) for comparison of our models to the estimates. This error value is thus weighted by the uncertainty for each of the individual subsidence estimates. In general, the uncertainties are less than +\-0.4 m, however, for some sites, these reach over +/-0.8 m (Fig. 5B).

4.2.5 Inundation Site Selection

Tsunami deposits are identified using gouge cores. Deposits are generally identified and associated with inundation from a tsunami source from the presence of a soil horizon overlain by a thin, sandy deposit. While the presence of a sand deposit can be easily attributed to a tsunami, the absence of sand beds does not necessarily mean inundation did not reach that deposit. So, we only utilize the presence of sand as a metric for evaluating inundation of our models. We note tsunami sand deposits have been located at various other locations within this region. To reduce computation cost of running inundation at multiple sites, we only incorporate 7 sites across northern California, Oregon, and Washington (Fig. 1A). These sites are chosen based on their regional distribution, precise geolocations of cores with observed sand, record of deposit thickness, and overall impact in the history of the CSZ. For Discovery Bay, Willapa Bay, and Crescent City, site locations were determined through georeferencing published figures of core locations with Google Earth, which may introduce some small human error in correcting locating core locations. Below we detail each inundation site from South to North and provide rationale for the inclusion of the site in this study.

Crescent City, CA (Hemphill-Haley et al., 2019): Situated in northern California, Crescent City is the southernmost site used in this study. It is also located in a region between sites with coastal subsidence estimates used in this study, providing the only point with an observed tsunami for a section of coast 200 km long (Fig. 1A). From Crescent City, we include tsunami deposits associated with the 1700 event at Marhoffer Creek marsh and Elk Creek wetland. Marhoffer Creek is located directly adjacent to Pebble Beach north of the city. Core deposits are found less than 100 m from the shoreline and around 4 m in elevation. Tsunami deposits for the 1700 event are observed at least 450 m inland. The Elk Creek site is situated in a flat, low elevation alluvial valley with deposits located approximately 1 km inland from the harbor. Cores here reach a maximum elevation of just below 2.5 m. Only 4 sand deposits associated with the 1700 event are observed here.

Bradley Lake, OR (Kelsey et al., 2005): This site is considered one of the most important and influential terrestrial tsunami deposit recorders, with 17 disturbance events associated with CSZ earthquakes since the damning of the lake 7300 years ago. Bradley Lake is situated 500 m inland, impounded by sand dunes over 10 m above sea level which act as a barrier of entry for tsunamis and storm surges. All but 4 deposits associated with a past earthquake record a tsunami large enough to breach the dunes. It is inferred that Bradley Lake has recorded both larger full margin earthquakes as well as segment ruptures.

Alsea Bay, OR (Spruell, 2018): Alsea Bay estimated to have experienced some of the smallest coseismic subsidence (~0.5 m) when compared to other sites along the Oregon Coast. However, this site has tsunami deposits up to 7 kilometers inland from the mouth of the Alsea Bay estuary. This seeming dichotomy between low subsidence and wide inland extent of tsunami deposits makes Alsea Bay a rather unique study site for the 1700 event. 56 cores located along the tidal flat of the estuary contained identifiable sandy deposits, with an average deposits thickness of 5.5 cm.

Salmon River, OR (Le Selle et al., in Review): With almost 250 total analyzed cores, Salmon River has the most substantial and highest quality dataset for analysis of the 1700 earthquake and tsunami. The Salmon River estuary lowlands covers a region of 8 square kilometers. Compared to its neighboring sites, Salmon River acts as a maximum for coseismic subsidence, with an estimated subsidence of 0.9-1.7 m. Sand deposits associated with the 1700 tsunami are found up to 4.25 km inland, with an average deposit thickness of 2.6 cm and a general thinning landward.

Cannon Beach, OR (Witter, 2008): Like the other sites in Oregon, the Ecola Creek watershed area within Cannon Beach in northern Oregon contains strong evidence and a number of deposits associated with the 1700 tsunami. Deposits in this area record storm surges and tsunami deposits associated to the 1964 Alaskan tsunami and CSZ prehistoric tsunamis. Within the last 1,000 years, 3 distinct severe tsunami inundation events have occurred in addition to the 1964 tsunami inundation. Deposits associated with the 3 paleotsunamis (including the 1700 event) extend 1.4-1.6 km inland where the sand deposits thinned and became texturally finer the farther inland they extend. Near the creek mouth, the 1700 sand deposits are thickest, where some cores have over 10 cm of sand interbedded between peat.

Willapa Bay, WA (Atwater, 1996): Willapa Bay is another historically significant location for this study. Within this area of southern Washington, three key terrestrial constraints for the 1700

event have been observed: ghost forests, deposits associated with coseismic subsidence, and sandy tsunami deposits (Atwater and Yamaguchi, 1991; Atwater, 1996). We note the significance of the ghost forest tree rings, however, we do not specifically use them as a constraint in this study. Within the last 3,500 years, Willapa Bay has recorded 7 events (Atwater and Hemphill-Haley, 1996). Although within Willapa Bay there are several areas with observed tsunami sand deposits within Willapa Bay, we only utilize those found in the tidal wetlands around the Niawiakum River outlet. Sandy deposits are observed several kilometers inland from the bay. Within some of these deposits associated with the 1700 event, 6 sand layers are present, likely the result of several tsunami pulses impacting the area. We note that future studies may benefit from the analysis of sand layers within the deposits to further constrain tsunami inundation models.

Discovery Bay, WA (Garrison-Laney and Miller, 2017): Discovery Bay is the furthest site from the megathrust used here for inundation modeling, located along the northern segment of the Olympic Peninsula situated within the Salish Sea. This section likely experienced little to no coseismic subsidence as a result of a megathrust rupture due to its distance. This site optimally records tsunami deposits as the bay amplifies tsunami waves and contains an abundant sediment supply from adjacent creeks. 9 tsunami sand deposits have been stratigraphically recorded in the last 2,500 years, the most recorded events out of any other Washington site (Williams et al., 2005). From this study, there are 3 cores with precise locations found within the tidal marsh adjacent to the head of the Salmon Creek.

4.2.6 Landscape Reconstruction

Modeling tsunami inundation for recent earthquakes accurately is nontrivial because of the various simplifications and assumptions one must implement. On top of this, there is added complexity when modeling for prehistoric earthquakes due to the uncertainty of how the landscape has evolved through time. There are over 300 years of potential natural and anthropogenic impacts to landscape evolution that have occurred between now and when the last CSZ event ruptured.

We incorporate some simple landscape reconstruction only at Bradley Lake, Oregon and Crescent City, California (Fig. 6). For Bradley Lake, we implement the inferred landscape used by Witter et al. (2012). This model more closely resembles the landscape depicted by the 1925

U.S. Coast and Geodetic Survey "T-Sheets" (Bernstein, 1925), where the lake's outlet was straighter less obstructed by more recently deposited sand dunes. Greater sand dune accumulation across the Oregon coast has been occurring since the early 1900s when exotic plants were introduced to help stabilize the coastal sand dunes (Komar, 1997). We also edited the DEM for Crescent City by removing the man-made jetties from Crescent Harbor that would act to impede onshore tsunami propagation. The Elk Creek site in Crescent City has likely experienced extensive anthropogenic alterations including deforesting, dredging, and filling. However, the low and broad nature of the valley itself is still dominantly consistent with what was likely present in 1700 (Hemphill-Haley et al., 2019). Since our inundation models are run using a bare Earth approach, any vegetation change would not affect the results of this site.

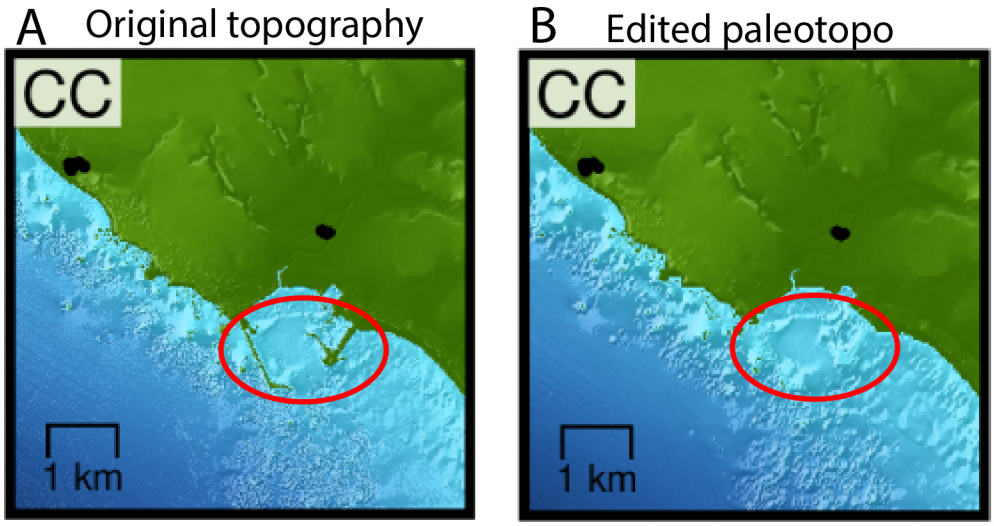

Figure 6: Example simple landscape reconstruction for Crescent City, CA. (A) Original 1/3 arcsecond topography for the region with respect to the NAVD88 vertical datum. (B) Edited landscape reconstruction for the same region where the manmade offshore features are removed (areas within the red outlined region).

Although we do not incorporate other efforts of landscape reconstruction at other sites, we tested the impact of possible landscape variations at both Alsea Bay and Salmon River, Oregon as well. Similar to the method at Bradley Lake, we produce simple landscape reconstructions for these sites based off the "T-Sheets" at both. At these sites, however, the tidal channels and dune

configurations appear relatively stable and unchanged in the last 100 years. Some progradation of the coast has occurred at both sites, however, when we removed this from the landscape and ran inundation at both sites at the highest tide and low tide, this did not produce any effect on the resultant inundation percentages. So, we kept the landscapes unedited for the rest of the study.

4.3 Results

4.3.1 Full Margin Ruptures

The simplest hypothesis is that the CSZ last ruptured in a full margin event. Of the initial 37,500 ruptures, 28 ruptures fit the coastal subsidence across the subduction with a weighted root mean square error (WRMSE) > 0.6 m and match the tsunami heights in Japan. To add the inundation modeling as a constraint, we specify that a rupture must inundate at least 6 of the 7 sites with inundation percentage at each site greater than 70%, and partial inundation at the last site. Because of the tight time constraint of the 26 January 1700 event, we model tsunami propagation and inundation during the 0.3 m tide stage, matching the hindcast average for the region (Mofjeld et al., 1997). We define "inundation" as the tsunami reaching a minimum onshore flow depth threshold of 0.5 m for each survey point. This threshold for inundation is based on studies on sediment transport that show flow-depths beneath this threshold are unlikely to result in deposition of sediment transported by a tsunami (Kench et al., 2008; Goto et al., 2014; Apotsos et al., 2011).

Based on these conditions, of the 28 ruptures that fit the subsidence and the tsunami in Japan, only 7 also fit the inundation criteria (Fig. 7). These events have a range of WRMSE for coastal subsidence from 0.29-0.47 m, which is far lower than our threshold of 0.6 m. Only one rupture, which we consider the "preferred" full margin rupture (Fig. 1A), produces inundation at all 7 sites, with the lowest percent of inundation of 85% at Alsea Bay. The rest of the ruptures can only partially inundate Alsea Bay, with most unable to inundate greater than 50% at this site.

All 7 ruptures have similarities in their slip patterns (Fig. 8), specifically the locations and amplitudes of dominant slip patches. These 7 ruptures are full "wall-to-wall" events, producing slip across the entire megathrust. They all have large, shallow slip (~20m) occurring across much of the margin. Similarly, they all experience slip to the trench and except for one rupture, the peak slip values occur at the trench (Fig. 8). Lastly, slip is concentrated almost entirely offshore,

with only some slip occurring up to 30 km depth beneath the Olympic Peninsula and parts of central Oregon (~44-45° N).

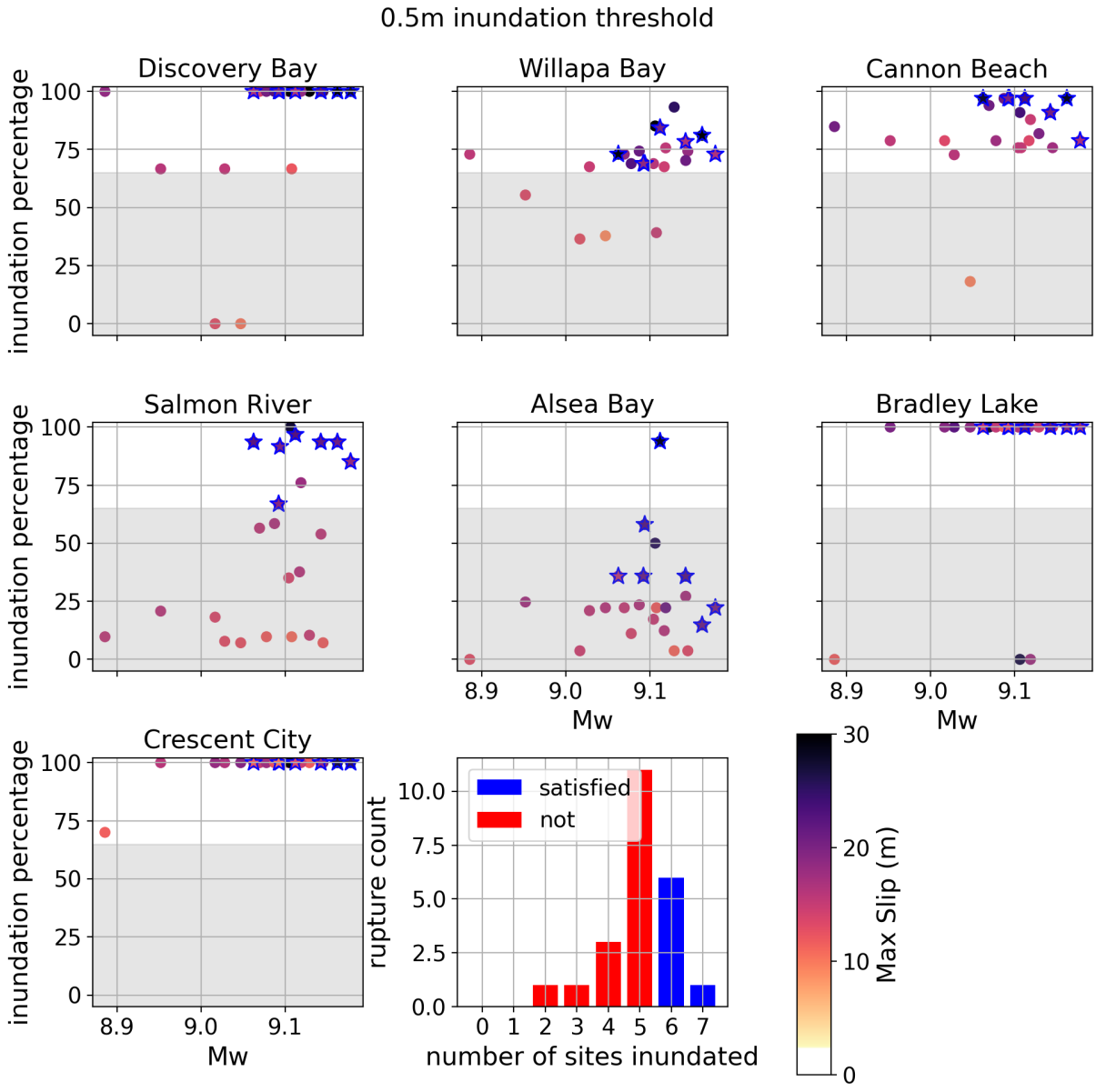

Figure 7: Inundation percentage for the 28 full margin ruptures at each of the 7 coastal sites. Ruptures that inundate at least 6 sites over the 70% threshold are depicted as stars. The plot colormap is based off the maximum slip recorded for a rupture within 0.5° latitude of the specific site.

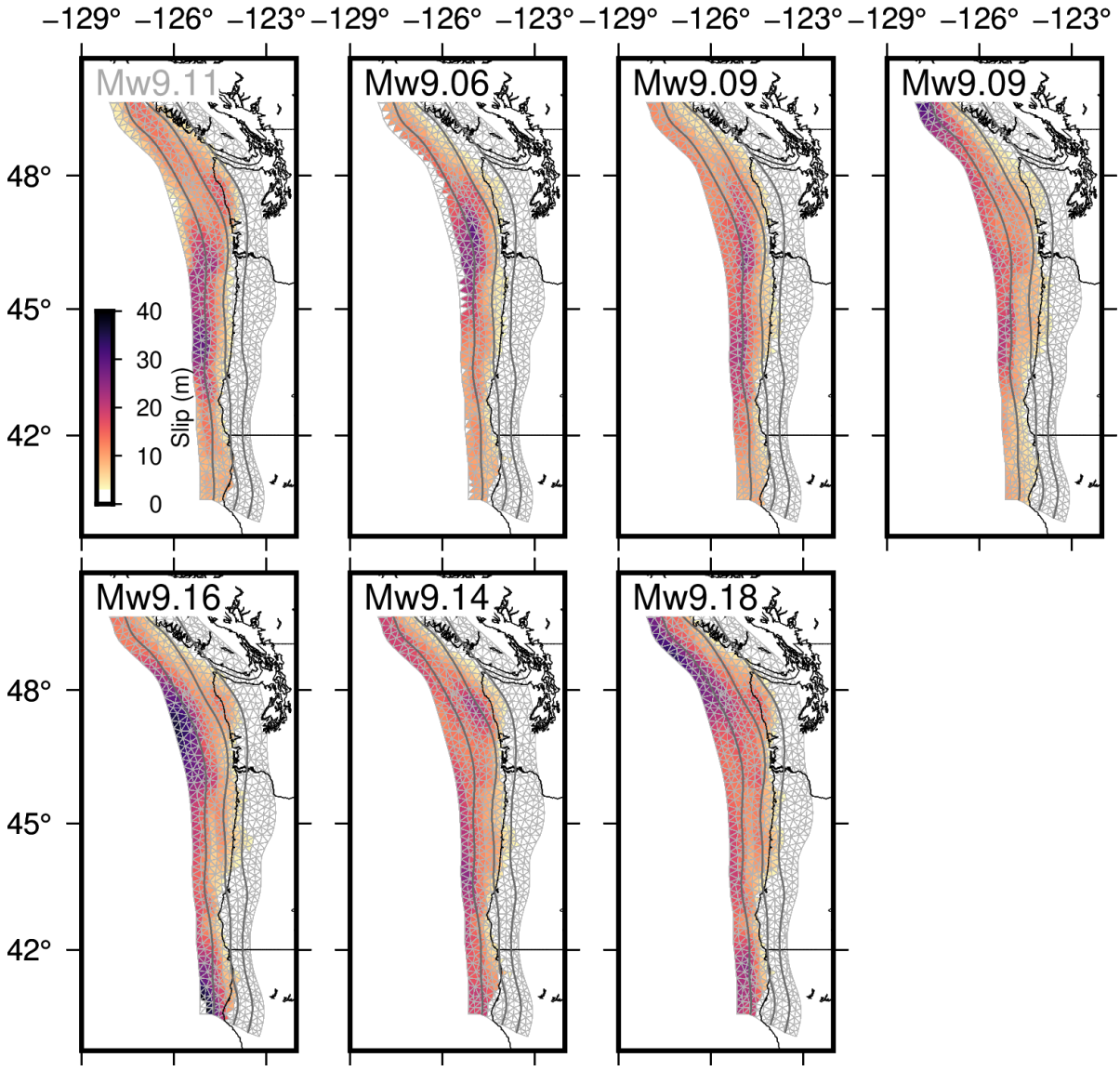

Figure 8: 7 Possible 1700 full margin ruptures that fit all three paleoseismic proxies. The first rupture is the only one that can inundate all 7 sites over the threshold. The other 6 ruptures inundate 6 of the 7 sites over the threshold, with Alsea Bay only partially inundated.

We calculate the median slip on each subfault that result from these 7 ruptures (Fig. 9A) and its interquartile range (Fig. 9B). This conveys a sense of the average slip needed to explain all three proxies and a measure its uncertainties. There is a tight range of magnitudes, with a median magnitude of Mw 9.11, a minimum of Mw 9.06, and a maximum of Mw 9.18. The maximum slip observed in the median slip model is 25 m, with over 15 m of slip experienced throughout much of the megathrust. The region of greatest slip occurs off the coast of Oregon, between

Salmon River to the north and Bradley Lake to the south. The interquartile range is consistently low (below 10 m) between 42 – 47° N and high (up to 15 m) towards the edges of the slab. Based on the median model and the IQR of it, the highest slip and most coherent signal of slip occurs off the coast of central Oregon (~44° N). This is unsurprising as the edges of the megathrust are constrained by fewer observations.

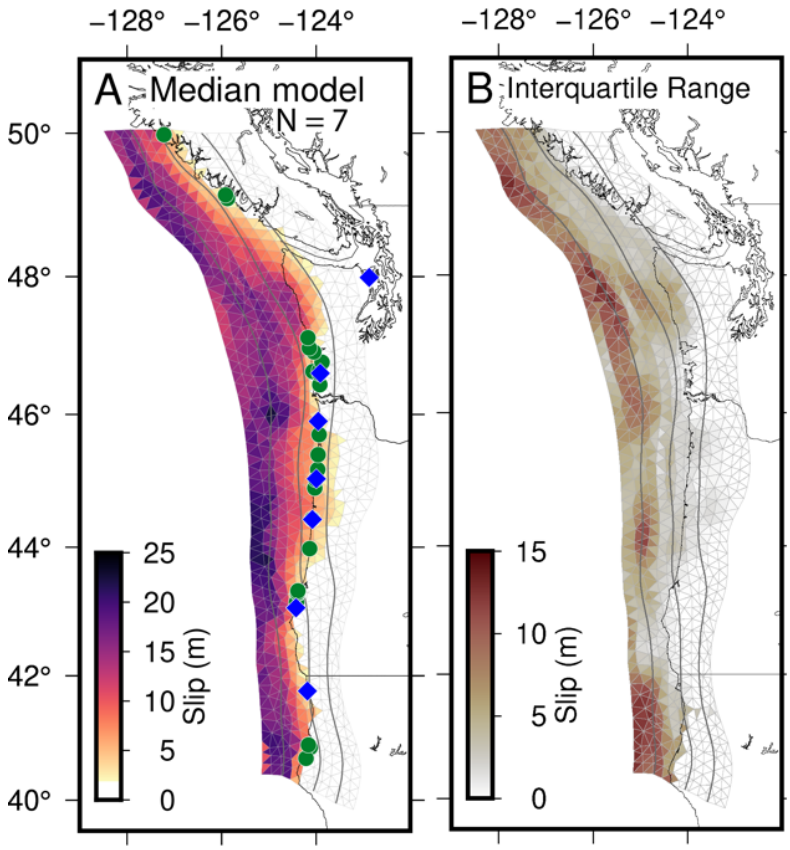

Figure 9: Median slip distribution and IQR. (A) Median slip model based on the 7 full margin ruptures that fit all 3 proxies. Green and blue points are the subsidence sites and inundation sites used in the study. (B) Interquartile range model.

4.3.2 Rupture Sequences

We now relax the previous assumption that all proxies must be attributed to the same earthquake and allow for smaller partial ruptures to be combined in sequences. Here, no one rupture needs to reproduce all the necessary geologic observations, but instead, the summation of the results of all the ruptures for a given sequence must fit them. For a sequence to be viable,

first, all ruptures must collectively reproduce the coastal subsidence at all sites with a WRMSE < 0.4 m. We recognize the differing cutoff of WRMSE between the two paths; however, due to the costly nature of determining sequences and that adequate full margin ruptures had an WRMSE comparable to 0.4 m, we utilize a lower threshold here. Second, only one rupture in the sequence should produce inferred tsunami heights in Japan while the other rupture must produce amplitudes in Japan smaller than 30 cm. Third, ruptures within the sequence cannot re-rupture more than 10% of a part of the megathrust that participated in another event. Lastly, the tsunamis resulting from a sequence must inundate at least 6 of the 7 sites at a minimum level of 70%. To our knowledge, field observations find no evidence of "stacked" deposits reflective of multiple instances of distinct tsunami sands matching the age constraint. Thus, we do not permit duplicate inundation at sites consisting of more than 15% of the deposits.

From the initial catalog of 37,500 ruptures, only 2,000 are partial margin ruptures that can duplicate local coastal subsidence within the specified error margins. Of these, 71 can reproduce the tsunami heights in Japan, while 700 produce heights below 30 cm. Those 71 ruptures are then considered the candidate mainshock events that would have ruptured on 26 January 1700. The other 700 ruptures can then be fore/aftershocks associated with the sequence. There are a multiple rupture sequences that can fit all proxies given our criteria. Notably, no 2 rupture sequences fit our criteria – only sequences of 3 and 4 ruptures can match the observations, with 418 unique sequences of 3 ruptures (Fig. 10) and 26,402 sequences of 4 ruptures. An example rupture sequence is shown in Fig. 12. Most sequences cannot produce adequate subsidence at all sites, however, a select few of 25 sequences of 3 and 650 sequences of 4 ruptures can fit all sites.

Of the initial 71 mainshock ruptures that can produce the tsunami heights needed in Japan, only 5 of these can be used to make sequences (Fig. 11). Three of these events occur in southern Cascadia, rupturing up to 44° N, the other two have slip past this. Some patterns are present between sequences. What we define as group 1 sequences experience a large mainshock (Mw 9.03) event rupturing the northern and central segments of the megathrust (Fig. 10A). Meanwhile group 2 sequences have a smaller mainshock (Mw 8.67-8.87) confined to the southernmost segment of the megathrust. For simplicity, we only present analysis of the sequences of 3 events, however, the trends are similar for sequences of 4.

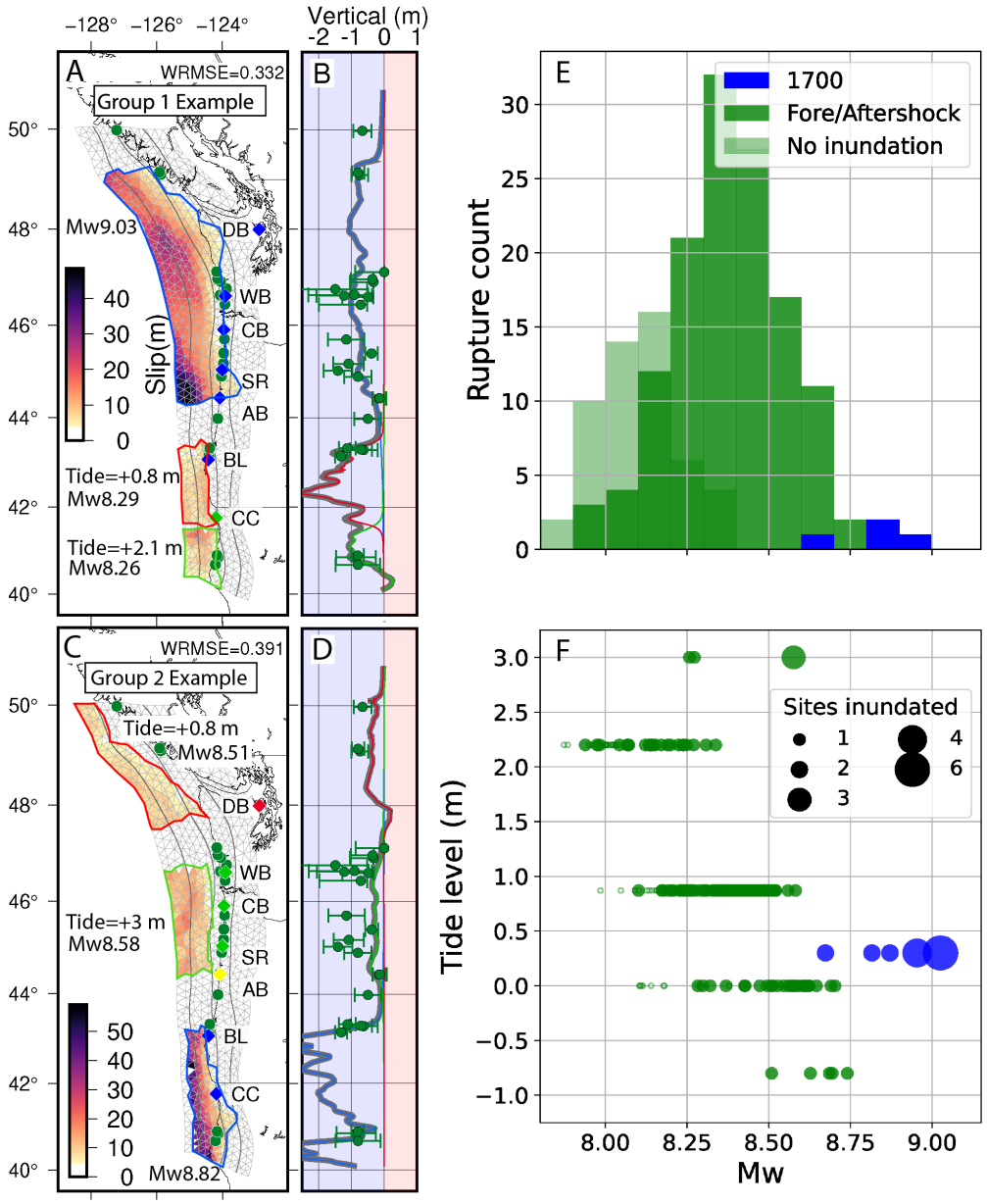

Figure 10: Example sequences of 3 ruptures and the distributions of Mw and tide levels for all 418 sequences. (A) Group 1 example sequence slip distribution with the mainshock rupture outlined in blue and the secondary fore/aftershock ruptures in red and green. The inundation sites depicted as diamonds are colored corresponding to the rupture that inundates them. If a site is not inundated, the point is depicted in yellow. The tide levels required for each of the secondary ruptures is expressed next to the ruptures. The mainshock event always occurs at 0.3 m above NAVD88 vertical datum. (B) Coastal deformation for the group 1 example sequence. The total deformation signal is shown in gray, whereas the deformation from each of the ruptures are shown in their outline colors: blue, green, and red. (C) Group 2 example sequence slip

distribution. (D) Coastal deformation for the group 2 example sequence. (E) Histogram of all ruptures used in sequences of 3 ruptures. Histograms are broken up into 3 categories. Mainshock events are in blue. Fore/aftershocks are in green and separated into two groups: those that produce inundation at one or more site, and those that do not produce any inundations and only contribute to the final coastal subsidence signal. (F) Scatter of all ruptures in sequences of 3 based on their magnitude and the highest tide stage required for sequencing to be possible. Each point represents an individual rupture with the size of the point correlated to the number of sites that rupture's resultant tsunami inundates. Small, empty points represent ruptures that do not produce any inundations.

Only ruptures in group 1 can inundate all 7 coastal sites (Fig. 10A & 12). These sequences require one Mw 9.03 mainshock event and a smaller Mw 8.26 event located near the southern boundary of the megathrust. The mainshock event has a peak slip of almost 50 m centered at the southern edge of the rupture area offshore central Oregon. Because of the ideal location of the peak slip, this rupture can inundate both Salmon River and Alsea Bay above the threshold, making it the only partial margin rupture able to do so. This event produces a tsunami large enough to fully inundate all sites except Crescent City. Typically, to inundate Bradley Lake, almost 15 m of slip is required directly offshore. While the rupture edge is over 150km from the site, the extreme amplitude of slip focused on the rupture's southern terminus is enough to breach the lake. Additionally, the smaller fore/aftershock required in these sequences must occur in the southernmost segment of the megathrust, creating the inundation at Crescent City (Fig. 12). While this rupture appears very small by comparison, it is the only one in this region that could produce the necessary subsidence and inundation at CC that does not also inundate sites previously wetted by other events. To produce the necessary inundation, this small rupture must occur when tide levels match or exceed MHHW. The last rupture within these sequences occurs directly offshore Bradley Lake (42-44° N), but because it is smaller (median Mw 8.14) or occurs during lower tidal levels, it only contributes to local coastal subsidence without adding any inundation signal. Overall, sequences within this group can reproduce the 3 paleoseismic proxies.

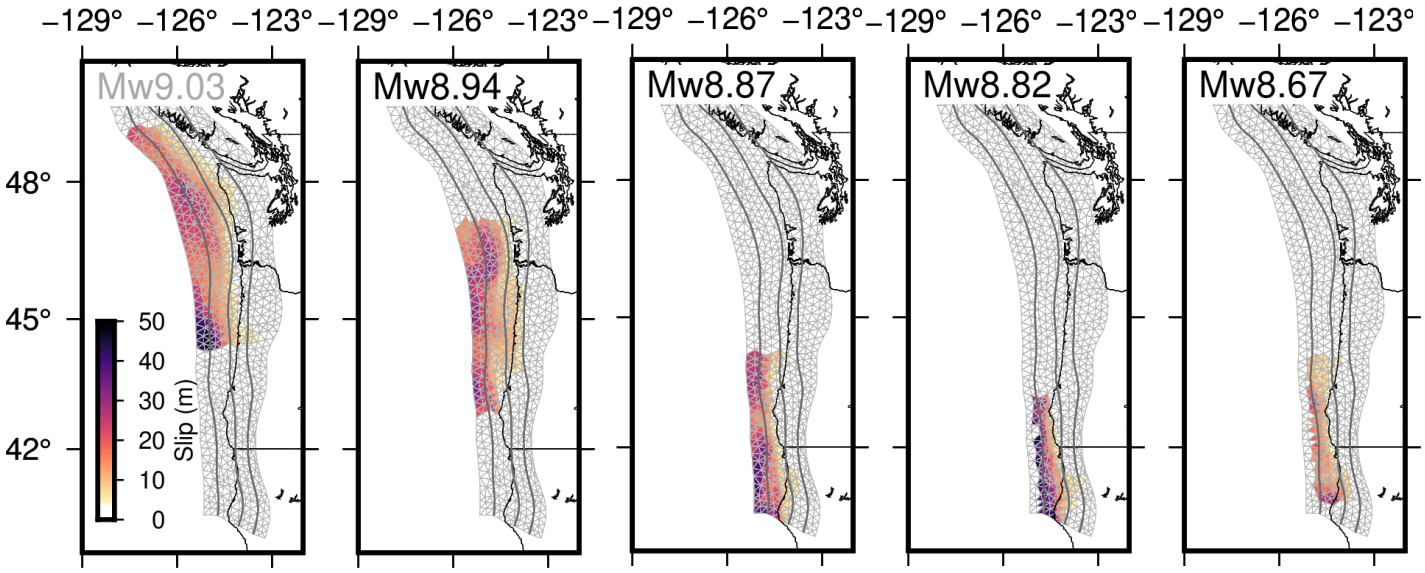

Figure 11: Mainshock ruptures for the sequences of 3 and 4 ruptures. The first rupture is the only one that can produce sequences that inundate all 7 coastal sites with an inundation percentage greater than 70%.

The next family of sequences, group 2, has 63% of all possible sequences of 3 ruptures and is defined by the presence of a southern Cascadia mainshock (40-44° N) (Fig. 10C). There are three possible mainshock events in group 2 (Fig. 11). Noticeably, these ruptures are smaller than the other possible mainshock events located further north because less slip is required to produce a tsunami to Japan when slip is focused in the southern portion compared to further north. Sequences in this group generally have similar magnitude ranges between mainshock events are the secondary ruptures, where the fore/aftershocks have a median Mw 8.4. These sequences are dependent on a single central Cascadia secondary rupture to produce the inundations needed from Alsea Bay to Willapa Bay. Even at the highest tide stage of +3 m, Alsea Bay could not be inundated above the minimum threshold. While technically under the WRMSE subsidence threshold, these sequences consistently underfit the central and northern Oregon geologic conditions (Fig. 10D).

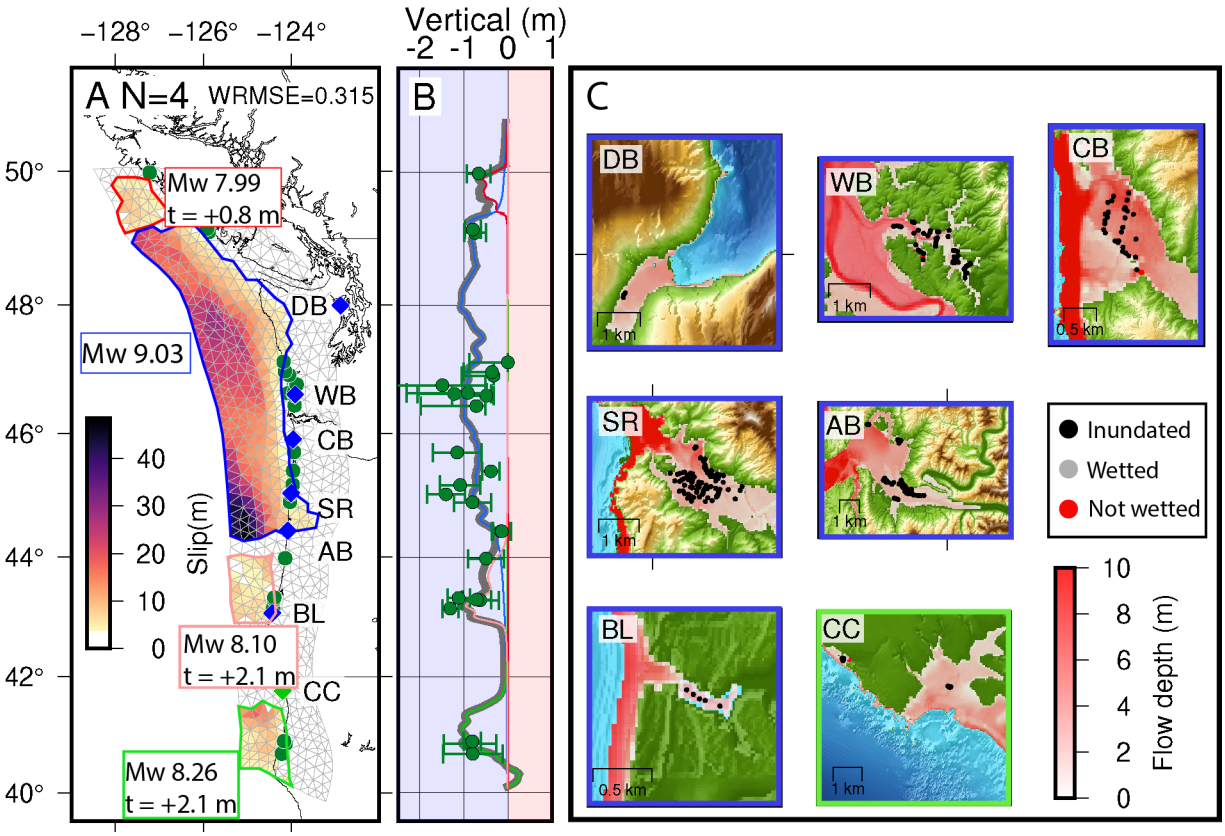

Figure 12: Example sequence of 4 ruptures that fits all 3 paleoseismic constraints. (A) Slip model composed of 4 distinct ruptures. Each individual rupture is highlighted by unique colors that match their coastal deformation signal in the adjacent panel. The rupture in blue is the mainshock event that produces the tsunami in Japan. Diamonds depict the inundation sites and their respective colors match the rupture that produces their inundations. (B) Coastal deformation for the slip model in (A). Coastal subsidence for this event fits with a WRMSE of 0.32 m. (C) 7 coastal sites with recorded paleotsunami sand deposits and the maximum inundation flow depth for the model in (A). Points depict locations of sand deposits where the colors black, gray, and red express deposits with flow depth exceeding the depth threshold of 0.5 m, flow depth below the threshold but still wetted, and no flow recorded, respectively.

4.4 Discussion

Of our initial catalog of 37,500 unique ruptures, only 7 “wall-to-wall” events could qualify as likely slip distributions for the 1700 event. When considering sequences of closely timed events, sequences of 3 and 4 ruptures were able to satisfy the constraints as well. Since both modes of failure can satisfy the paleoseismic proxies within the thresholds we set, we cannot

fully rule out either mode of megathrust behavior. However, based on the specific conditions required to produce adequate inundations with partial margin ruptures, we think that Cascadia last failed in a single event is more likely than in a sequence of closely timed events. For any sequence to fit the proxies, realistic but high tide conditions are required for adequate inundation. Additionally, over half of the adequate sequences produced in this study reproduce the 3 proxies with less than favorable results. The dependence of group 2 sequences to the single central Cascadia rupture that underfits almost all Oregon subsidence sites and inadequately inundates Alsea Bay makes these sequences less favorable when compared to the full margin ruptures.

4.4.1 Inundation Site Importance

The importance and impact of the inundation sites is not uniform between sites and mode of failure assumptions. Not all sites used in this study have equal value for constraining slip patterns. Willapa Bay, Salmon River, and Alsea Bay (Fig. 7) have the greatest quantity of identified tsunami deposits; they also have significant topographical complexity which makes widespread inundation difficult at times. Alsea Bay is the most challenging to fully inundate, with only one full margin event inundating this site over the minimum threshold (Fig. 1C). Part of the challenge at this site is that the region where deposits are seen is expansive, covering ~24 km^2. Salmon River shows the clearest example of minimum offshore slip dependence where at least 18 m of slip is routinely needed to adequately inundate. This is comparable but slightly higher than the minimum slip requirement from a single-site study using more complex sediment transport models (La Selle et al., in Review).

Conversely, some sites are almost always inundated by the 28 candidate full-margin rupture models, making them less sensitive to constraining details of the necessary slip. Due to the culling efforts from the first two paleoseismic proxies (the subsidence estimates and the Japan tsunami), the remaining full margin ruptures all have relatively high slip values. A study of inundation modeling at Bradley Lake determined a minimum slip threshold of > 14 m of in southern was necessary for that site (Witter et al., 2012). Because the 28 full margin ruptures are always above this threshold (Fig. 7), this site proves less impactful. Nonetheless, Bradley Lake provides critical constraints when testing rupture sequences.

Unlike the full margin ruptures, for sequences, Bradley Lake becomes a much greater control for adequacy of sequences. Bradley Lake is only inundated by partial margin ruptures

that can also produce the necessary tsunami heights in Japan. Even during the highest tide stage (+3 m), Bradley Lake cannot be inundated by any fore/aftershock rupture. This is also the case for Alsea Bay, where only the mainshock event from group 1 can inundate this site. Additionally, Crescent City plays a fundamental role due to the limited number of ruptures in southern Cascadia (below 44° N) that can fit the subsidence data. Only 22 fore/aftershock ruptures with slip directly offshore Crescent City were used for sequences; however, only one of these ruptures could adequately inundate this site. It is important to note that regardless of assumption of failure, sites with a greater number of tsunami deposits generally require more specific rupture conditions.

4.4.2 Slip Comparison to Previously Published Models

We compare the locations and amplitude of large slip patches in our median full margin slip distribution to those from Wang et al. (2013) and notice similarities in asperity locations. The model from Wang et al. has 4 very distinct slip patches, with the widest occurring offshore Washington and the one with greatest amplitude of slip occurring around 43-44° N. While our median slip model has more large, distributed slip, the general locations of dominant slip patches are quite similar, especially the location of the highest amplitude slip patch (Fig. 9A). Most notable, however, we see peak slip of 29 m, almost 10 m greater than theirs. This increase in slip is also present when we instead compare our models to earlier ones as well. For instance, when compared to the "T-shirt" scenarios (Witter et al., 2011), the large category ruptures best fit our proposed models both in slip range and event magnitude. Contrary to our results, it was previously thought that the 1700 event more closely resembles a medium sized "T-shirt". Similarly, the nearest resembling model constrained by the Japan tsunami heights from Satake et al., 2003 experiences an average slip of 20 m across the megathrust, which still underfits the slip we require by 9 m. Our candidate ruptures are generally more complex than previous models, with slip heterogeneity that is more similar to what is expected in large subduction zone earthquakes (Small and Melgar, 2021). These models experience more downdip slip underneath the Olympic peninsula around 47° N than other studies propose, however, since onshore observations are sparse in this region, this is somewhat unconstrained. Overall, our candidate full margin events appear more heterogeneous and with greater amplitudes of slip than what has

often been considered. This likely is the result of complexity of our slip assumptions, along with the addition of the inundation metric for constraining rupture scenarios.

4.4.3 Implications for Future Hazards

Understanding the characteristics of the earthquake cycle is fundamental for our understanding of the full suite of possible future ruptures. While either mode of failure would cause detrimental impact to the region, whether the CSZ will rupture in a full margin Mw 9 event compared to a sequence of Mw 8 events will have a large impact on how hazards are quantified. If we can use the same techniques here to study earthquakes prior to the 1700 event and can constrain slip distributions for those events, we can gain insight into patterns of failure and how Cascadia could rupture next. Unfortunately, incorporating these methods to study older past ruptures becomes increasingly difficult due to the growing uncertainty in past landscapes the further we look. This should not prevent us, however, from attempting to do so.

When considering rupture sequences, there is still quite a variety of possible sequences with varying overall slip patterns. One clear component for increased hazards with sequences is the present gap between rupture areas. Even though we allow for rupture areas to overlap by 10% of their total areas, most sequences experience gaps between ruptures up to 100 km along strike (Fig. 12A). If we assume that sequences are the dominant behavior, then the gaps present within our potential sequences (e.g., Fig. 12A), would likely not have slipped since the penultimate earthquake, increasing the available slip budget for a future earthquake.

Based on the turbidite record mentioned prior, the Cascadia subduction zone is thought to have ruptured in 19 full margin events in the last 10,000 years, with a range of time intervals between events from ~110 to 1150 years (Goldfinger et al., 2012). The penultimate full margin event is thought to have occurred 800 BP (Nelson et al., 2021). We can perform a rough calculation to determine the amount of time needed to produce a slip budget seen in our median slip distribution through dividing the slip pattern by various proposed slip deficit rate (SDR) models for the CSZ (Schmalzle et al., 2014; Li et al., 2018). By doing this, we are assuming that the pattern of coupling has not changed substantially in the last 800 years.

In Fig. 13, we compute how many years are needed to produce the slip budget for the median slip model under different assumptions of megathrust coupling. If we assume a SDR model with high coupling near the trench as in the gamma and Li models, most of the slip produced by the median slip model accumulated around 500 +/- 100 years (Fig. 13D and 13F). This matches quite well with the time interval between the last two events (Nelson et al., 2021). If we assume a coupling model with shallow creeping instead, the slip budget requires a much greater amount of time for accumulation, with the shallowest regions requiring almost 5,000 years of accumulation (Fig. 13E). When we consider the Li or the Gamma coupling models, the majority of the slip budget accumulated between the last two events has been depleted. However, the shallow regions off the Olympic Peninsula did not slip in the full available slip budget, with an excess of over 5 m of slip left over for a future event based on either the gamma or the Li coupling models.

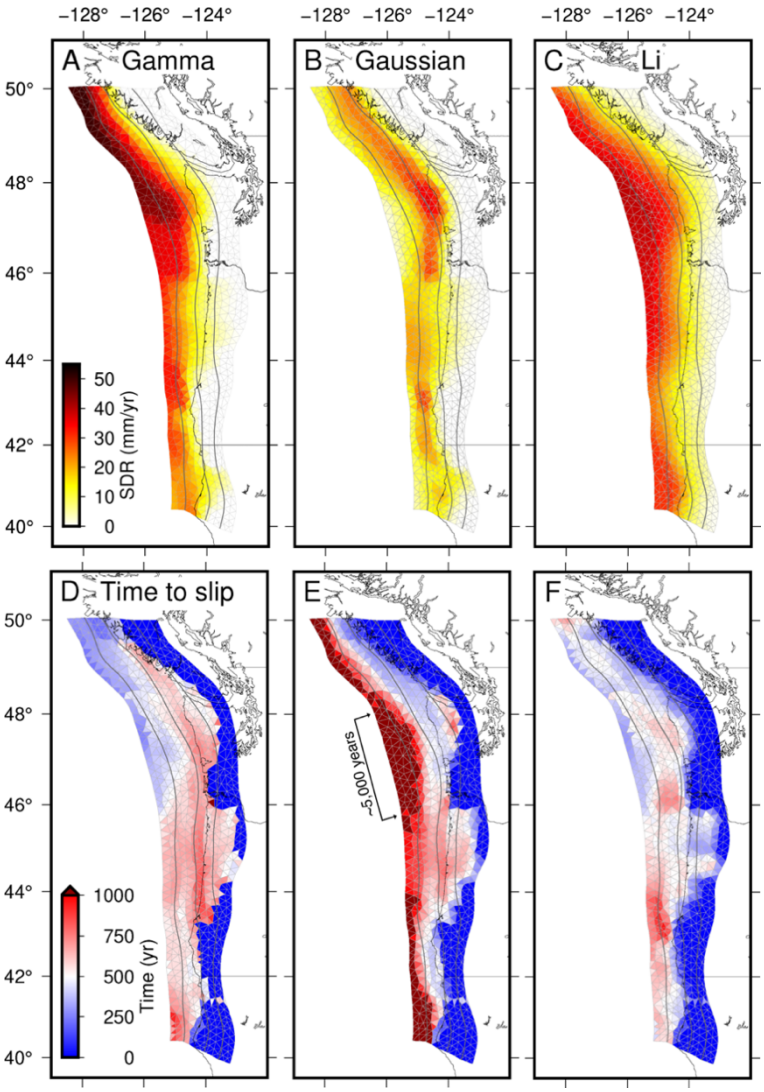

Figure 13: Time needed for slip accumulation based on SDR models. (A-C) Slip deficit rate (SDR) models for the CSZ. (A) SDR model where full geodetic coupling is assumed at the trench and decays downdip based off of a gamma function from. (B) SDR model where instead the trench is assumed to be creeping and the pattern of coupling is fit with a gaussian distribution. The first two SDR models are from Schmalzle et al. (2014). (C) SDR model from Li et al. (2018) where the trench is fully coupled. (D-F) Time to slip budget models calculated from the median full margin slip distribution. Time is determined by dividing the SDR by the slip at each subfault. Each time to slip model corresponds with the model above, so (D) is determined from the gamma coupling model (E) is from the gaussian coupling model, and (F) is from the Li coupling model. The colormaps are saturated at 1,000 years, so any subfault with time to slip greater than 1,000 years is saturated to the deep red color. The colormap diverges at 500 years since that is the amount of time between Cascadia 1700 event and the penultimate full margin event.

4.5 Conclusion

It is not debated that there was a large megathrust rupture on the Cascadia subduction zone on 26 January 1700. Various models for this failure have been considered – a Mw 9+ "wall to wall" rupture or a sequence of closely timed partial margin ruptures – and assessed on their viability based predominantly on analysis of their coastal deformation (Leonard et al., 2004, 2010; Wang et al., 2013), or their ability to produce a tsunami in Japan (Satake et al., 2022), or both (Melgar, 2021). Our study, however, is the first to use inundation modeling at multiple sites across the Pacific Northwest in addition to those two constraints.

By considering the three paleoseismic proxies, we find 7 full margin ruptures of an initial catalog of 37,500 unique slip distributions that fit the constraints. These 7 ruptures have consistent slip patterns between one another, with variability mostly confined to the edges of the megathrust (Fig. 9B). These models can near fully inundate 6 of the coastal sites, but only one rupture can inundate all 7 sites above the 70% inundation threshold (Fig. 1). While there is low IQR for all 7 events, we consider the one that inundates all 7 sites the "preferred model". Under the specific requirements for consideration, we can fit all paleoseismic proxies with sequences of 3 and 4 ruptures. These can be grouped into several families with similar trends, however, only one group of 25 sequences of 3 and 650 sequences of 4 can produce inundation at all 7 sites (Fig. 12A). These preferred sequences are dependent on high tide conditions to aid full inundation.

Our favored full margin ruptures experience almost 10 m of additional slip than some previously considered models (e.g., Wang et al., 2013). Along some sections of the CSZ, incorporating the minimum inundation marked by tsunami deposits as a constraint on rupture models increases predicted slip when compared to using subsidence data alone. This necessity for increased slip and difficulty inundating all sites and deposits could, however, indicate where more complex tsunami sources may need to be invoked. We note here that we do not use the presence and absence of tsunami sand deposits provided by some studies (e.g., Witter, 2008) as constraints for inundation area, but rather, the presence of sand deposits generally provides a minimum estimate of tsunami inundation. With a greater understanding of the relationship between topography, sand deposition, and inland inundation extent, future work could expand upon this work to utilize the presence/absence of sand as further constraints.

Regardless of the assumed hypothesis for the mode of failure, various simplifications and conditions neglected in this study may be useful for future studies. For example, slip could extend onto splay faults during one of the ruptures which could have increase tsunami heights and therefore inundation at some sites like Alsea Bay (e.g., van Zelst et al., 2022). Splays have been identified throughout the CSZ (e.g., Han et al., 2017), and many have been considered active in the recent megathrust events. Which ones, and how many (if any), contributed to the 1700 event is difficult to say. So, we recognize they may contribute to our results, however, we neglect them based on their uncertainties. Similarly, we assume that all surface deformation recorded by the paleoseismic proxies is coseismic and therefore neglect any influence from post-seismic relaxation or afterslip. While this would likely not influence the inundation results, it could lead to an overestimation of coastal deformation in some regions (Atwater and Hemphill-Haley, 1997). Post-seismic deformation has been observed at various recent megathrust events like 2010 Maule Mw 8.8 (Bedford et al., 2013), making it likely to have some influence on the final observed subsidence associated to the 1700 event. Though these sources of error may impact our results, their inclusion is non-trivial and would require further nuances and assumptions into the study. Still, we determine a select few heterogeneous ruptures that might be the last great Cascadia earthquake.

References Cited

Apotsos, A., Buckley, M., Gelfenbaum, G., Jaffe, B., & Vatvani, D. (2011). Nearshore tsunami inundation model validation: toward sediment transport applications. *Pure and Applied Geophysics*, *168*, 2097-2119.

Atwater, B. F. (1996). Coastal evidence for great earthquakes in western Washington. *Assessing earthquake hazards and reducing risk in the Pacific Northwest*, *1*, 77.

Atwater, B. F., & Hemphill-Haley, E. (1996). *Preliminary estimates of recurrence intervals for great earthquakes of the past 3500 years at northeastern Willapa Bay, Washington* (Vol. 96). US Department of the Interior, US Geological Survey.

Atwater, B. F., & Hemphill-Haley, E. (1997). *Recurrence intervals for great earthquakes of the past 3,500 years at northeastern Willapa Bay, Washington* (No. 1576). US Government Printing Office.

Atwater, B. F., Carson, B., Griggs, G. B., Johnson, H. P., & Salmi, M. S. (2014). Rethinking turbidite paleoseismology along the Cascadia subduction zone. *Geology*, *42*(9), 827-830.

Atwater, B. F., & Yamaguchi, D. K. (1991). Sudden, probably coseismic submergence of Holocene trees and grass in coastal Washington State. *Geology*, *19*(7), 706-709.

Barnhart, W. D., Murray, J. R., Briggs, R. W., Gomez, F., Miles, C. P., Svarc, J., ... & Stressler, B. J. (2016). Coseismic slip and early afterslip of the 2015 Illapel, Chile, earthquake: Implications for frictional heterogeneity and coastal uplift. *Journal of Geophysical Research: Solid Earth*, *121*(8), 6172-6191.

Bartlow, N. M. (2019). A long-term view of episodic tremor and slip in Cascadia. *Geophysical Research Letters*, **47**(3), e2019GL085303.

Blaser, L., Krüger, F., Ohrnberger, M., & Scherbaum, F. (2010). Scaling relations of earthquake source parameter estimates with special focus on subduction environment. *Bulletin of the Seismological Society of America*, *100*(6), 2914-2926.

Bletery, Q., Thomas, A. M., Rempel, A. W., Karlstrom, L., Sladen, A., & De Barros, L. (2016). Mega-earthquakes rupture flat megathrusts. *Science*, *354*(6315), 1027-1031.

Bedford, J., Moreno, M., Baez, J. C., Lange, D., Tilmann, F., Rosenau, M., ... & Vigny, C. (2013). A high-resolution, time-variable afterslip model for the 2010 Maule Mw= 8.8, Chile megathrust earthquake. *Earth and Planetary Science Letters*, *383*, 26-36.

Comninou, M., & Dundurs, J. (1975). The angular dislocation in a half space. *Journal of Elasticity*, *5*, 203-216.

Frankel, A., Chen, R., Petersen, M., Moschetti, M., & Sherrod, B. (2015). 2014 update of the Pacific Northwest portion of the US National Seismic Hazard Maps. Earthquake Spectra, 31(1_suppl), S131-S14

Garrison-Laney, C., & Miller, I. (2017). Tsunamis in the Salish Sea: Recurrence, sources, hazards.

Goda, K., Yasuda, T., Mori, N., & Maruyama, T. (2016). New scaling relationships of earthquake source parameters for stochastic tsunami simulation. Coastal Engineering Journal, 58(3), 1650010-1.

Goldfinger, C., Nelson, C. H., Morey, A. E., Johnson, J. E., Patton, J. R., Karabanov, EI., ... & Vallier, T. (2012). *Turbidite event history—Methods and implications for Holocene paleoseismicity of the Cascadia subduction zone* (No. 1661-F). US Geological Survey.

Goto, K., Hashimoto, K., Sugawara, D., Yanagisawa, H., & Abe, T. (2014). Spatial thickness variability of the 2011 Tohoku-oki tsunami deposits along the coastline of Sendai Bay. *Marine Geology*, *358*, 38-48.

Han, S., Bangs, N. L., Carbotte, S. M., Saffer, D. M., & Gibson, J. C. (2017). Links between sediment consolidation and Cascadia megathrust slip behaviour. Nat. Geosci. 10, 954–959.

Hayes, G. P., Moore, G. L., Portner, D. E., Hearne, M., Flamme, H., Furtney, M., & Smoczyk, G. M. (2018). Slab2, a comprehensive subduction zone geometry model. *Science*, *362*(6410), 58-61.

Hawkes, A. D., Horton, B. P., Nelson, A. R., Vane, C. H., & Sawai, Y. (2011). Coastal subsidence in Oregon, USA, during the giant Cascadia earthquake of AD 1700. *Quaternary Science Reviews*, *30*(3-4), 364-376.

Hemphill-Haley, E., Kelsey, H. M., Graehl, N., Casso, M., Caldwell, D., LoofbourI, C., ... & Southwick, E. (2019). Recent sandy deposits at five northern California coastal wetlands-stratigraphy, diatoms, and implications for storm and tsunami hazards. *Scientific Investigations Report-US Geological Survey*, (2018-5111).

Hill, J. C., Watt, J. T., & Brothers, D. S. (2022). Mass wasting along the Cascadia subduction zone: Implications for abyssal turbidite sources and the earthquake record. *Earth and Planetary Science Letters*, *597*, 117797.

Howarth, J. D., Orpin, A. R., Kaneko, Y., Strachan, L. J., Nodder, S. D., MountI, J. J., ... & Cağatay, M. N. (2021). Calibrating the marine turbidite palaeoseismometer using the 2016 Kaikōura earthquake. *Nature Geoscience*, *14*(3), 161-167.

Kelsey, H. M., Nelson, A. R., Hemphill-Haley, E., & Witter, R. C. (2005). Tsunami history of an Oregon coastal lake reveals a 4600 yr record of great earthquakes on the Cascadia subduction zone. *Geological Society of America Bulletin*, *117*(7-8), 1009-1032.

Kemp, A. C., Cahill, N., Engelhart, S. E., Hawkes, A. D., & Wang, K. (2018). Revising estimates of spatially variable subsidence during the AD 1700 Cascadia earthquake using a Bayesian foraminiferal transfer function. *Bulletin of the Seismological Society of America*, *108*(2), 654-673.

Kench, P. S., Nichol, S. L., Smithers, S. G., McLean, R. F., & Brander, R. W. (2008). Tsunami as agents of geomorphic change in mid-ocean reef islands. *Geomorphology*, *95*(3-4), 361-383.

Konca, A. O., Avouac, J. P., Sladen, A., Meltzner, A. J., Sieh, K., Fang, P., ... & Helmberger, D. V. (2008). Partial rupture of a locked patch of the Sumatra megathrust during the 2007 earthquake sequence. *Nature*, *456*(7222), 631-635.

La Selle, S.M., Nelson, A.R., Witter, R.C., Jaffe, B.E., Gelfenbaum, G., Padgett, J.S., 2024, Tsunami deposit data and sediment transport models from the Salmon River estuary, central Oregon: U.S. Geological Survey data release, https://doi.org/10.5066/P9M86S7D.

Leonard, L. J., Currie, C. A., Mazzotti, S., & Hyndman, R. D. (2010). Rupture area and displacement of past Cascadia great earthquakes from coastal coseismic subsidence. *Bulletin*, *122*(11-12), 2079-2096.

Leonard, L. J., Hyndman, R. D., & Mazzotti, S. (2004). Coseismic subsidence in the 1700 great Cascadia earthquake: Coastal estimates versus elastic dislocation models. *Geological Society of America Bulletin*, *116*(5-6), 655-670.

LeVeque, R. J., Waagan, K., González, F. I., Rim, D., & Lin, G. (2017). Generating random earthquake events for probabilistic tsunami hazard assessment. *Global Tsunami Science: Past and Future, Volume I*, 3671-3692.

Li, S., & Freymueller, J. T. (2018). Spatial variation of slip behavior beneath the Alaska Peninsula along Alaska-Aleutian subduction zone. *Geophysical Research Letters*, *45*(8), 3453-3460.

Li, S., Wang, K., Wang, Y., Jiang, Y., & Dosso, S. E. (2018). Geodetically inferred locking state of the Cascadia megathrust based on a viscoelastic Earth model. *Journal of Geophysical Research: Solid Earth*, *123*(9), 8056-8072.

Mai, P. M., & Beroza, G. C. (2002). A spatial random field model to characterize complexity in earthquake slip. *Journal of Geophysical Research: Solid Earth*, *107*(B11), ESE-10.

Melgar, D., & Bock, Y. (2015). Kinematic earthquake source inversion and tsunami runup prediction with regional geophysical data. *Journal of Geophysical Research: Solid Earth*, *120*(5), 3324-3349.

Melgar, D., & Hayes, G. P. (2019). The correlation lengths and hypocentral positions of great earthquakes. *Bulletin of the Seismological Society of America*, *109*(6), 2582-2593.

Melgar, D., Williamson, A. L., & Salazar-Monroy, E. F. (2019). Differences between heterogenous and homogenous slip in regional tsunami hazards modelling. *Geophysical Journal International*, *219*(1), 553-562.

Melgar, D. (2021). Was the January 26th, 1700 Cascadia earthquake part of a rupture sequence?. *Journal of Geophysical Research: Solid Earth*, *126*(10), e2021JB021822.

Melgar, D., Sahakian, V. J., & Thomas, A. M. (2022). Deep coseismic slip in the Cascadia megathrust can be consistent with coastal subsidence. *Geophysical Research Letters*, *49*(3), e2021GL097404.

Mofjeld, H. O., Foreman, M. G., & Ruffman, A. (1997). West Coast tides during Cascadia subduction zone tsunamis. *Geophysical research letters*, *24*(17), 2215-2218.

Moreno, M., Rosenau, M., & Oncken, O. (2010). 2010 Maule earthquake slip correlates with pre-seismic locking of Andean subduction zone. *Nature*, *467*(7312), 198-202.

Nelson, A. R., DuRoss, C. B., Witter, R. C., Kelsey, H. M., Engelhart, S. E.,Ihan, S. A., ... & Padgett, J. S. (2021). A maximum rupture model for the central and southern Cascadia subduction zone—reassessing ages for coastal evidence of megathrust earthquakes and tsunamis. *Quaternary Science Reviews*, *261*, 106922.

Okada, Y. (1985). Surface deformation due to shear and tensile faults in a half-space. *Bulletin of the seismological society of America*, *75*(4), 1135-1154.

Ozawa, S., Nishimura, T., Suito, H., Kobayashi, T., Tobita, M., & Imakiire, T. (2011). Coseismic and postseismic slip of the 2011 magnitude-9 Tohoku-Oki earthquake. *Nature*, *475*(7356), 373-376.

Padgett, J. S., Engelhart, S. E., Kelsey, H. M., Witter, R. C., Cahill, N., & Hemphill-Haley, E. (2021). Timing and amount of southern Cascadia earthquake subsidence over the past 1700 years at northern Humboldt Bay, California, USA. *GSA Bulletin*, *133*(9-10), 2137-2156.

Philibosian, B., & Meltzner, A. J. (2020). Segmentation and supercycles: A catalog of earthquake rupture patterns from the Sumatran Sunda Megathrust and other well-studied faults worldwide. *Quaternary Science Reviews*, *241*, 106390.

Sahakian, V., D. Kilb, J. Gomberg, N. Nieminski, and J. Covault (2024), Submarine avalanche deposits hold clues to past earthquakes, *Eos, 105.*

Satake, K., Shimazaki, K., Tsuji, Y., & Ueda, K. (1996). Time and size of a giant earthquake in Cascadia inferred from Japanese tsunami records of January 1700. *Nature*, *379*(6562), 246-249.

Satake, K., Wang, K., & Atwater, B. F. (2003). Fault slip and seismic moment of the 1700 Cascadia earthquake inferred from Japanese tsunami descriptions. *Journal of Geophysical Research: Solid Earth*, *108*(B11).

Schmalzle, G. M., McCaffrey, R., & Creager, K. C. (2014). Central Cascadia subduction zone creep. *Geochemistry, Geophysics, Geosystems*, *15*(4), 1515-1532.

Shennan, I., Long, A. J., Rutherford, M. M., Green, F. M., Innes, J. B., Lloyd, J. M., ... & Walker, K. J. (1996). Tidal marsh stratigraphy, sea-level change and large earthquakes, I: A 5000 year record in Washington, USA. *Quaternary Science Reviews*, *15*(10), 1023-1059.

Spruell, J. T. (2018). Up-estuary extent and lithologic characteristics of tsunami deposits attributed to the 1700 Cascadia earthquake within Alsea Bay, OR.

Small, D. T., & Melgar, D. (2021). Geodetic coupling models as constraints on stochastic earthquake ruptures: An example application to PTHA in Cascadia. *Journal of Geophysical Research: Solid Earth*, *126*(7), e2020JB021149.

Small, D. T., & Melgar, D. (2023). Can stochastic slip rupture modeling produce realistic M9+ events?. *Journal of Geophysical Research: Solid Earth*, *128*(3), e2022JB025716.

Staisch, L. (2024). Sensitivity Testing of Marine Turbidite Age Estimates along the Cascadia Subduction Zone, Bull. Seismol. Soc. Am. XX,1–15

Tanioka, Y., & Sataka, K. (1996). Fault parameters of the 1896 Sanriku tsunami earthquake estimated from tsunami numerical modeling. *Geophysical research letters*, *23*(13), 1549-1552.

Tozer, B., Sandwell, D. T., Smith, W. H., Olson, C., Beale, J. R., & Wessel, P. (2019). Global bathymetry and topography at 15 arc sec: SRTM15+. *Earth and Space Science*, *6*(10), 1847-1864.

van Zelst, I., Rannabauer, L., Gabriel, A. A., & van Dinther, Y. (2022). Earthquake rupture on multiple splay faults and its effect on tsunamis. *Journal of Geophysical Research: Solid Earth*, *127*(8), e2022JB024300.

Wang, P. L., Engelhart, S. E., Wang, K., Hawkes, A. D., Horton, B. P., Nelson, A. R., & Witter, R. C. (2013). Heterogeneous rupture in the great Cascadia earthquake of 1700 inferred from coastal subsidence estimates. *Journal of Geophysical Research: Solid Earth*, *118*(5), 2460-2473.

Williams, H. F., Hutchinson, I., & Nelson, A. R. (2005). Multiple sources for late-Holocene tsunamis at Discovery Bay, Washington State, USA. *The Holocene*, *15*(1), 60-73.

Witter, R.C., 2008, Prehistoric Cascadia Tsunami Inundation and Runup at Cannon Beach, Oregon: Oregon Department of Geology and Mineral Industries, Open-File Report O-08-XX.

Witter, R. C., Zhang, Y., Wang, K., Goldfinger, C., Priest, G. R., & Allan, J. C. (2012). Coseismic slip on the southern Cascadia megathrust implied by tsunami deposits in an Oregon lake and earthquake-triggered marine turbidites. *Journal of Geophysical Research: Solid Earth*, *117*(B10).

Witter, R. C., Zhang, Y. J., Wang, K., Priest, G. R., Goldfinger,I, Stimely, L., ... & Ferro, P. A. (2013). Simulated tsunami inundation for a range of Cascadia megathrust earthquake scenarios at Bandon, Oregon, USA. *Geosphere*, *9*(6), 1783-1803.

Yamaguchi, D. K., Atwater, B. F., Bunker, D. E., Benson, B. E., & Reid, M. S. (1997). Tree-ring dating the 1700 Cascadia earthquake. *Nature*, *389*(6654), 922-923.

Zhang, Y. J., Witter, R. C., & Priest, G. R. (2011). Tsunami–tide interaction in 1964 Prince William Sound tsunami. *Ocean Modelling*, *40*(3-4), 246-259.

CHAPTER 5

Conclusion and Future Work

Presented in this dissertation is the creation, validation, and application of a new branch of stochastic slip rupture modeling. In combination with the rupture generation, I also use tsunami modeling as both a way to visualize the impact of subduction zone earthquakes and as a tool for studying the earthquakes themselves. In Chapter 2, I have detailed the new method for stochastic modeling where one can implement fault characteristics as a way to pre-condition models where slip may be more likely to occur during a rupture. Since the traditional method for stochastic modeling utilizes global rupture statistics, by incorporating a specific fault's interseismic coupling into the workflow, one can in theory produce slip distributions that are more characteristic of a specific fault. To test the impact of incorporating coupling in this way, I performed a probabilistic tsunami hazard assessment across the coastal Pacific Northwest for 4 different rupture classes based on varying assumptions or inclusion of a coupling constraint. From this study, it is apparent that incorporating coupling to inform slip produces observable differences than when the traditional method of generating stochastic slip models is used. Depending on the a priori assumption of near trench coupling, however, coastal tsunami hazards could be enhanced or reduced when compared to the hazard estimates from ruptures without coupling.

In Chapter 3, I validate both types of stochastic slip rupture modeling for their abilities to produce "realistic" **M**9+ slip distributions. Here, I quantified dissimilarity between stochastic slip distributions to previously published finite fault models for 4 recent and historic **M**9+ earthquakes as a proxy for testing their ability to produce great earthquakes. For the 2011 **M**9.1 Tohoku-Oki earthquake, we also compared tsunami inundations from our stochastic models with an inundation survey following the 2011 earthquake and tsunami. By comparing both dissimilarity of slip distributions and inundation extent, I determine that both the traditional K-L expansion approach and the coupling constrained modeling approach for generating stochastic slip models can produce past **M**9+ ruptures, and therefore have the potential for producing "realistic" great earthquakes.

With this validated approach for generating great earthquakes, I then constrained potential slip distributions for the 26 January 1700 Cascadia earthquake, as detailed in Chapter 4. I utilized a catalog of 37,500 stochastic rupture models. By comparing their resultant coastal deformation, tsunami arrival heights in Japan, and inundation area at 7 coastal sites to previously published paleoseismic datasets, I found 7 "wall-to-wall" ruptures that could satisfy all three constraints. These events share similar slip patterns, with a median peak slip and magnitude of 25 m and **M**9.11, respectively. Interestingly, when the median slip distribution of the potential events was compared to slip deficit rate models for the CSZ, we find good correlation between the slip deficit budget produced during the period between the 1700 event and the penultimate event (~800 years BP) and the median slip model, possibly illustrating that little slip residual was left after the last event. However, I also determined that sequences of 3 or 4 closely timed (years to a few decades) events could also satisfy the constraints. While both modes of failure could be considered good fits, I favor the hypothesis that Cascadia last ruptured in a full margin event due to the specific tidal conditions required for sequences to fit.

The value of the contents of this dissertation comes from their applicability for future studies. Because of the creation and validation of the coupling constrained stochastic modeling approach, there is now a way to create more fault specific rupture models. Related to Chapter 2, a future step could be applying this modeling technique and producing a more fully developed PTHA study that focuses on widespread hazards associated with inundation across the Pacific Northwest. With an imminent great CSZ rupture, updated tsunami hazards are needed for adequate preparedness. This PTHA study would follow the logic tree approach used by PSHA to better assess the potential hazards associated with a rupture and tsunami.

Similarly, a clear path for future steps is presented from Chapter 4: how can we further whittle down the possible slip distributions to just one, unique model for the 1700 event? A simple means for this would be to incorporate more coastal sites with tsunami deposits associated to the 1700 event. In Chapter 4, I only utilize 7 coastal sites; however, there are many other coastal marshes that have previously identified deposits. Rather than incorporating more sites, one could instead apply a more complex onshore inundation modeling which could benefit these results. For instance, one could instead incorporate sediment transport modeling into the workflow. Past studies that determined the locations of the paleotsunami deposits used in this dissertation have also recorded the thickness (and sometimes grain size and composition) of the

sand deposits. These could then be used in the sediment transport models which would hopefully better constrain the models. Additionally, splay faults associated with the megathrust have been observed throughout Cascadia, and possible activation of these shallow faults could have occurred during the 1700 CE event. Recent projects have been focused on mapping splay faults and their geometries across Cascadia. We could include these splay faults as possible contributors for slip and see how this impacts the fits to the geologic observations. Lastly, at some of these sites with paleotsunami deposits (e.g., Willapa Bay, WA), sand depositional pulses have been identified. These pulses could be associated with incoming wave pulses associated with the tsunami and could easily be included in the modeling approach. So, rather than only modeling whether a core is wetted or not, we could instead model and analyze how many times the location experienced an incoming wave pulse.